Heterogeneous Ice Nucleation from Laboratory–Generated and Field–Collected Aerosol Particles

A Dissertation Presented

by

Bingbing Wang

to

The Graduate School

in Partial Fulfillment of the Requirements

for the Degree of

Doctor of Philosophy

in

Marine and Atmospheric Science

Stony Brook University

December 2011

Stony Brook University

The Graduate School

Bingbing Wang

We, the dissertation committee for the above candidate for the Doctor of Philosophy degree, hereby recommend acceptance of this dissertation.

Daniel A. Knopf – Dissertation Advisor
Assistant Professor, Institute for Terrestrial and Planetary Atmospheres,
School of Marine and Atmospheric Sciences, Stony Brook University

Minghua Zhang – Chairperson of Defense
Professor, Institute for Terrestrial and Planetary Atmospheres, School of
Marine and Atmospheric Sciences, Stony Brook University

Robert L. de Zafra
Professor, Department of Physics and Astronomy, Stony Brook University

John E. Mak
Associate Professor, Institute for Terrestrial and Planetary Atmospheres,
School of Marine and Atmospheric Sciences, Stony Brook University

Alexander Laskin
Senior Research Scientist
William R. Wiley Environmental Molecular Sciences Laboratory, Pacific
Northwest National Laboratory

This dissertation is accepted by the Graduate School.

Lawrence Martin
Dean of the Graduate School

Abstract of the Dissertation

Heterogeneous Ice Nucleation from Laboratory–Generated and Field–Collected Aerosol Particles

by

Bingbing Wang

Doctor of Philosophy

in

Marine and Atmospheric Science

Stony Brook University

2011

Aerosol particles can serve as atmospheric ice nuclei (IN) and thus initiate ice formation resulting in the formation of cirrus and mixed-phase clouds and thereby indirectly affect the global radiative budget, hydrological cycle, and climate. Atmospheric ice crystal formation by heterogeneous nucleation is poorly understood and poses one of the largest uncertainties in predicting future climate. Here I present a laboratory study on heterogeneous ice nucleation efficiency and water uptake by various types of laboratory-generated and field-collected organic-containing particles for temperatures and relative humidity typical of the troposphere and lower stratosphere.

Laboratory–generated Suwannee river standard fulvic acid (SRFA) and Leonardite standard humic acid (Leonardite) particles served as surrogates of HUmic LIke Substances typically found in atmospheric particles. These organic particles nucleate ice efficiently via deposition mode (ice crystals form directly from the supersatu-

rated water vapor) and immersion freezing (ice crystals form from the ice nucleus suspended in supercooled aqueous droplets) at relevant atmospheric conditions. Oxidation of Leonardite and SRFA particles by O_3 led to a decrease in deposition nucleation efficiency and to water uptake at lower temperatures for the former and to an increase in the lowest temperature at which deposition nucleation was observed for the latter. Thus, particle hygroscopicity may not be the only factor determining particle's ice nucleation efficiency.

Laboratory–generated amorphous secondary organic aerosol (SOA) particles from anthropogenic precursor gases such as naphthalene serving as surrogates of ubiquitous SOA in the atmosphere demonstrated the potential to act as deposition IN at temperatures below 230 K and at relative humidity (RH) with respect to ice (RH_{ice}) below the homogeneous freezing limit. Water uptake was observed above 230 K followed by immersion freezing at temperatures between 230 and 242 K. The bulk atomic oxygen–to–carbon (O/C) ratio of these SOA particles did not show a significant effect on deposition ice nucleation but on water uptake. Above 230 K particles with higher O/C ratio take up water at lower RH than particles with low O/C ratio. These SOA particles may form a glassy, i.e. solid state, and nucleate ice via deposition mode below 230 K whereas they adopt a semi–solid state with lower viscosity at higher temperatures and take up water. Thus, phase state and viscosity affect the interaction of SOA with water vapor.

Different types of anthropogenic and marine impacted particles collected within and around the urban environments of Los Angeles and Mexico City were investigated for their potential to nucleate ice. To relate the particle's ice nucleation efficiency with chemical composition, micro–spectroscopic single particle analyses were applied by using computer controlled scanning electron microscopy with energy dispersive analysis of X–rays (CCSEM/EDX) and scanning transmission X–ray microscopy with near edge X–ray absorption fine structure spectroscopy (STXM/NEXAFS). The chemical composition was found to play a crucial role in determining the water uptake and immersion freezing but less for deposition nucleation. Overall, these field-collected particles can serve as efficient IN at atmospheric conditions typical for cirrus and mixed phase cloud formation and exhibit distinctly different ice nucleation efficiencies compared to the laboratory generated organic proxies.

The experimentally derived ice nucleation data were analyzed us-

ing classical nucleation theory (CNT) and the singular hypothesis approach (SH) providing heterogeneous ice nucleation rate coefficients (J_{het}) and cumulative IN spectrum (K), respectively, allowing either approach to be implemented in cloud resolving models. The experimentally derived J_{het} and corresponding contact angles were determined as a function of temperature and RH_{ice} and used to parameterize heterogeneous ice nucleation. Atmospheric implications of these findings and the proposed parameterizations are discussed.

Contents

List of Figures

List of Tables

Acknowledgements

The development of my doctoral thesis would not have been possible without the help and support of many colleagues and friends. I would like to thank all who participated directly and indirectly in the success of this thesis.

First and foremost, I would like to thank Daniel Knopf for offering me to join the Knopf group. It has been a pleasure working under your tutelage. Thank you for sharing your knowledge and skills with me and all the conversations and discussions that clarified my thinking. Thank you for your patience and promptly feedbacks during the writing for both scientific papers and the thesis. Thank you for being an outstanding advisor and mentor. Graduate school would not have been the same without your outstanding support.

I would like to thank all the collaborators for their support. I thank Alex Laskin for tremendous support and advice during the studies on the field samples and my visit at Pacific Northwest National Laboratory, Mary Gilles for the outstanding work on particle analysis and for inviting me to visit Lawrence Berkeley National Laboratory, Andrew Lambe and Paola Massoli for the support on SOA study, and other collaborators including Ryan Moffet, Tobias Roedel, Timothy Onasch, Paul Davidovits, and Douglas Worsnop.

I wish to thank the members of my Ph.D. committee including Minghua Zhang, John Mak, Robert de Zafra, Alex Laskin, and Daniel Knopf for their thoughtful advice and comments regarding my research. A special thank you to John, he introduced me Stony Brook University and served as my mentor for the my first semester at Stony Brook.

A special thank you goes to the members in Knopf and Mak's group including Peter Alpert, Yannick Rigg, Seanna Forrester, Jonathan Slade, Zhihui Wang, Tracey Evans, and Luping Su, especially, Peter and Zhihui for all the discussions and support. I also would like to thank all friends at Stony Brook, especially Tiantian Tang for her full support.

Finally, I could not have gotten this far without the love and encouragement from my family. They are always very supportive and for that I will always be thankful. To my sisters, thank you for taking care the family when I am far away from home for more than ten years .

Chapter 1

Introduction

1.1 The Atmosphere

Earth's atmosphere can be characterized by the variations of pressure and temperature with altitude. As altitude increases, the number of molecules decreases resulting in an exponential decrease of atmospheric pressure. The temperature profile with height can be used as a basis to distinguish the layers of the atmosphere. The atmosphere is divided into lower and upper regions. The lower atmosphere includes the troposphere and the stratosphere which extends to the stratopause (∼45–55 km). The troposphere is the lowest layer of the atmosphere where the temperature decreases with height from the Earth's surface up to the tropopause. The tropopause is at ∼8–18 km height depending on latitude and time of year[56,57]. Temperature increases with height in the stratosphere which extends from the tropopause to the stratopause. The temperature of the upper troposphere and lower stratosphere (UT/LS) can reach as low as ∼180 K, well below the ice melting point of 273.15 K.

In the atmosphere, the gas phase is composed primarily of nitrogen, oxygen, and argon. Trace gases, such as carbon dioxide and water vapor, only contribute less than 1% of the atmosphere by volume[57]. Water vapor is distributed throughout the atmosphere with highly variable concentrations. Air is transported resulting in redistribution of water vapor in the atmosphere. During transport, advection cools the air which can lead to the phase transition of water, e.g. condensation of water vapor, resulting in the formation of clouds. The formation of cloud particles, either aqueous droplets or ice crystals, always occurs on pre–existing aerosol particles associated with the air parcel[20]. Regions of the atmosphere with temperatures below 273 K have the potential to form ice crystals from pre–existing aerosol particles. This thesis focuses on the efficiencies of different types of organic and organic–containing aerosol particles to interact with water vapor, i.e. water uptake and ice nucleation at atmospheric conditions typical for the formation of cold clouds, such as cirrus and mixed-phase clouds.

1.2 Ice and Mixed–Phase Clouds and Aerosol–Cloud Interaction

1.2.1 Ice and Mixed–Phase Clouds

Different types of clouds cover about two thirds of the global surface. A cloud can contain aqueous droplets or ice crystals, or both. The classification of clouds can be based on their phases, i.e. liquid, ice, or mixed phase. Mixed-phase clouds contain both aqueous droplets and ice crystals. A cirrus cloud which contains only ice crystals is one type of ice cloud. Other ice containing clouds include high clouds which contain mainly ice crystals such as cirrostratus and cirrocumulus and mid-level clouds that contain both droplets and ice crystals such as altostratus and altocumulus[53,58]. Contrail cirrus which result from aircraft operations are purely anthropogenically induced clouds that affect radiative forcing on regional scales.

Mixed-phase clouds are frequent in mid–latitude and polar regions[58]. Previous studies have indicated that mixed-phase clouds dominated low cloud types within the Arctic region in winter[59–61]. Shupe et al.[61] showed that mixed–phase clouds occurred on average 41% of the time, with a maximum in fall (>70%) and ice clouds were observed 38% of the time, with a maximum of 52%. Cirrus clouds can account for one-third of the global cloud coverage and can form at any latitude with suitable environmental conditions[53,62,63]. Table 1.1 shows an example of the physical properties of mixed-phase clouds observed in the Arctic[54,64]. The typical measured variation of the physical properties of cirrus clouds is also listed[53,65]. Considering the high global cloud coverage of cirrus and mixed–phase clouds, it can expected that these clouds with inherently different properties will have different impacts on the global radiative budget[62,63].

1.2.2 Effects of Ice Crystal on Radiation and Precipitation

Clouds can modulate the short–wave and long–wave radiative fluxes through the atmosphere. Optical properties of ice crystals are determined by the refractive index of bulk ice, size, shape, and orientation. The shape and size of

Table 1.1: The average and the range of cirrus cloud properties adapted from Lynch et al.[53]. Annual mean and range of mixed-phase cloud properties observed in the Arctic in 1997–1998 adapted from Shupe et al.[54]. For mixed–phase clouds, the range represents monthly averages and covers the 5th to 95th percentiles of the data from Shupe et al.[54].

	cirrus cloud		mixed-phase cloud	
Property	Mean	Range	Mean	Range
Thickness / km	1.5	0.1–8	1.9	0.4–4.4
Altitude / km	9	4–20	0.9	0–3.5
Concentration / L^{-1}	30	10^{-4}–10^{4}	1–6[a]	0.1–10[a]
Ice content / g m^{-3}	0.025	10^{-4}–1.2	0.027	10^{-4}–0.11
Size / μm	250	1–8000	93	27–200

[a] Measurements from the Mixed-Phase Arctic Cloud Experiment (M-PACE) in 2004[64].

ice crystals render the radiative forcing by ice–containing clouds significantly more complicated than that of warm clouds which contain spherical aqueous droplets[66]. The shapes of ice crystals are also responsible for some atmospheric optical phenomena such as halos and sundogs.

Figure 1.1 shows highly simplified sketch for the radiative effects of different types of clouds. All clouds can reflect short–wave radiation, and have a cooling effect on the Earth–atmosphere system. For ice and mixed-phase clouds, the absorption of long-wave radiation and re–emission at colder temperatures can dominate the scattering of solar radiation if the clouds have sufficiently low optical depth. As optical depth becomes larger, the solar albedo effect increases, leading to a net cooling[53]. The radiative response of cold clouds is further influenced by their coverage, altitude, thickness, spatial inhomogeneity, and numerous other factors, including ice crystal number, size, shape, solar zenith angle, and surface albedo[53,66].

Mixed-phase clouds have been identified to have an important climatic effect, especially in the polar regions[67–70]. In the Arctic, for example, the dominant radiative effect of mixed–phase clouds during wintertime is due to long–wave radiative fluxes because of the virtual absence of sunlight. The optical depth for mixed–phase clouds was determined to range from 0.03 to 21 with annual average of 3[67].

Cirrus clouds can have varying effects on the radiation budget. Thin cirrus clouds can have a predominant warming effect by effectively trapping the outgoing long–wave radiation[63,71]. Optically thick ice clouds still warm the atmosphere on the whole but cool the surface and the upper atmosphere[63].

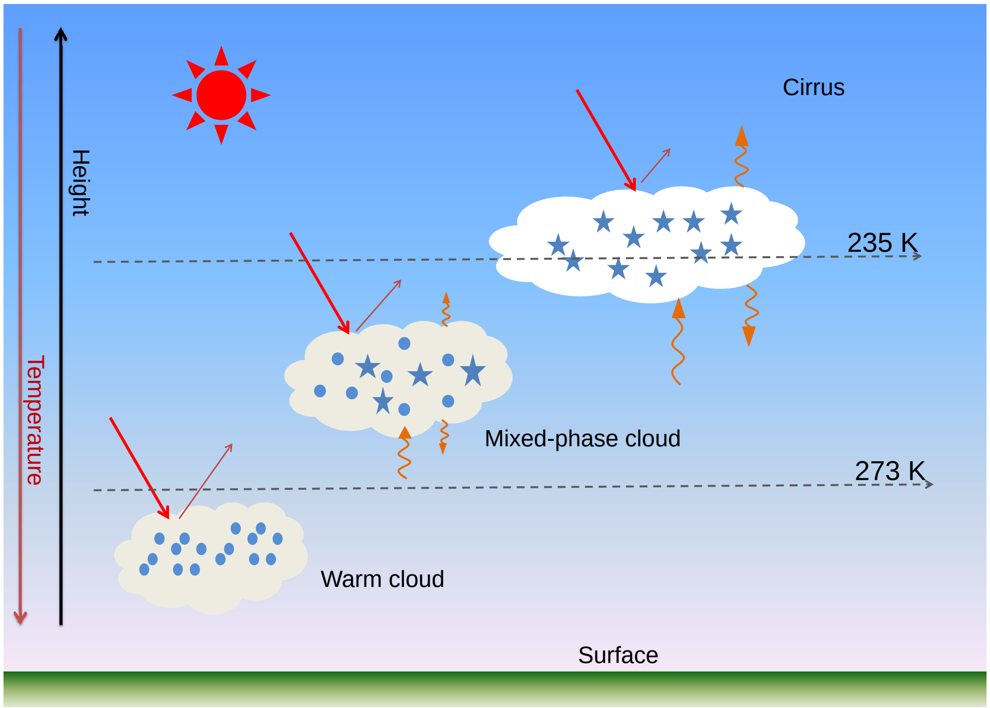

Figure 1.1: Simplified radiative effects of different types of clouds. Clouds containing ice particles (stars) and/or aqueous droplets (dots) regulate the long-wave (wavy arrows) and short-wave (arrows) radiative fluxes.

The optical depth for cirrus ranges from less than 0.03 for subvisual cirrus up to 50 for anvil cirrus[53].

To illustrate the effects of surface albedo, cloud and surface temperature, and optical depth on radiative fluxes at the top of the atmosphere, different types of clouds with various properties are calculated here, for illustrative purposes, using a simple model proposed by Corti and Peter[55]. Table 1.2 demonstrates the net cloud radiative forcing at the top of atmosphere for different types of clouds using various observed properties. These idealized estimates clearly show the effect of different cloud properties on the net cloud forcing.

The radiative properties of ice and mixed–phase clouds are determined in part by the underlying ice nucleation mechanisms which can produce ice crystals with different number concentrations, sizes, and shapes[72–74]. Inhomogeneities in the cloud structure affect radiative properties as well, rendering radiative transfer calculations as very challenging[66].

By transporting water vapor from Earth's surface and redistributing it in the atmosphere and back to the surface, clouds can affect and regulate the

Table 1.2: The net cloud radiative forcing at the top of atmosphere for different types of clouds for given properties including cloud top and surface temperature, surface albedo, and optical depth assuming the global and daily mean conditions approximated by a zenith angle of 60 degree in combination with a solar constant of 684 W m^{-2} suggested by Corti and Peter[55].

	Cirrus			Mixed-phase clouds	Warm clouds
Surface albedo	0.3	0.7	0.7	0.9	0.7
T(surface)/K	290	260	260	260	290
T(cloud top)/K	220	220	220	250	280
Optical depth	0.1	1	3	3	80
Net forcing (W m^{-2})	7	32	16	5	42
	warming	warming	warming	warming	cooling

atmospheric hydrological cycle. In mixed-phase clouds, heterogeneous ice nucleation is the only pathway for ice initiation and thus is crucial for the precipitation development[75]. This in turn defines the degree of cloud glaciation with subsequent consequences for precipitation and the hydrological cycle[64,66,70,76].

In mixed-phase clouds, the air is saturated with respect to supercooled liquid water and is supersaturated with respect to ice. The imbalance between the vapor pressure over ice and over supercooled water leads to rapid growth of the ice crystals at the expense of aqueous droplets, known as the Wegener–Begeron–Findeisen process[77–79]. Therefore precipitation formation is more efficient in mixed-phase clouds than in warm clouds[80,81]. The magnitude of this glaciation effect depends strongly on assumptions of the ice nucleation efficiency of the ice nuclei[81,82]. The important microphysical properties of clouds include ice crystal number concentration, size, and shape which again are significantly affected by the ice nucleation mechanisms and also the efficiency of IN[80]. But the effect of IN on precipitation still remains a challenging problem because of many uncertainties with respect to their concentration under different environment conditions[83].

Ice formation in the UT/LS region resulting in cirrus cloud formation, can lead to dehydration of the UT/LS region by triggering gratvational sedimentation of ice particles[84]. This dehydration process affects the water vapor distribution and thus changes the hydrological cycle and the global radiation budget[85,86]. In the UT/LS region, this process also controls the amount of water vapor transported into the stratosphere, resulting in important consequences for stratospheric chemistry[87,88].

1.2.3 Formation of Ice and Mixed–Phase Clouds

Clouds are initiated by aerosol particles through cloud microphysical processes which involve ice, liquid water, and water vapor. Aerosol–cloud interactions pose one of the largest uncertainties in prediction of future climate changes due to the insufficient understanding of cloud microphysical processes[89]. Whereas an increasingly better understanding of the role of CCN on warm cloud formation is being achieved, the effect of aerosol particles serving as IN on the atmosphere is still not well understood[66,89–96]. This is mostly due to the insufficient understanding of the ice nucleation mechanisms and the ice nucleation efficiencies of aerosol particles[66,89–91].

By serving as IN, aerosol particles can initiate ice nucleation and may induce the formation of ice and mixed–phase clouds. The interactions between aerosol and clouds will change the cloud microphysical processes, lead to the formation of new clouds and modification of the existing clouds, and subsequently affect the distribution and lifetime of clouds and thus climate[66,89,90,97–100]. The strength of these aerosol indirect effects depends on the propensity of the particles to act as IN and corresponding ice nucleation mechanisms.

In the atmosphere, ice formation can proceed via homogeneous or heterogeneous nucleation from aerosol particles[20,101]. Homogeneous ice nucleation proceeds from supercooled aqueous particles below ∼235 K[20,33,101,102]. Heterogeneous ice nucleation is initiated by a pre–existing substrate, the ice nucleus[20,101]. Heterogeneous ice nucleation occurs at warmer temperatures and lower supersaturations with respect to ice than homogeneous ice nucleation[20,102] and hence renders IN an important role in atmospheric ice formation. The different nucleation mechanisms produce ice crystals with different sizes, shapes, and number concentrations depending on the atmospheric conditions and the available IN[72–74].

Ice formation via heterogeneous ice nucleation can be further subdivided into the following pathways: (a) deposition mode in which IN form ice crystals directly from supersaturated water vapor, (b) immersion freezing in which ice crystals form from immersed IN in supercooled aqueous droplets, (c) condensation freezing in which ice crystals form during the condensation of water vapor onto IN at supersaturated conditions, and (d) contact freezing in which ice formation is trigged by collision of supercooled droplets with IN[20,101]. In cirrus levels, the dominant nucleation modes include homogeneous ice nucleation, immersion freezing, and deposition nucleation whereas for mixed–phase clouds, immersion freezing, contact freezing, and secondary ice multiplication may be dominant[72].

The mechanism and effectiveness of contact freezing remains unknown, although previous studies have shown that certain particles may nucleate ice at

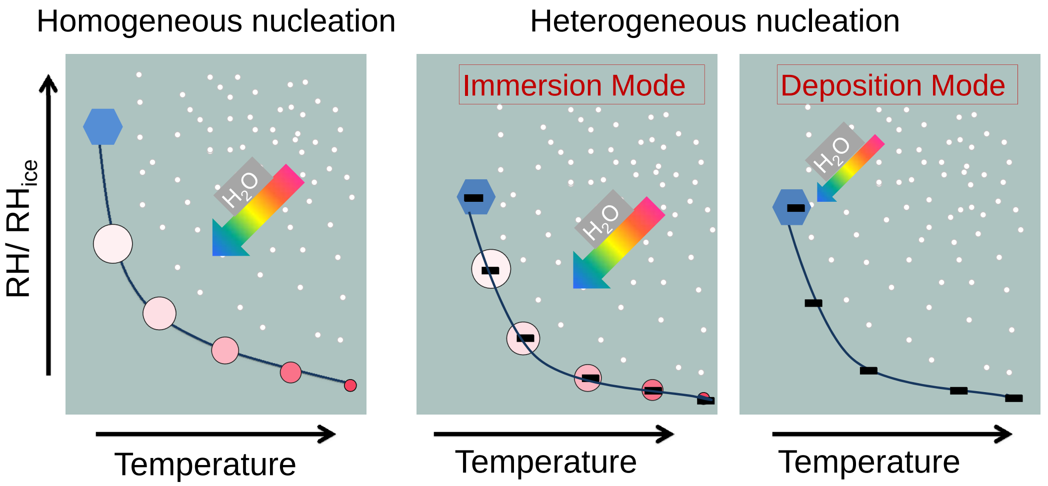

Figure 1.2: Homogeneous ice nucleation and heterogeneous ice nucleation.

higher temperatures via contact freezing compared to immersion freezing[20]. Furthermore, the relative role of contact freezing in atmospheric ice formation is also not clear[91]. Secondary ice multiplication (i.e. rime splintering, fragmentation during evaporation, or collisions between crystals) is also believed to be important for the glaciation processes of supercooled water clouds. Both contact freezing and secondary ice multiplication are much less understood[91]. Condensation and immersion freezing cannot be completely separated since IN are both suspended in aqueous droplets and also the formation of an immersed particle in a droplet is often due to water uptake. Thus, immersion and condensation freezing may be regarded as similar. This study only focuses on immersion freezing and deposition ice nucleation.

Figure 1.2 shows how ice crystals form via homogeneous and heterogeneous ice nucleation. As temperature decreases and relative humidity increases, particles may take up water vapor and/or nucleate ice. Particles which dissolve and subsequently take up water continuingly nucleate ice homogeneously. AN insoluble particle immersed in an aqueous droplet can nucleate ice via immersion freezing. Ice nucleation via condensation freezing undergoes a similar process compared to immersion freezing. For deposition ice nucleation, ice nucleates on particles directly from the supersaturated water vapor without formation of *macroscopic* water layers.

The complexity and multipathways of ice nucleation render the determination of the ice nucleation efficiencies of particles very challenging, in particular when consider the physical and chemical complexity of atmospheric aerosol particles.

To describe the ice nucleation processes, different theories or hypotheses have been developed. The main descriptions include: (a) classical nucleation theory (CNT)[20,57,103–106], (b) singular hypothesis (SH)[107–110], (c) activated IN fraction[9,111–113], (d) water-activity-based approach[33,52,114–119,119], and (e) an approach using a combination of CNT and SH[120–122].

CNT states that homogeneous and heterogeneous nucleation are due to stochastic processes and provides a physical model of ice nucleation applying independent thermodynamic variables, such as temperature and RH[20]. SH assumes that heterogeneous ice nucleation occurs on active sites located on the particle surface which become active at characteristic temperatures[107]. This time–independent approach provides an overall phenomenological explanation for heterogeneous ice nucleation. The approach arising from a combination of CNT and SH can be essentially considered as a "modified singular hypothesis"[122]. The IN activated fraction, i.e. the number of particles activating ice formation of total particle number, is a measure commonly used to describe ice nucleating efficiency of particles, neglecting the information of particle surface area[112]. The water–activity–based approach has been used to describe homogeneous ice nucleation and immersion freezing and to predict freezing temperatures and nucleation rate coefficients if the water activities of aqueous droplets are known[33,52].

So far none of those approaches can provide perfect agreement between theory and laboratory and field measurements[20]. Also disagreements among these descriptions persist. One of the main longstanding debates is whether heterogeneous ice nucleation should be described by a stochastic or deterministic process. And so the lack of physical theory for nucleation renders parameterizations of experimental results for weather and climate models more difficult and challenging.

1.3 Aerosol Particles in the Atmosphere

1.3.1 Aerosol Particles

An aerosol is defined as a relatively stable suspension of solid or liquid particles in a gas[56,57,123]. Aerosol particles are ubiquitous in the atmosphere and their number concentrations can reach up to 10^8 cm^{-3} with sizes ranging from ∼20 to ∼100 μm in diameter[56]. Particles smaller than 2.5 μm are identified as fine particles and those with diameters larger than 2.5 μm are defined as coarse particles. Aerosol particles may be either directly emitted into the atmosphere or formed in site in the atmosphere which are referred as primary and secondary particles, respectively.

Primary particles in the atmosphere stem from natural and anthropogenic sources. Natural sources include sea spray, deserts, volcanos, forest fires, and vegetation, among others. Major anthropogenic sources are fossil fuel combustion, biomass burning, and industrial processes[124–129]. Secondary particles are formed from natural or anthropogenic precursor gases by nucleation, condensation, and chemical reactions[56,57]. The chemical and physical properties of particles can vary significantly depending on a number of factors, such as their sources, size, location, and formation mechanisms[56,57].

Particles of various complexities and chemical and physical properties emitted or generated from different sources play important roles in air quality, health–related issues, cloud formation, and climate[56,57]. Particles can affect the global radiative budget directly by scattering and absorption of solar and terrestrial radiation and indirectly by serving as cloud condensation nuclei (CCN) and ice nuclei (IN)[66,89,90,97–100]. The efficiency of particles to act as CCN and IN are determined by particle sizes, chemical composition, number concentration, morphology, and phase state. Thus, knowledge about the CCN and IN efficiencies of aerosol particles along with their chemical and physical properties improves the understanding of the aerosol indirect effects and thus their impacts on climate.

1.3.2 Chemical Composition of Particles

Atmospheric aerosol particles can be composed of an extremely diverse mixture of chemical species which strongly depends on particle sources, formation mechanisms, and atmospheric processing. The chemical components of aerosol particles can be divided into inorganic and organic compounds which are either internally or externally mixed. Abundant inorganic components include water soluble substances such as ammonium sulfate, sulfuric acid, ammonium nitrate, and sodium chloride and water insoluble substances such as mineral dust[56,57].

Organic materials in aerosol particles contain a myriad of different chemical compounds, many of which have not been chemically identified yet[130]. The organic fraction of atmospheric particles can consist of water soluble organic material typically represented by mono–, di– and poly–carboxylic acids, polyols, aromatic acids, sugars, and other functional groups[92,131–135]. In addition, water insoluble organics such as soot or black carbon are also present as common constituent in aerosol particles[136]. Soot particles are emitted from combustion processes such as transportation, biomass burning, domestic heating, and cooking. One type of organic material with high molecular weight extracted from atmospheric particles, termed HUmic LIke Substances (HULIS), include both water soluble compounds such as fulvic acid and water insoluble sub-

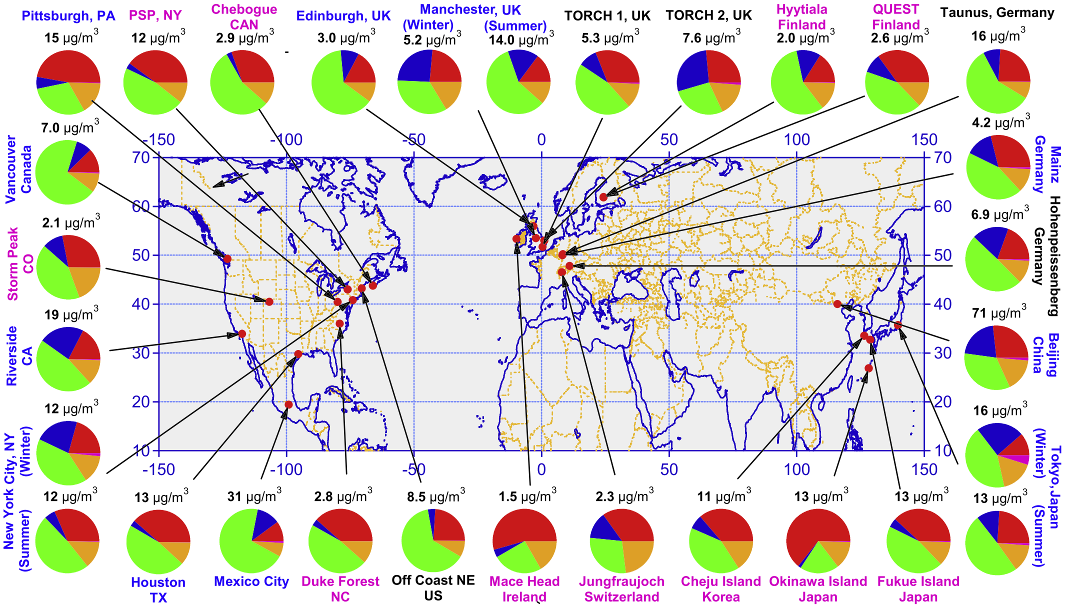

Figure 1.3: The average mass concentration and chemical composition of fine particulate matter measured at various locations in the Northern Hemisphere using aerosol mass spectrometer adapted from Zhang et al.[1]. Color coded labels of sample location: urban areas (blue), location at less than 100 miles downwind of major cites (black), and rural/remote areas at more than 100 miles downwind (pink). Pie charts show the average mass concentration and chemical composition: organics (green), sulfate (red), nitrate (blue), ammonium (orange), and chloride (purple) of non-refractory submicron particle.

stances such as humic acid[135]. HULIS have various sources including primary terrestrial sources, biomass burning, secondary organic aerosol formation, and marine sources[135,137–146].

Organic materials in general contribute ∼20–50% to the total fine particle mass at continental mid-latitudes and up to 90% in tropical forested areas[1,92,123,130,147,148]. The major sources of organic particles include fossil fuel combustion, biomass burning emission, and secondary organic formation[130]. Biomass burning is a major source of atmospheric particles with the source strength similar to fossil fuel burning[149,150]. Biomass burning aerosol particles consist of a complex mixture of organics and inorganics and can reach to the UT/LS region[151–153]. Another type of organic particles, known as secondary organic aerosol (SOA), are formed by oxidation of both anthropogenic and biogenic semi–volatile and volatile organic compounds (VOCs). SOA can also contribute to a significant fraction of total organic particles[1,92,130].

Figure 1.3 shows an overview of chemical composition of particles with size smaller than 1 μm measured by aerosol mass spectrometry at various locations in the Northern Hemisphere[1]. Organic compounds found in the condensed phase comprise a major fraction of the submicron particle mass ranging from 18–70% with an average of 45%, while sulfate accounts for 32% on average and other compounds account for the rest[1]. Zhang et al.[1] showed that oxygenated organic aerosol components on average account for 64%, 83%, and 95% of the total organic mass in urban, urban downwind, and rural/remote sampling sites, respectively. Zhang et al.[1] also frequently identified highly oxygenated organic components that exhibit a mass spectrum similar to fulvic acid which is a suggested model compound for highly oxidized organics present in the atmospheric particles[1,154].

Organic compounds in the particle phase were also often found in the UT/LS region where temperatures favor ice formation[2,155,156]. For example, Murphy et al.[2] measured the chemical composition of individual particles using a laser ionization mass spectrometer at altitudes between 5 and 19 km in the Northern Hemisphere. As shown in Fig. 1.4, in situ measurements of the chemical composition of individual particles reveal the existence of an extremely diverse set of particles in the troposphere and the stratosphere. The particles usually consist of both organics and sulfates (internally mixed) with different ratios depending on the altitudes[2]. Murphy et al.[2] showed that in the stratosphere sulfates are dominated by a small fraction of organics while in upper troposphere aerosol particles often contained much more organic material than sulfate. Previous studies have shown that IN residues indeed contain organic materials[112,156–158]. This indicates that these organic particles could affect the initiation of ice crystal formation but the exact effects are not yet clear.

1.3.3 Atmospheric Aging of Particles

During their atmospheric lifetime, particles provide surfaces on which low volatility compounds can condense and reactive trace gas species can react. The related processes, known as atmospheric aging, can change the particle's chemical and physical properties which subsequently can affect the efficiency of the particle to serve as CCN and IN[92,159–162]. Particles can undergo different physical and chemical aging processes in the atmosphere including, but not limited to: 1) condensation of SOA on pre-existing particles[57,92], 2) condensation of hydrophilic material such as inorganic acids, e.g., H_2SO_4 and HNO_3[140,163,164], and 3) heterogeneous oxidation by atmospheric trace gases such as O_3, NO_3, and OH[92,161,162,164–168].

Previous studies have investigated the effects of aging processes on ice nu-

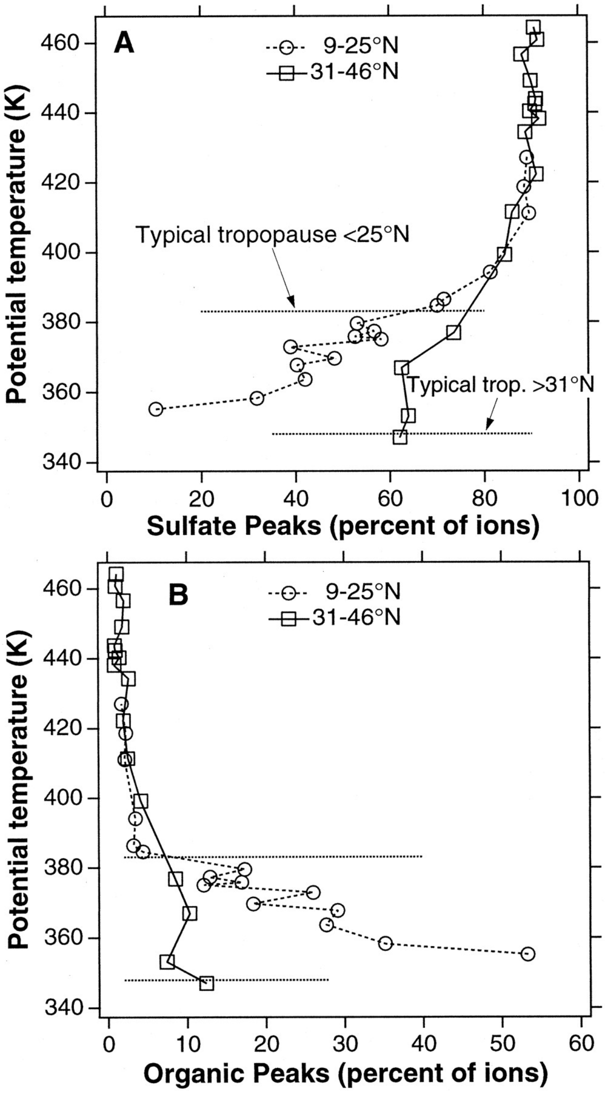

Figure 1.4: Average profiles of the percentage of ion current in sulfate (A) and organic (B) peaks measured using a laser ionization mass spectrometry operate in the troposphere and the stratosphere in the Northern Hemisphere as a function of potential temperature adapted from Murphy et al.[2]. Each mass spectrum from an single particle was normalized to a total ion current of 100%. Several sulfur-containing peaks were summed to establish the sulfate signal.

cleation using laboratory-generated particles[3,9,11,13,169–174]. The condensation of SOA on available pre–existing particles during transport may change their chemical and physical properties[11,57,92]. For example, Möhler et al.[11] found that the ice nucleation efficiency of mineral dust such as illite was significantly suppressed by a coating of SOA stemming from the reaction of α–pinene with O_3. Particles become more hydrophilic due to the condensation of inorganic acids thus affect the propensity to interact with water vapor[13,170,172,173]. This process can facilitate the water uptake, but also destroy ice nucleation active sites due to chemical reaction by the strong acids. For example, the coating of H_2SO_4 can significantly decrease the ice nucleation efficiencies of mineral dust[170,173] and soot[9].

Another atmospheric aging process is due to the heterogeneous oxidations, i.e. gas–to–particle reactions, involving gas phase oxidants and radicals. In general, heterogenous oxidation can lead to the addition of oxygenated functional groups to the condensed phase organic fraction resulting in the increase of oxidation state and hygroscopicity or lead to the volatilization of organic compounds[92,162,164,165]. These reactions will alter the chemical and physical properties of the particle's surface and thus are expected to change the ice nucleation efficiency of the particle. Only a few studies so far have investigated the effect of organic particle oxidation on ice nucleation and those are limited to temperatures above 240 K[3,174]. Both studies showed that oxidation of soot by gas phase O_3 does not significantly change corresponding ice nucleation efficiencies compared to unoxidized soot particles[3,174]. In other ice nucleation studies particles were chemically aged by exposure to liquid oxidative agents such as hydrogen peroxide[169] and nitric and sulfuric acid mixtures[13]. Clearly, the effects of different atmospheric aging processes on ice nucleation from organic particles are insufficiently investigated.

1.3.4 Physical State of Particles

The physical state (phase) and morphology of aerosol particles play a crucial role in determining their interaction with water vapor and thus affect the abilities of the particles to serve as IN. Particles may adopt different phase states including crystalline, liquid, and amorphous semi-solid and solid (i.e. glassy)[19,175]. Depending on viscosity the amorphous state can be further classified as glasses, rubbers, gels or viscous liquids[176]. A glass is an amorphous solid which exhibits mechanical properties as a solid, but lacks the long-range molecular order which is typical of the crystalline state[177]. The physical state of atmospheric particles depends on the their chemical composition and surrounding atmospheric conditions, such as temperature and RH[19,175,176,178].

Ice formation processes are very selective and one of the main requirements for IN is the insolubility requirement[20], at least IN should be insoluble or imcompletely dissolved to provide solid surfaces. Thus, the ice nucleation efficiency of particles can show a strong sensitivity on initial particle phase states which also depend on composition, mixing state, and the surrounding conditions[6,19,46,50,175,176,178–180]. Aqueous droplets or highly hygroscopic soluble particles (e.g., H_2SO_4) without insoluble components may only freeze via homogeneous ice nucleation whereas insoluble particles, such as mineral dust, can nucleate ice via immersion freezing and deposition ice nucleation. The importance of the phase state is also highlighted by recent observations that the water soluble compounds ammonium sulfate and oxalic acid can nucleate ice via deposition mode when being in a crystalline state[6,50]. Different phases of organic particles may result in different interactions with water vapor which in turn can influence particles to act as IN[176]. A recent study by Murray et al.[46] have shown that glassy citric acid particles at temperatures below 212 K can nucleate ice via the deposition mode. But at temperatures above 212 K, these citric acid particles adopt a liquid state and nucleate ice homogeneously[46]. This indicates that the existence of different phase states at different temperatures and RH can influence the ice nucleation pathways of the particles.

As discussed above, not only the various ice nucleation pathways and the complex nature of the particles but also atmospheric aging processes and particle phase states controlled by ambient temperature and RH, further complicate the understanding of the effects of aerosol particles on cloud formation.

1.4 Ice Nucleation of Organics Particles

The efficiency of homogeneous ice nucleation from aqueous particles is well constrained when the water activity of the aqueous solution is known whereas the ice nucleation efficiencies of atmospheric aerosol particles via heterogenous nucleation remain poorly understood[20,33,66,89–91,115,116]. In the atmosphere, typical number concentration of IN ranges from ∼0.001 to 0.01 $\mathrm{cm^{-3}}$, although values up to 1 $\mathrm{cm^{-3}}$ have been observed[181]. The very low IN number concentrations, compared with that of the total ambient aerosol, which can be as low as 10 $\mathrm{cm^{-3}}$ in clean conditions, but are still four orders of magnitude higher than the IN concentrations, presents unique measurement and modeling challenges.

Previous cirrus and mixed–phase cloud studies have shown that ice crystal residues can contain organic material[112,156,158,182–184], but the exact effect of organics on ice nucleation is not clear. These field studies suggested that organic material may act as IN[112,156,183] but also demonstrated that the organic material can inhibit ice nucleation[112,184,185]. For example, DeMott et al.[112] investigated the capability of particles to initiate cirrus clouds and showed that both natural and anthropogenic particles contribute to the IN population.

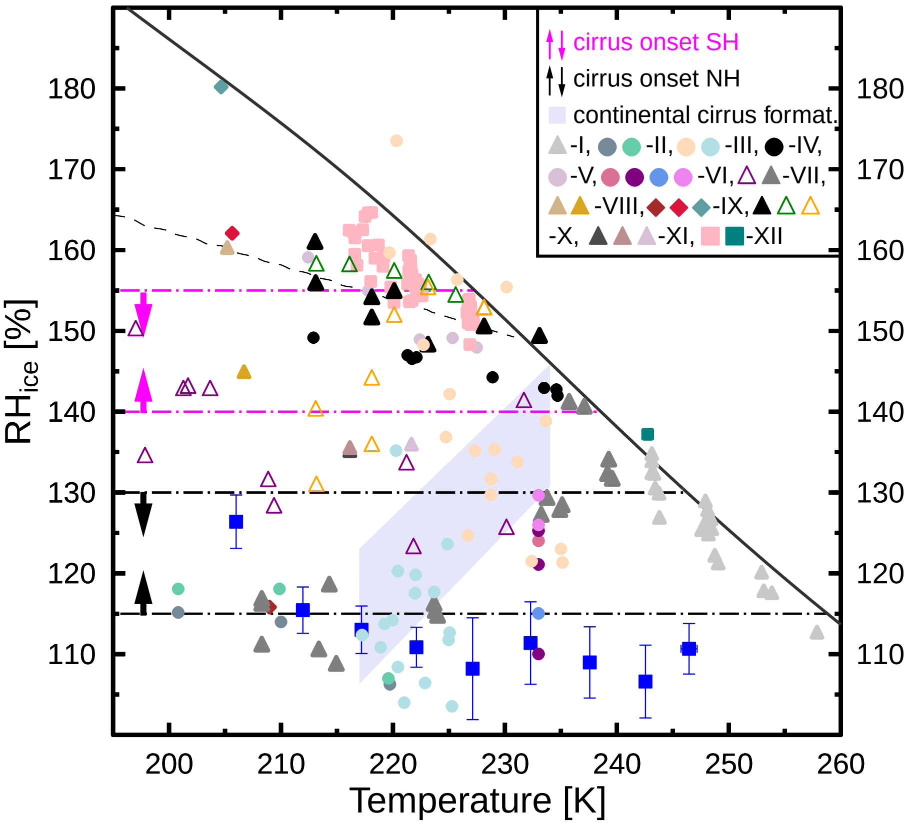

Figure 1.5: Blue squares represent ice nucleation onsets on kaolinite particles. Reported heterogeneous ice nucleation onsets for laboratory generated proxies of organic particles: I–soot aged by O_3 from Dymarska et al.[3]; II–maleic acid and mixed maleic acid-ammonium sulfate particles from Shilling et al.[4]; III–glutaric acid and mixed glutaric acid-ammonium sulfate particles from Baustian et al.[5]; IV–crystalline oxalic acid in aqueous solution from Zobrist et al.[6]; V–adipic acid from Prenni et al.[7]; VI–leonardite, oxalic acid, sodium humic acid, and octyl-silica from Kanji et al.[8]; VII–soot coated with sulfuric acid, and uncoated soot particles from Möhler et al.[9]; VIII–soot containing different amounts of sulfur from Möhler et al.[10]; IX–Arizona test dust coated by secondary organic aerosol (SOA), illite coated by SOA, pure SOA from Möhler et al.[11]; X–soot, soot coated with a monolayer, and multiple layers of sulfuric acid from DeMott et al.[12]; XI–three different types of oxidized soot surrogates from Koehler et al.[13]; XII–biomass burning particles from two different studies from DeMott et al.[14], Petters et al.[15]. Light grey shaded area indicates bounds of continental cirrus formation from Heymsfield and Miloshevich[16]. The RH_{ice} ranges between horizontal paired lines with corresponding arrows indicate the lower limits for cirrus formation conditions in northern (black dash-dotted lines) and southern hemisphere (pink dash-dotted lines) from Ström et al.[17] and Haag et al.[18].

Although these few in situ observations provided information of potential particles to serve as IN, the measurements were limited to a narrow range of temperature and RH or were conducted at fix particle temperatures[112,158,185]. There is still a shortage of information about the concentrations, sources, and properties of IN in the atmosphere.

Early laboratory studies have already indicated that organic particles can act as efficient IN but the measurements were limited to the determination of temperature thresholds without information of corresponding RH[169,186–191]. More recent laboratory studies investigated the heterogeneous ice nucleation efficiencies of different organic and organics-containing particles serving as proxies of atmospheric aerosol particles[4–9,12,14,15,46,49,117,119,158,171,174,192–201].

Figure 1.5 shows heterogeneous ice nucleation data from previous studies using laboratory generated organic or organic-containing particles as proxies of atmospheric aerosol particles[3,4,6,8,11,14,15,158,171,196,199,200]. Previous studies have shown that various type organics can serve as efficient IN, such as insoluble soil substances[199,202], organic monolayer coatings on aqueous particles[6,118,192], certain dicarboxylic acid particles in the crystalline state[4–6,48], and soot particles[9,12,200,203,204]. Zobrist et al.[6] showed that oxalic acid dihydrate can act as heterogeneous IN in immersion freezing. Maleic acid, mixed maleic acid ammonium sulfate, and mixed glutaric acid ammonium sulfate particles when in the crystalline state can nucleate ice via deposition nucleation at similar RH_{ice} and temperatures compared to the clay mineral, kaolinite, which is known to be an efficient IN[4–6,48]. Only a few studies have investigated the ice nucleation ability of HULIS which can be a major component of organic aerosol particles[8,199]. Kanji et al.[8] showed that sodium humic acid and Leonardite (humic acid) can nucleate ice via the deposition mode. However this study was limited to 233 K.

However other laboratory studies also observed that certain organic particles are not efficient IN. For example, some dicarboxylic acids particles such as adipic acid[7,195] and complex organic particles from biomass burning[14,15]. The majority of the laboratory studies indicate that carbonaceous particles (soot and organic particles) are inefficient IN under conditions relevant for cirrus formation which is shown as the gray area and regions indicated by paired dash-dotted lines[16–18]. Only a small part of reported ice nucleation data coincides with onset conditions relevant for cirrus formation[16–18].

Although atmospheric aging of organic particles can affect particle composition which in turn may change their ice nucleation ability, so far only two studies have investigated the effect of chemical aging on ice nucleation activity[3,174]. Dymarska et al.[3] indicated that oxidation of soot by O_3 did not have a significant effect on the heterogeneous IN ability of soot particles at temperatures above 240 K. Friedman et al.[174] showed that oxidation of soot and oleic acid coated soot particle by O_3 also did not significantly change the ice nucleation of the corresponding uncoated particles at temperature between 233 K and 258 K. Clearly, there is an urgent need for more laboratory studies on the effect of chemical aging on ice nucleation ability of different organic particles.

Since SOA contribute to a significant fraction of the global organic particle budget, it is extremely important to understand their ice nucleation efficiency. But prior to this work only two studies have investigated the ice nucleation efficiency of SOA and both showed that pure SOA are not efficient IN[11,171]. Möhler et al.[11] showed that the coating of SOA stemming from the reaction of α–pinene with O_3 suppressed the ice nucleation of mineral dust. Furthermore, only one study has investigated the ice nucleation efficiency of an amorphous solid organic particle under conditions of the upper troposphere[46]. Murray et al.[46] showed that glassy citric acid particles at temperatures below 212 K can nucleated ice via deposition mode. But at temperatures above 212 K, the citric acid particles adopted a liquid state and nucleated ice homogeneously[46]. More studies are needed to investigate the IN potential of amorphous organic particles since recent studies have indicated that biogenic SOA can be semi–solid and glassy at high temperatures[205,206].

The above discussion shows that ice nucleation investigations are needed using laboratory generated organic and organic-containing particles serving as amorphous organic particle surrogates. Although laboratory generated proxies may not perfectly represent atmospheric aerosol particles, these studies can significantly contribute to a better description of the underlying physical processes leading to the formation of ice. In addition, atmospheric organic particles should also be investigated at conditions typical for cirrus and mixed-phase cloud formation to infer ice crystal formation from complex, natural occurring aerosol particles. This combined approach allows to relate ice nucleation efficiencies of controlled laboratory–generated IN with atmospheric IN.

1.5 Thesis Objectives

Aerosol particles affect the climate indirectly through aerosol-cloud interactions. The exact effects of aerosol particles serving as IN on the atmosphere are still not well understood, due to the insufficient understanding of the underlying ice nucleation mechanisms and the complex nature of atmospheric particles. This Ph.D. thesis focuses on heterogeneous ice nucleation and water uptake by various types of organic and organic-containing aerosol particles and addresses the three main questions outlined below.

First, can organic particles from biomass burning serve as IN? How efficient and to what extent does oxidation by O_3 change the ice nucleation ability of these particles? Second, can organic particles from secondary organic formation serve as IN? How do the phase and oxidation state of these particles affect their ice nucleation efficiency and water uptake? Third, how do real atmospheric aerosol particles from different urban environments behave in terms of ice nucleation? To address these three questions, this thesis focuses on the following objectives: 1. Determination of heterogeneous ice nucleation and water uptake by laboratory–generated Suwannee river standard fulvic acid (SRFA) and Leonardite standard humic acid (Leonardite) particles serving as surrogates of HULIS in atmospheric particles and the effect of particle oxidation by O_3 on corresponding IN efficiencies. 2. Determination of heterogeneous ice nucleation and water uptake by amorphous SOA particles with different O/C ratios generated from naphthalene serving as anthropogenic precursor gas. 3. Determination of heterogeneous ice nucleation and water uptake by particles impacted by anthropogenic and marine sources collected within and around the urban environments of Los Angeles and Mexico City. The results from these three objectives are presented in Chapter 4, 5, and 6, respectively. The major findings are summarized and an outlook is given in Chapter 7.

Chapter 2

Theory of Ice Nucleation and Phase State of Particle

2.1 Water Vapor Pressure

An aerosol particle interacts with surrounding water vapor. When the water or ice vapor pressure of the particle is lower than ambient water vapor partial pressure, water uptake or ice deposition can occur. If it is greater, water evaporation or ice sublimation can proceed. The measurements of water vapor pressures over supercooled water are difficult in part due to homogeneous freezing of supercooled water at temperatures below 235 K. But also larger water samples will freeze at significantly higher temperatures rendering these experiments very challenging. Therefore, for temperatures as low as 180 K, the description of water vapor pressures over supercooled water and ice depends on indirect measurements of molar heat capacity and the use of a physical model. The most recent updated parameterizations for the saturated water vapor pressure over a plane water and ice surfaces are provided by Murphy and Koop[25] as described below.

The saturated water vapor pressure over a plane supercooled water surface (p^0_{w}) for 123 K < T < 332 K is calculated using the following equation with temperature (T) in K and pressure in Pa,

$$\begin{aligned} ln(p_{\mathrm{w}}) \approx\ & 54.842763 - 6763.22/T - 4210ln(T) + 0.000367T \\ & + tanh(0.0415(T - 218.8))(53.878 - 1331.22/T \\ & - 9.44523ln(T) + 0.04025T). \end{aligned} \tag{2.1}$$

The saturated water vapor pressure over a plane surface of ice (p^0_{ice}) is calculated using the following equation for T > 110 K,

$$ln(p_{\mathrm{ice}}) = 9.550426 - 5723.265/T + 3.53068ln(T) - 0.00728332T. \tag{2.2}$$

Small ice crystals and water droplets less than few micrometers have higher vapor pressures than bulk phases due to the Kelvin effect. At 200 K, the differences are $\sim$ 0.5% to 5% for particles with 1 to 0.1 μm, respectively. At higher temperatures, the differences are smaller[25]. For the investigated temperature range in this study, these differences are smaller than the experimental uncertainties.

The formation of a liquid droplet or an ice crystal in the atmosphere depends on saturation or relative humidity and temperature. The saturation ratio with respect to water (S) and to ice (S_{ice}) and relative humidity with respect to water (RH) and to ice (RH_{ice}) can be calculated using the following equations:

$$S = \frac{p_{\mathrm{w}}}{p^0_{\mathrm{w}}(T)}, \tag{2.3}$$

$$S_{\mathrm{ice}} = \frac{p_{\mathrm{w}}}{p^0_{\mathrm{ice}}(T)}, \tag{2.4}$$

$$RH = \frac{p_{\mathrm{w}}}{p^0_{\mathrm{w}}(T)} \times 100\%, \tag{2.5}$$

$$RH_{\mathrm{ice}} = \frac{p_{\mathrm{w}}}{p^0_{\mathrm{ice}}(T)} \times 100\%, \tag{2.6}$$

where $p_{\mathrm{w}}(T)$ and $p_{\mathrm{ice}}(T)$ are the saturation vapor pressures over ice and water, respectively. p_{w} is the water vapor partial pressure. In this thesis, p_{w} in the ice nucleation experiments is determined by measuring the dew point (T_{d}). $p^0_{\mathrm{w}}(T)$, p^0_{ice}, and $p^0_{\mathrm{w}}(T_{\mathrm{d}})$ are calculated using the parameterizations given by Murphy and Koop[25] as described above.

2.2 Phase State of a Particle

The physical state and morphology of aerosol particles play a crucial role in determining their interaction with water vapor. Water uptake and release will affect the water content of the particle which eventually determines the ice nucleation pathway. This section briefly demonstrates the phase states, the changes in phase state caused by water uptake and release, and the glass transition of organic particles.

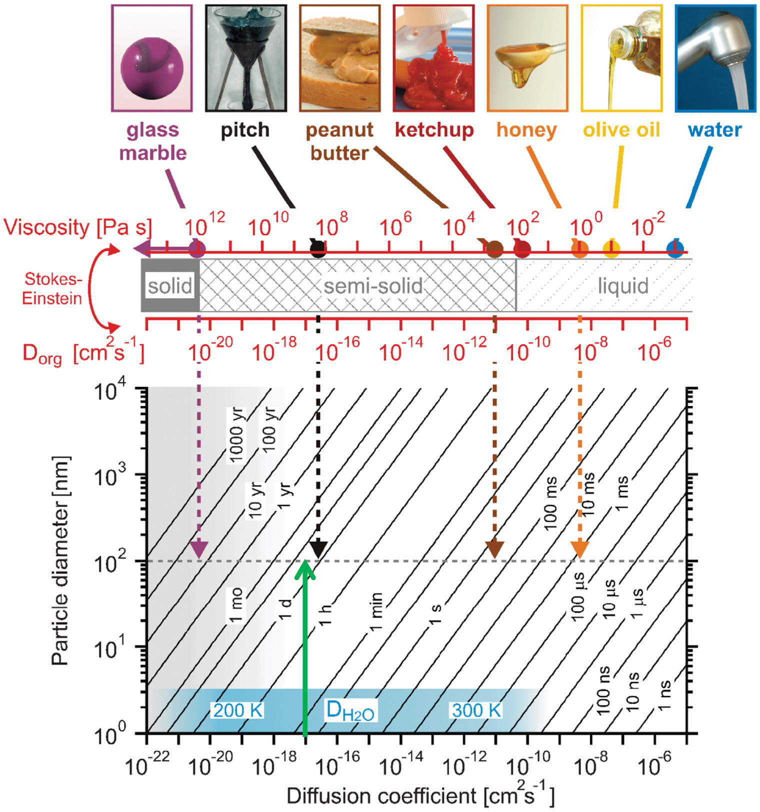

Figure 2.1: The approximate viscosities (η) and images for representative substances at room temperature adapted from Koop et al.[19]. The molecular self-diffusion coefficient D_{org} can be derived from η. In the lower panel the corresponding e-folding times of equilibration as function of particle size are shown.

2.2.1 Amorphous State of an Organic Particle

Aerosol particles may adopt different phase states including crystalline, liquid, and amorphous semi-solid and solid which are determined by particle composition, viscosity, mixing state, temperature, and humidity[19,46,175,176,178,180,205]. The amorphous states of organic particles are discussed in this section.

Viscosity (η), in units of Pa s, can be used to distinguish between liquid (10^2 Pa s), semi-solid (10^2–10^{12} Pa s), and solid ($>10^{12}$ Pa s) states[19,207]. The approximate viscosities (η) of several familiar substances at room temperature are shown in Fig. 2.1. The molecular self-diffusion coefficients (D_{org}) are also shown in the lower panel. η spans over fifteen orders of magnitude from liquid water (10^{-3} Pa s), viscous liquids such as honey (10 Pa s), semi-solids such as peanut butter (10^3 Pa s) and tar pitch (10^8 Pa s), and to amorphous solids such as glass marbles (>10^{12} Pa s)[19]. An amorphous substance with η larger than 10^{12} Pa s is termed glass which exhibits mechanical properties as a solid, but lacks the long-range molecular order which is typical of a crystalline state[177].

Recent studies have shown that atmospheric organic and organic-containing particles can adopt an amorphous semi-solid or solid (i.e. glassy) state rather than a liquid state[19,176,180,205]. For example, atmospheric relevant organic compounds such as carboxylic acids, carbohydrates, and substances with high molecular weight can adopt amorphous states at room temperature[176,208]. Laboratory studies have shown that atmospherically relevant organic aqueous droplets can also be transferred into a glassy state by cooling or drying[19,46,176,180]. Recently, it has been shown that SOA particles formed from the oxidation of biogenic VOCs can adopt amorphous semi-solid or solid states at room temperature[205,206].

In the lower panel of Fig. 2.1, the characteristic time of mass-transport and mixing by molecular diffusion (τ_e) in an aerosol particle as a function of particle size and D are shown according to

$$\tau_e = \frac{{d_p}^2}{4\pi D}, \tag{2.7}$$

where d_p is the particle diameter and D is diffusion coefficient[207]. For water partitioning in the aerosol particle, τ_e is the e-folding time of equilibration, i.e., the time after which the concentration in the particle core deviates by less than a factor of 1/e from the equilibrium value. For example, an organic particle with a diameter of 100 nm and η of 10^8 Pa s (similar to peanut butter) would have a τ_e less than 1 s. The diffusion coefficient of water ($D_{\mathrm{H_2O}}$) in a glassy particle is typically about 10^{-10}-10^{-12} cm^2 s^{-1} at room temperature[209,210]. $D_{\mathrm{H_2O}}$ is significant smaller at lower temperatures. For example, $D_{\mathrm{H_2O}}$ is less than 10^{-17} cm^2 s^{-1} at 200 K[209,210]. Thus, the diffusion of water into amorphous semi-solid or solid organic particles and water uptake by the particles is extremely slow at low temperatures. For example, assuming an organic particle with a diameter of 100 nm and $D_{\mathrm{H_2O}}$ of 10^{-17} cm^2 s^{-1}, the e-folding times of equilibration will be more than one day as shown by the green arrow in the lower panel of Fig. 2.1.

2.2.2 Water Uptake and Release

This section briefly discusses how water uptake and release change the physical state of a particle. Figure 2.2 demonstrates the water uptake and release by aerosol particles with different phases due to an increase or decrease of surrounding RH[176].

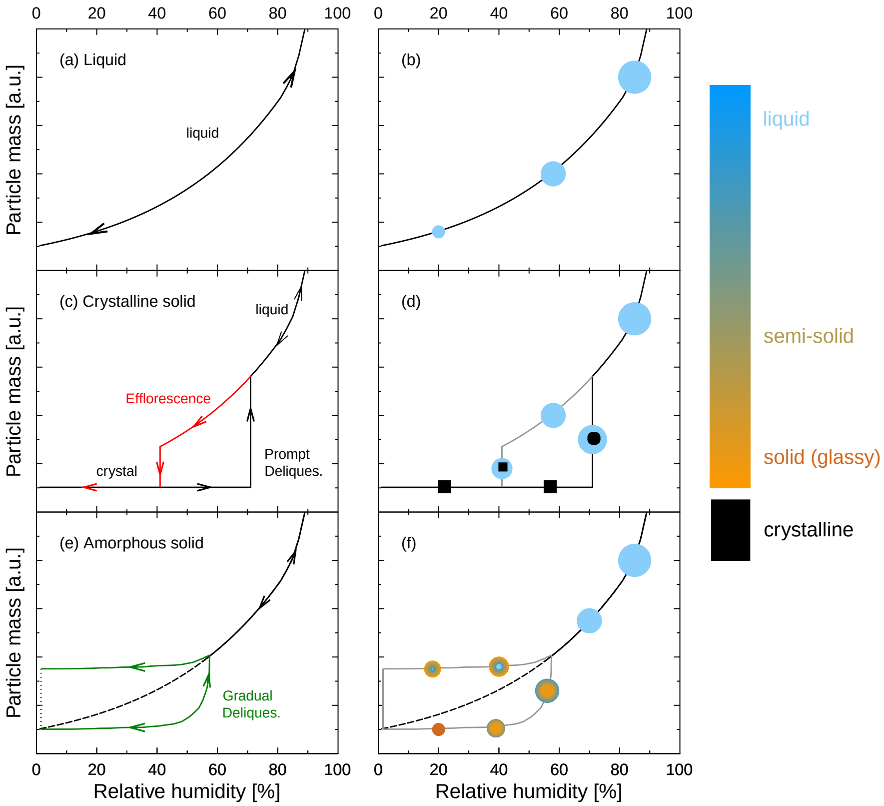

Figure 2.2: (a,b) water uptake and release by a liquid particle with negligible water vapor pressure; (c,d) water uptake by a crystalline solid particle and water release by an aqueous droplet to its original crystalline state; (e,f) amorphous solid particles showing humidity-induced glass transition adapted from Koop et al.[19].

The change in particle mass as a function of RH is shown in Fig. 2.2. As shown in Figs. 2.2a and 2.2b, upon increase of RH, an aqueous (liquid) droplet will take up water vapor until the condensed phase is in equilibrium with the gas phase, i.e. the water partial pressure in the aqueous droplet equals the water partial pressure in the gas phase. Further increase in RH leads to water uptake by the aqueous droplet following a single curve. Upon decrease of RH, the aqueous droplet will lose water following the exact same curve resulting in an smaller aqueous droplet.

Figures 2.2c and 2.2d demonstrate water uptake by a crystalline solid particle and water release by an aqueous droplet in which the droplet returns to its original crystalline state. Upon increase of RH, crystalline particles will adsorb a small amount of water at the surface leading to microstructural rearrangements of the particle surface. Bulk absorption of water may occur resulting in dissolution of the crystalline particles and complete deliquescence at a specific DRH. In reverse, upon decrease of RH, aqueous droplets will release water. When RH is below the DRH, small particles normally do not recrystallize readily but remain in a metastable liquid state. Crystallization is kinetically hindered. Below a specific RH (efflorescence relative humidity, ERH), particles will crystallize and return to a crystalline solid state. As a consequence of deliquescence and efflorescence at different RH, the particles experience a hysteresis effect when subject to hydration and dehydration cycles.

Figures 2.2e and 2.2f demonstrates water uptake and release of particle in an amorphous solid (i.e. glassy) state. Amorphous solid organic particles may absorb water vapor and tend to undergo gradual deliquescence compared to the prompt deliquescence transition of crystalline particles[209,210]. Upon increase of RH, the water accommodation and uptake occur only at the outermost layers of the amorphous solid particle, due to the exceedingly small diffusion coefficient of water ($D_{\mathrm{H_2O}}$) into the solid particles[19,209,210]. Upon further increase in RH the outermost layers will absorb more and more water vapor which reduces the particle's viscosity and increases the flux of water into semi-solid/solid particle from the gas phase. This process is termed a humidity-induced glass transition and indicates that at some humidity level significant water uptake occurs and the solid particle turns into a liquid[19,176,205]. Upon drying, the liquid particle becomes more and more viscous because the solute's concentration increases, which in turn reduces $D_{\mathrm{H_2O}}$. At a certain point $D_{\mathrm{H_2O}}$ becomes sufficiently small to prevent water molecules in the interior of particle from escaping and only the water molecules in the outermost region of the liquid particle manage to leave. This process would lead to the formation of a highly viscous shell and to a solid shell at even lower humidity and a core which can still contain water. These processes depend on the rate of humidification or drying because of the effects of the bulk diffusion kinetics of water vapor. For example, if a smaller RH rate change is used the particle has more time to absorb water upon humidification and release water upon drying which can lead to a smaller glass transition RH value[19].

2.2.3 Glass Transitions of Organic Particles

Aerosol particles in an amorphous semi-solid/solid state or with amorphous solid shells may be kinetically limited to interact with water vapor, and this influences how these particles act as IN[46,179,209]. It has been shown that aqueous organic and multi-component organic particles can form glasses and this may affect cirrus cloud formation processes at low temperatures in the UT/LS region[46,179,180,211]. Thus, it is necessary to determine the phase transition of organic particles.

As discussed above, water uptake by amorphous solid particles or water release from aqueous droplets may involve intermediate semi-solid stages during the glass transition. Previous studies have also shown that aqueous organic particles upon drying or exposure to low temperatures can form glassy states[46,176,179,180,209,210]. The temperature at which a glass transition occurs is the glass transition temperature (T_g)[19,177,180,209]. The glass transition is a non-equilibrium transition which occurs over a temperature range rather than a classical first-order transition with a well thermodynamically defined temperature point[19].

T_g will be used as a representative temperature below which an amorphous organic particle exhibits solid properties and above which the organic particle is likely to be in a semi-solid state. Various factors may affect or control T_g of organic particles including the molar mass, oxygen-to-carbon (O/C) ratio, mixing state, and ambient RH. Koop et al.[19] suggested that, in addition to temperature, molar mass, and water content are much more important than the O/C ratio for characterizing whether an organic particle is in a liquid, semi-solid, or solid state. In general, organic particles with higher molar mass exhibit higher T_g. Water which exhibits a T_g of 136 K can serve as a plasticizer in aqueous organic droplets and thus reducing the T_g of the pure dry organic component[19]. Higher water content in the organic particle or at higher humidity condition, the water will decrease the T_g of the particles. This indicates that it requires lower temperature for particles with higher water contain to transform into a solid (glassy) state. The humidity effect on T_g for organic particles is briefly discussed according to Koop et al.[19].

To predict T_g of an organic particle as a function of RH, three parameters are required including particle hygroscopicity, a parameter representing the interaction between water and organic solute, and a glass transition temperature of the dry organic component ($T_g(dry)$). Particle hygroscopicity can be described via water activity (a_w) as a function of organic solute concentration. If no or limited a_w data are available, there are various approaches to predict a_w. A widely used method is based on the effective hygroscopicity parameter (κ_{org}) or the van't Hoff factor (i_{org}) of the organic particle as follows:

$$a_w = (1 + i_{org}\frac{n_{org}}{n_w})^{-1}\,, \tag{2.8}$$

$$a_w = (1 + \kappa_{org}\frac{\rho_w}{\rho_{org}}\frac{M_{org}}{M_w}\frac{n_{org}}{n_w})^{-1}\,, \tag{2.9}$$

where ρ is the density, M is molar mass, and n is the number of moles of water or organic in the particle; the indices w and org refer to water and the organic solute, respectively.

T_g of an organic particle can be derived using the formulation developed by Gordon and Taylor[212]:

$$T_g(w_{org}) = \frac{w_w T_{g,w} + w_{org} T_g(dry)/k_{gt}}{w_w + w_{org}/k_{gt}}\,, \tag{2.10}$$

where w_w and w_{org} are the mass fractions of water and organic, $T_{g,w}$ and $T_g(dry)$ are glass transition temperatures of pure water and dry organic, respectively, and k_{gt} is the Gordon-Taylor constant specific for this water-organic system.

At equilibrium conditions, the RH equals a_w. If i_{org} and M_{org} are known, n_{org} and n_w can be derived from a_w using Eq. 2.8. The mass fractions of water and organic (w_w and w_{org}) can also be converted from n_{org} and n_w. Then, if $T_{g,org}$(dry) and k_{gt} are known, $T_g(RH)$ can be calculated using Eq. 2.10. Similar to this method, if κ_{org}, ρ_{org}, M_{org}, k_{gt}, and $T_g(dry)$ are known, $T_g(RH)$ can also be derived using Eq. 2.9 and 2.10. As an example, aqueous citric acid which can form a glass at 212 K exhibits k_{gt} of 3.18. i_{org} for the citric acid can range from 1.0 to 3.2 at infinite dilution, i.e. approaching $100\% RH$ and at the nearly pure citric acid particle, respectively.

Figure 2.3 shows the range of predicted T_g as a function of relative humidity for SOA using different i_{org}, k_{gt}, and T_g(dry) as suggested by Koop et al.[19]. For example, the blue line shows the predicted T_g if SOA has i_{org}, k_{gt}, and T_g(dry) of 1.0, 2.5, and 270 K, respectively. The T_g of a particle decreases as RH increases. Above the blue line, this SOA particle will exhibit an amorphous semi-solid or liquid state. At conditions with temperature and RH in the gray area as shown in Fig. 2.3, SOA particles will adopt a solid state. According to Fig. 2.3, the phase state of SOA particle can be precisely determined if the uncertainties in predicted T_g are significantly reduced. The uncertainties in predicted T_g are mainly due to a lack of data for the required parameters. Currently, there are only limited data available for atmospherically relevant organic compounds to predict T_g of aerosol particles. Clearly, if the T_g of atmospheric organic or organic containing aerosol particle is well known, this will advance the understanding of the interaction between particles and water vapor and thus cloud formation processes.

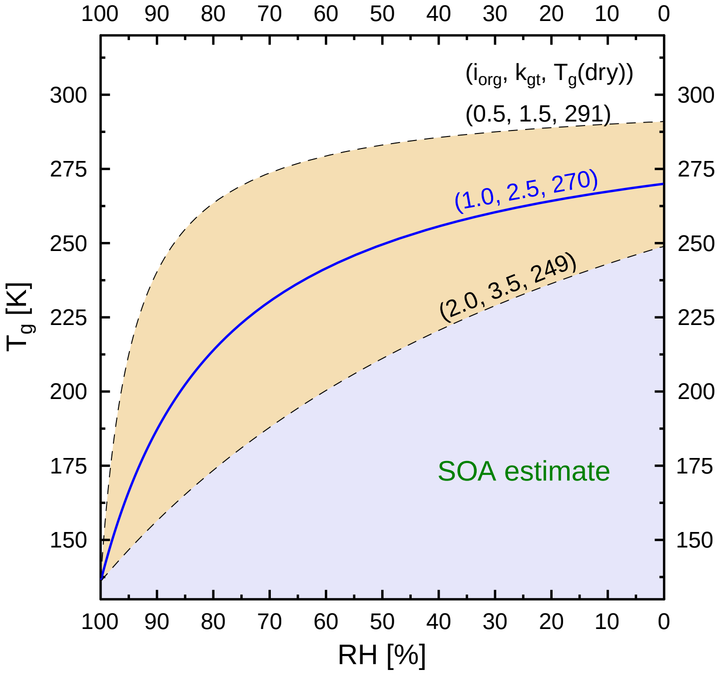

Figure 2.3: Predicted T_g as a function of relative humidity for SOA using various parameter values for i_{org}, k_{gt}, and T_g(dry) adapted from Koop et al.[19]. The number on each line indicates the values of the parameters.

2.3 Theoretical Description of Ice Nucleation

As discussed in Chapter 1, the description of heterogeneous ice nucleation as a stochastic or deterministic process is debated. In this study, the experimentally derived ice nucleation data are analyzed using both CNT and SH approaches allowing either approach to be implemented in cloud resolving models for further validation and sensitivity experiments. The parameter, IN activated fraction, commonly found in the literatures, is also derived to allow comparison with other studies.

2.3.1 Classical Nucleation Theory

Classical nucleation theory (CNT) provides a physical description of ice nucleation applying independent thermodynamic variables such as temperature and saturation[20]. CNT treats the formation of an ice cluster as water molecules from a liquid or gas phase joining or leaving the cluster randomly and provides nucleation rate coefficients or nucleation rates by determining the change in the Gibbs free energy of ice germ formation. A drawback of CNT is given by its main assumptions that microscopic ice cluster properties can be expressed by macroscopic properties such as density and surface tension. The main theoretical descriptions and equations presented here are derived from Pruppacher and Klett[20]. Ice germ formation via homogeneous nucleation from supercooled water is presented first and then extended for the description of heterogeneous ice nucleation.

Homogeneous ice nucleation

In a pure supercooled water droplet, the change in Gibbs free energy (ΔG_i) due to the formation of a spherical ice cluster containing i molecules can be defined as

$$\Delta G_i = (\mu_s - \mu_l)i + 4\pi r^2 \sigma_{sl}\,, \tag{2.11}$$

where μ_s and μ_l are chemical potentials of the solid (ice) and the liquid phase, respectively. σ_{sl} is the surface tension between the solid and the liquid phase. r is the radius of the ice cluster. The number of molecules, i, is determined as

$$i = \frac{4\pi r^3}{3 v_s}\,, \tag{2.12}$$

where v_s is the volume of one molecule in the solid phase. The difference in the chemical potentials can be expressed as

$$\mu_s - \mu_l = -kT \ln S\,, \tag{2.13}$$

where k is Boltzman's constant, T is absolute temperature, and S is the saturation ratio.

ΔG_i can be rewritten using Eq. 2.13 and Eq. 2.12 as

$$\Delta G_i = -\frac{4\pi r^3}{3 v_s}\; kT \ln S + 4\pi r^2 \sigma_{sl}\,. \tag{2.14}$$

The nucleation of an ice germ depends on the transfer of water molecules between the liquid and the solid phase which determines the size of ice cluster. The first term in Eq. 2.14 describes the change in Gibbs free energy due to the transfer of molecules from the liquid to the solid phase. The second term describes the change in Gibbs free energy due to the formation of the cluster surface, i.e. establishing an interface between ice and the aqueous phase.

Figure 2.4 demonstrates an example of ΔG as a function of saturation ratio (S) and cluster size (r). In a subsaturated environment (i.e. S<1), ΔG increases with increasing r. Thus, an ice cluster will not grow larger and so

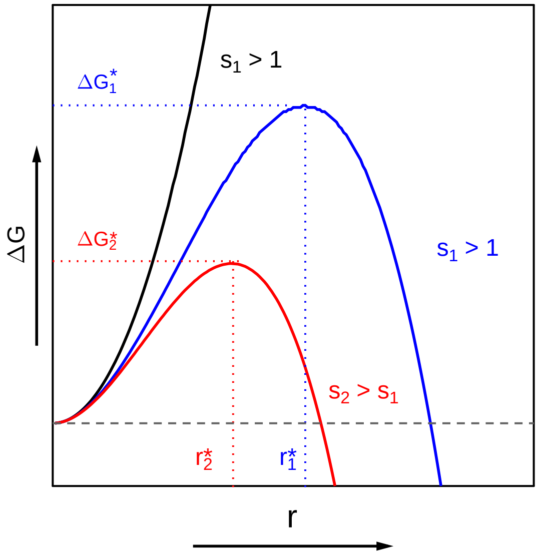

Figure 2.4: The change in Gibbs free energy (ΔG) due to the formation of an ice cluster as a function of saturation ratio (S) and cluster size (r).

ice nucleation is not favored. Under supersaturated conditions (i.e. S>1), ΔG increases initially with increasing r due to the formation of a solid surface but decreases once the ice cluster reaches the critical size (r^*) due to the compensation by the formation of the solid phase. For example, in the case of S_1 as shown in Fig. 2.4, the ice cluster can overcome the energy barrier (ΔG_1^*) and grow spontaneously, resulting in ice formation once it reaches the critical size (r_1^*). The r^* can be determined by setting the derivative of the ΔG^* to zero. Then, ΔG^* at r^* can be derived as

$$\Delta G^* = \frac{16\pi}{3} \frac{v_s^2 \sigma_{sl}^3}{(kT \ln S)^2} \, . \tag{2.15}$$

An increase in the saturation ratio ($S_2 > S_1$) will reduce the critical size and the energy barrier to r_2^* and ΔG_2^*, respectively.

According to CNT, the homogeneous ice nucleation rate coefficient, J_{hom}, measures the number of ice germs formed per unit of volume and per unit of time and is defined as

$$J_{hom} = A \cdot \exp(\frac{-\Delta G_d}{RT}) \cdot \exp(\frac{-\Delta G^*_{hom}}{kT}) = A \cdot exp(\frac{-\Delta G_{act,hom}}{kT}) \, , \tag{2.16}$$

where A is a pre-exponential factor and $\Delta G_{act,hom}$ is the activation energy required for the formation and growth of an ice germ. $\Delta G_{act,hom}$ consists of ΔG^{*}_{hom} and ΔG_d. ΔG_d is the molar Gibbs free energy of activation for diffusion of water molecules across the liquid-to-ice boundary and ΔG^{*}_{hom} is the change in Gibbs free energy due to the formation of critical size ice germ.

Heterogeneous ice nucleation

According to CNT, heterogeneous ice nucleation is the stochastic process in which a foreign particle increases the probability for the formation of an ice germ[20]. In other word, the presence of an ice nucleus can lower the energy barrier (ΔG^{*}) without disturbing the stochastic nature. Thus, the theoretical description of heterogeneous ice nucleation is an extension of that for homogeneous ice nucleation with additional treatments involving the ice nucleus.

Considering a spherical cap of ice germ on the solid surface of an ice nucleus which is immersed in a supercooled water droplet (i.e. immersion freezing), the ice cluster is bounded with the other two phases, i.e. the liquid water and the solid surface on which the ice cluster is resting as shown in Fig. 2.5. If there is no net force component along the solid surface, this mechanical equilibrium condition is given by

$$\sigma_{sl} \cdot \cos(\theta) = \sigma_{ln} - \sigma_{sn} \,, \tag{2.17}$$

where θ is the contact angle for the ice cluster on the surface of the ice nucleus. θ characterizes the relationship of the surface tensions between the ice nucleus, ice cluster, and liquid water. Further, the compatibility parameter or wetting coefficient, m, is introduced and defined as

$$m = \cos(\theta) = \frac{\sigma_{ln} - \sigma_{sn}}{\sigma_{sl}} \,. \tag{2.18}$$

ΔG_i for the formation of an ice cluster with i molecules, which accounts for all the surface tensions, can be described as

$$\Delta G_i = (\mu_s - \mu_l)\frac{V_i}{v_s} + A_{sl}\sigma_{sl} + A_{sn}(\sigma_{sn} - \sigma_{ln}) \,, \tag{2.19}$$

where V_i is the total volume of the spherical cap of ice germ; σ_{sl}, σ_{sn}, and σ_{ln} are the surface tension of ice-liquid, ice-nucleus, and liquid-nucleus interface, respectively; A_{sl} and A_{sn} correspond to the area of the ice-liquid and ice-nucleus interfaces, respectively. These variables are geometrically described as

$$V_i = \frac{\pi r^3}{3}(2+m)(1-m) \,, \tag{2.20}$$

$$A_{sl} = 2\pi r^2(1-m) \,, \tag{2.21}$$

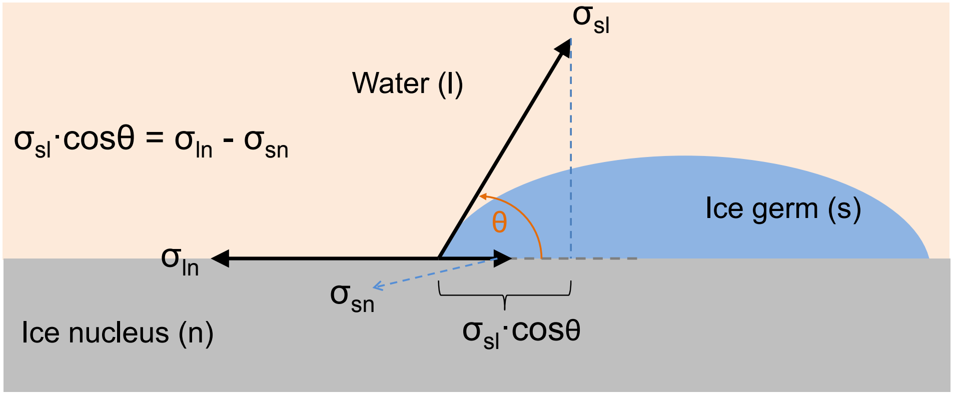

Figure 2.5: The mechanical equilibrium condition for a spherical cap of ice germ on an ice nucleus surface. θ is the contact angle adapted from Pruppacher and Klett[20]. σ_{sl}, σ_{sn}, σ_{ln} are the surface tension of ice-liquid, ice-nucleus, and liquid-nucleus, respectively. $\sigma_{sl} \cdot \cos(\theta)$ balances the difference of σ_{ln} and σ_{sn}.

$$A_{sn} = \pi r^2(1 - m^2)\,. \tag{2.22}$$

Combination of the equations described above, ΔG_i can be rewritten as

$$\Delta G_i = f(m)\left[-\frac{4\pi r^3}{3v_s}\,kT\ln S + 4\pi r^2\sigma_{sl}\right], \tag{2.23}$$

where

$$f(m) = \frac{(2+m)(1-m)^2}{4}\,. \tag{2.24}$$

The energy barrier for the heterogeneous nucleation of the ice germ (ΔG^*_{het}) can then be derived as

$$\Delta G^*_{het} = f(m)\left[\frac{16\pi}{3}\frac{v_s^2\sigma_{sl}^3}{(kT\ln S)^2}\right] = \Delta G^*_{hom} \cdot f(m)\,. \tag{2.25}$$

This indicates that the presence of an ice nucleus can lower the energy barrier for homogeneous nucleation (ΔG^*_{hom}) by a factor of $f(m)$ which is controlled by θ. For this reason, heterogeneous ice nucleation proceeds at warmer temperatures and lower supersaturations than homogeneous ice nucleation. In general, $0 \leq f(m) \leq 1$, confirming that the presence of an ice nucleus can lower the ΔG_{hom}. If $f = 0$, there is no energy barrier to nucleation. If $f = 1$, then $\Delta G_{het} = \Delta G_{hom}$ and so ice nucleates homogeneously. Thus, θ is a key parameter in determining the nucleation efficiency of the ice nucleus. A smaller θ and thus smaller $f(m)$ corresponds to a more efficient ice nucleus.

Finally, the heterogenous ice nucleation rate coefficient, J_{het}, which measures the number of ice germs formed per unit of ice nucleus surface and per unit of time is given as

$$\begin{aligned} J_{het} &= A \cdot \exp(\frac{-\Delta G_d}{RT}) \cdot \exp(\frac{-\Delta G^*_{het}}{kT}) \\ &= A \cdot \exp(\frac{-\Delta G_d}{RT}) \cdot \exp\left[\frac{-\Delta G^*_{hom}}{kT} \cdot f(m)\right] . \end{aligned} \tag{2.26}$$

For the deposition mode ice nucleation (i.e. ice nucleation directly from the supersaturated water vapor), the derivation of J_{het} is analogous to that of immersion freezing (Eq. 2.26). The equations for deposition ice nucleation of J_{het} and ΔG^*_{het} will hold if σ_{sl} is replaced by surface tension between ice and vapor (σ_{sv}), σ_{ln} is replaced by surface tension between vapor and ice nucleus (σ_{vn}), and the ΔG_d is replaced by the molar Gibbs free energy of activation for diffusion of water molecules across the vapor-to-ice boundary.

As shown above, θ would be the most straightforward parameter to compare the ice nucleation efficiencies of different types of IN. But the direct measurements of θ or corresponding surface tensions are extremely difficult to make especially at this microscopic scale and low temperatures.

In this study, J_{het} for the investigated aerosol particles, which can be used to predict ice crystal production rates, are derived from the experimental data. Then θ values are determined from the experimentally derived J_{het} according to CNT. The analytical method to derive experimental J_{het} has been used and described in detail in previous studies[197,213,214] and thus is only briefly described here.

Different numbers of ice nucleation events may occur within a given temperature interval, ΔT. J_{het} at T^i within the ith temperature interval, is derived using the following formula,

$$J_{\mathrm{het}}\left(T^i\right) = \frac{n^i_{\mathrm{f}}}{t^i_{\mathrm{tot}} \cdot S^i}, \tag{2.27}$$

where n^i_{f} is the number of observed ice nucleation events and $t^i_{\mathrm{tot}} \cdot S^i$ is the product of the total observation time and the particle surface area available for ice nucleation within the ith temperature interval. The product $t^i_{\mathrm{tot}} \cdot S^i$ is defined by the sum of contributions from the samples which remain unfrozen and those nucleated ice in the ith temperature interval according to

$$t_{\mathrm{tot}}^{i} \cdot S^{i} = \sum_{j=1}^{n_{\mathrm{f}}^{i}} \left(\frac{T_{\mathrm{st}}^{i} - T_{\mathrm{f},j}^{i}}{c_{\mathrm{r}}}\right) S_{j}^{i} + \frac{\Delta T}{c_{\mathrm{r}}} S_{\mathrm{uf}}^{i}, \tag{2.28}$$

where n_{f}^{i} is the number of ice nucleation events within the ith temperature interval, T_{st}^{i} is the start temperature of the ith temperature interval, $T_{\mathrm{f},j}^{i}$ is the freezing temperature of the jth nucleation event, S_{j}^{i} is the particle surface area of the jth ice nucleus, c_{r} is the cooling rate used in the experiments, and S_{uf}^{i} is the total particle surface area that remain unfrozen until the end of the ith temperature interval. This yields J_{het}. m and thus θ can be derived from J_{het} using Eq. 2.26, 2.15, and 2.24.

2.3.2 Singular Hypothesis

The singular hypothesis (SH) assumes that heterogeneous ice nucleation occurs on active sites located on the particle surface which become active at characteristic temperatures. This description is time-independent and hence is also termed "deterministic". This approach provides an overall phenomenological explanation of the heterogeneous ice nucleation process[20,107,215]. Since it is a time-independent approach, cumulative IN spectra, K, in units of cm^{-2}, are used to describe the heterogeneous ice nucleation process[107] instead of a nucleation rate. At a specific temperature, K indicates the total number of active sites which are activated and form ice germs at all warmer temperatures. Thus, only a specific number of IN will nucleate ice at a constant temperature.

The analytical method applied here to derive $K(T)$ for a description of deposition ice nucleation is similar to the methods described in previous studies[107,110,119,216]. $K(T)$ can be derived representing the number of ice active sites on the particle surface which have nucleated ice between temperature, T, and the temperature (T_0) which corresponds to RH_{ice} =100%. $K(T^i)$ at temperature, T^i, is derived from the differential ice nuclei spectrum, $k(T^i)$. For the i^{th} temperature interval, $k(T^i)$ is defined as the ice active surface site density for a unit of particle surface area according to

$$k(T^{i}) = \frac{1}{S_{\mathrm{tot}}^{i}} \frac{n_{\mathrm{f}}^{i}}{\Delta T}, \tag{2.29}$$

where S_{tot}^{i} is the total particle surface area that remains unfrozen at the start of the i^{th} temperature interval[107], and n_{f}^{i} is the number of ice nucleation events in the i^{th} temperature interval. Numerically integrating $k(T^i)$ from the temperature at which RH_{ice} =100% to T^i, results in

$$K(T^i) = \sum_{T_\mathrm{d}}^{T_i} \frac{n_\mathrm{f}^i}{S_\mathrm{tot}^i}\,, \tag{2.30}$$

where $K(T^i)$ indicates the density of active sites which had nucleated ice for temperatures higher than T^i. Since there is no fundamental underlying physical principle available for the SH approach, the resulting dependency of K on T cannot be microphysically interpreted, but serves as an empirical description.

2.3.3 IN Activated Fraction

IN activated fraction, i.e. the ratio of particles activating ice formation to total particle number, is a measure commonly used to describe the ice nucleating efficiency of particles, neglecting the information of particle surface area[112,217]. This parameter is often reported from cloud chamber experiments, such as a continuous flow diffusion chamber[112]. In addition to J_{het} and $K(T)$, the IN activated fractions at measured ice nucleation onsets are also provided for comparison with other studies. The optical microscope based technique in this study is sensitive to each individual ice nucleation event. Thus, the IN activated fraction reported here is mainly defined by the number of deposited particles on the substrates.

Chapter 3

Experimental Methods

3.1 Particle Generation and Collection

3.1.1 Laboratory–Generated Particle Samples

Unexposed and O_3–Exposed HULIS Particles

Micrometer-sized particles of Kaolinite, SRFA, and Leonardite were dry-deposited onto a hydrophobically coated glass substrate from a tip of a syringe using ultra high purity N_2 as a carrier gas. SRFA, and Leonardite particles served as surrogates of HULIS typically found in atmospheric particles. Kaolinite particles, known to be an efficient IN, were used to validate the experimental method. The hydrophobic coating (a monolayer of dichlorodimethylsilane) renders any effect of the substrate on ice nucleation negligible. The diameters of the deposited particles were less than 10 μm, with a mean diameter of 2–3 μm as determined using an optical microscope (OM). All particle samples were prepared in a clean bench to avoid sample contamination by ambient particles.

Oxidation of SRFA, and Leonardite particles by O_3 was conducted using a flow reactor as shown in Fig. 3.1. To generate O_3, ultra high purity N_2(g) and O_2(g) were first passed through a hydrocarbon gas trap and subsequent cold trap at 198 K for further purification. O_3 was generated by passing the O_2(g) through an ultraviolet source operated at 254 nm (Jelight Inc.) and subsequently mixed with a dry N_2(g) flow. The O_3–containing flow was introduced into a flow reactor consisting of a 35 cm long denuder with inner diameter of 2 cm in which the particle samples or blank substrates were placed. An O_3 monitor (2B Technologies) working at atmospheric pressure was used to measure the concentration of O_3 every 10 seconds based on the absorption of UV light by O_3 at 254 nm. The particle samples were exposed to O_3 concentrations of $\sim$85 ppm for 3 hours in the flow reactor at 54 hPa which

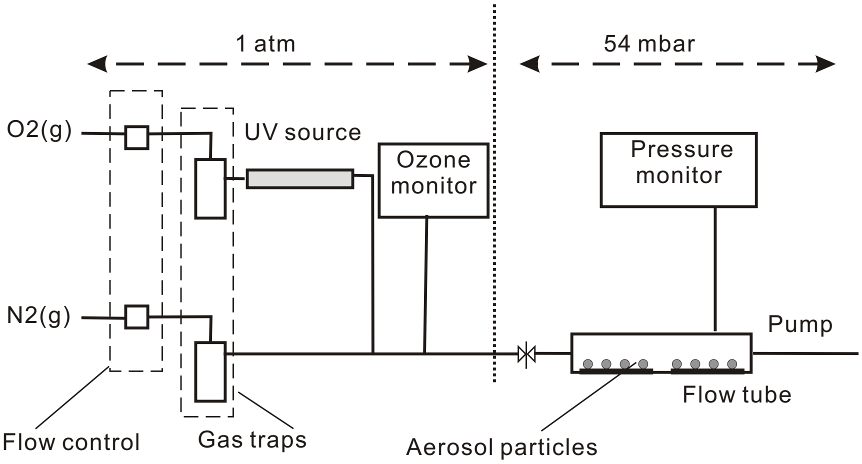

Figure 3.1: The experimental setup for exposing particles to O_3. O_3 generation and quantification are conducted at 1 atm. Aerosol oxidation experiments are performed in a flow reactor at 54 mbar.

yields an atmospheric O_3 exposure of 4.8×10^{-2} atm s. This atmospheric exposure is equivalent to exposure of particles at ∼40 ppb O_3 for about 2 weeks.

Secondary Organic Aerosol Particles

In collaboration with Boston College and Aerodyne Research. Inc., the generation and collection of amorphous SOA particles from precursor gas were conducted at Boston College.

SOA particles were generated via gas-phase oxidation of naphthalene with OH radicals and O_3, followed by homogenous nucleation. Figure 3.2 shows the simplified schematic sketch for SOA generation and collection. Input lines 1 and 2 provide carrier gases (N_2 and O_2) and OH radical precursors (O_3 and H_2O) with a total flow rate of 9.0 L/min. Line 3 provides the SOA precursor gas, naphthalene. Naphthalene vapor was introduced into the Potential Aerosol Mass (PAM) flow reactor by passing N_2 gas over solid naphthalene placed in a Teflon tube.

The PAM flow reactor is a horizontal 15 L glass cylindrical chamber, 46 cm long and 22 cm inside diameter. Four mercury lamps are mounted in teflon–coated quartz cylinders inside the chamber and provide ultraviolet (UV) lights for the generation of OH radicals. Prior to each experiment, the PAM flow reactor was conditioned with OH. The OH exposure is the product of OH con-

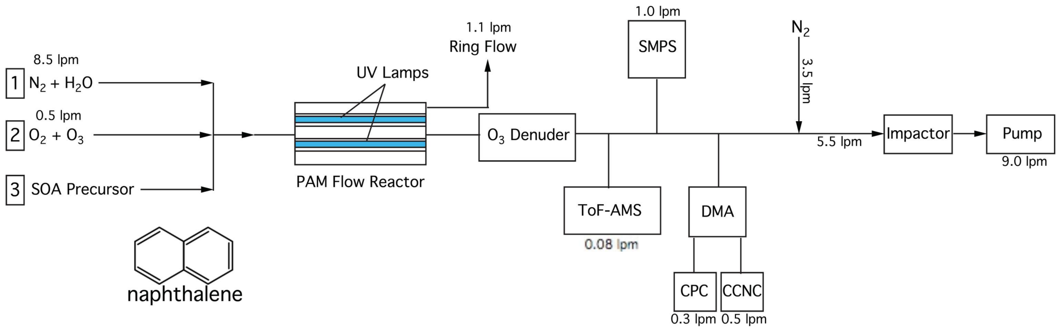

Figure 3.2: The schematic sketch of experimental setup for SOA generation and collection adapted from Lambe et al.[21]. As indicated, input lines 1 and 2 provide carrier gases (N_2 and O_2) and OH radical precursors (O_3 and H_2O). Line 3 provides precursors for SOA production, in this thesis, naphthalene. lpm represents flow unit, liter per minute

centration and average residence time in the PAM and is varied by changing the UV light intensity via stepping UV lamp voltages between 0 and 110V. Typical OH exposures ranged from $(1.6\pm0.8) \times 10^{11}$ to $(2.5\pm0.5) \times 10^{12}$ molec cm^{-3} s. Exposures in this range are equivalent to 1–20 days of atmospheric exposure assuming an average atmospheric OH concentration of $\sim1.5 \times 10^6$ molec cm^{-3}. This PAM flow reactor can produce SOA particles with various O/C ratio from 0 to 1.5. Experiments were conducted at RH of $\sim30\pm5\%$ depending on the temperature in the PAM flow reactor (22–32°C) at different UV lamp settings.

A four-stage Sioutas cascade impactor (SKC Inc.) was used for SOA particle collection. Figure 3.3A shows a simplified sketch of this impactor for aerosol particle collection and Fig. 3.3B shows the cascade impactor used in this study. The Sioutas cascade impactor consists of four impaction stages and one filter stage. Each impaction stage consists of an accelerator plate with specified nozzles and a collector plate. At each stage, the particle-laden air jets impinge upon the collector plate and particles larger than the cut–off point of this stage will be collected. Smaller particles in the air jet will follow the air streamlines and proceed to the next stage. Particles are separated and collected in the following aerodynamic particle diameter ranges: 0.25–0.5, 0.5–1.0, 1.0–2.5, and 2.5–10 μm. Particles smaller than 0.25 μm can be collected on the final filter stage.

SOA particles were collected on a hydrophobically coated glass substrate attached on the fourth stage of the cascade impactor. A glass substrate (in the red circle) attached to the collector plate is shown in Fig. 3.3C. The 50% cut–point of the fourth stage is 0.25 μm at an operational flow rate of $\sim$9 L/min. This flow rate was achieved by combining a high purity N_2 flow (3.5 L/min)

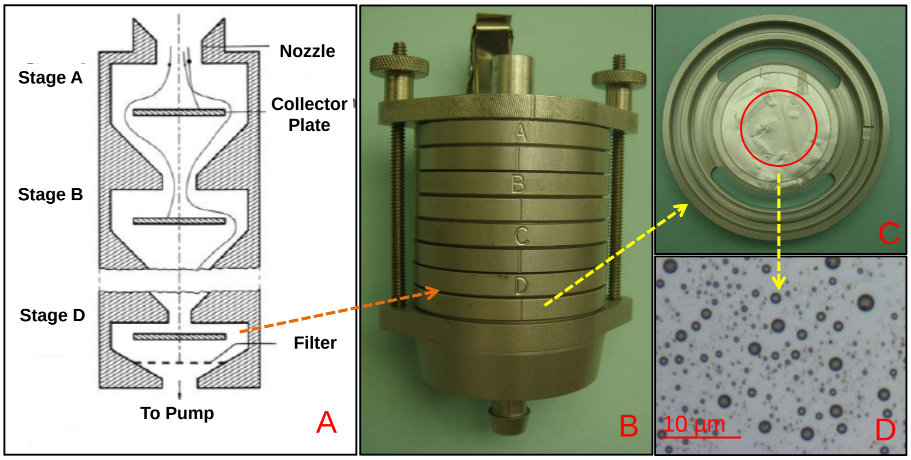

Figure 3.3: (A) A simplified sketch of a impactor illustrating the impaction of aerosol particles (B) A four-stage Sioutas cascade impactor. (C) A hydrophobically coated glass substrates attached to the fourth impaction stage of the impactor. (D) A typical optical microscope (OM) image of the collected SOA particles on a glass substrate.

and the SOA particle–containing flow from the PAM flow reactor (5.5 L/min) as shown in Fig. 3.2. In this study, three different types of SOA particle with O/C ratios of 0.27, 0.54, and 1.0 were generated and collected for ice nucleation and water uptake experiments. An optical microscope (OM) image of SOA particles with an O/C ratio of 0.54 is shown in Fig. 3.3D.

During particle collection, the mass spectra of SOA particles were measured using an Aerodyne time-of-flight aerosol mass spectrometer (ToF-AMS) to the provide O/C ratio of the particles. The particle size distribution was measured using a scanning mobility particle sizer (SMPS) combined with condensation particle counter (CPC). CCN activities of the SOA particles were also measured using a continuous flow CCN counter (CCNC). The particles were size-selected by a DMA (Differential Mobility Analyzer) prior to CCN measurements.

3.1.2 Field-Collected Particle Samples

Various types of authentic atmospheric particles were collected during the CalNex (California Research at the Nexus of Air Quality and Climate Change, 2011)[218] and the MILAGRO (Megacity Initiative: Local and Global Research Observations, 2006)[219] field studies for the heterogeneous ice nucleation and water uptake experiments and detailed micro–spectroscopy particle analyses by using computer controlled scanning electron microscopy with energy

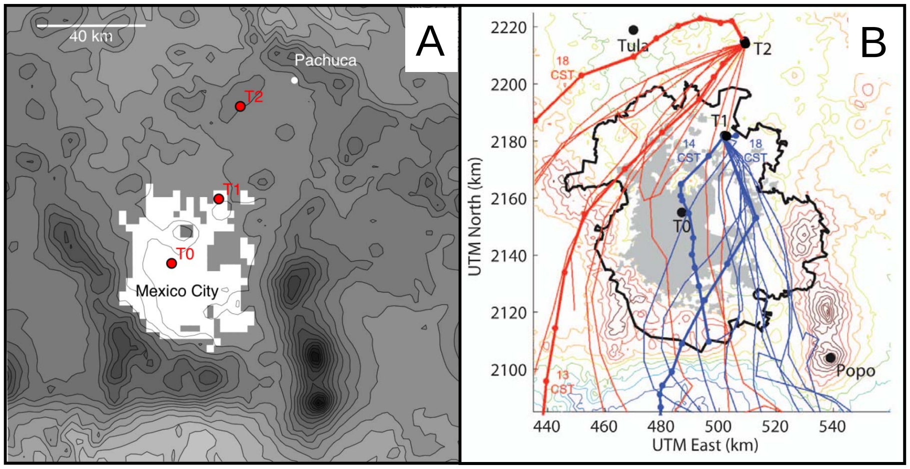

Figure 3.4: (A) A map of study area during MILAGRO campaign showing the locations of T0, T1, and T2 sampling sites adapted from Doran et al.[22]. (B) Blue and red lines indicate 12 hour back trajectories ending at the T1 and T2 sites, respectively.

dispersive analysis of X–rays (CCSEM/EDX) and scanning transmission X–ray microscopy with near edge X–ray absorption fine structure spectroscopy (STXM/NEXAFS).

MILAGRO Campaign

During the MILAGRO 2006 campaign, particle samples in the size range of 0.3-2.5 μm were collected at T0, T1, and T2 sampling sites. As shown in Fig. 3.4A, the T0 site was located inside of the Mexico City metropolitan area; T1 and T2 were located northeast from the city, 35 km and 60 km, respectively. Three sites were located progressively downwind of the typical urban air plume. At each site particles were collected onto different substrates by a Time-Resolved Aerosol Collector (TRAC) impactor[220]. Three types of substrates were used: (1) Si_3N_4 coated silicon wafer grids for ice nucleation experiments, (b) silicon wafers with Si_3N_4 window for particle analysis using STXM/NEXAFS, and (c) a transmission electron microscopy (TEM) grids (copper 400 mesh grids, carbon type B film, Ted Pella, Inc.) for CCSEM/EDX analysis.

Particle samples collected on March 22, 2006, when the northeastern airflow occurred from T0 to T1 and T2 as shown in Fig. 3.4B, are chosen for the detailed micro–spectroscopy particle analyses and the ice nucleation and water uptake experiments. Another particle sample which composed of mainly

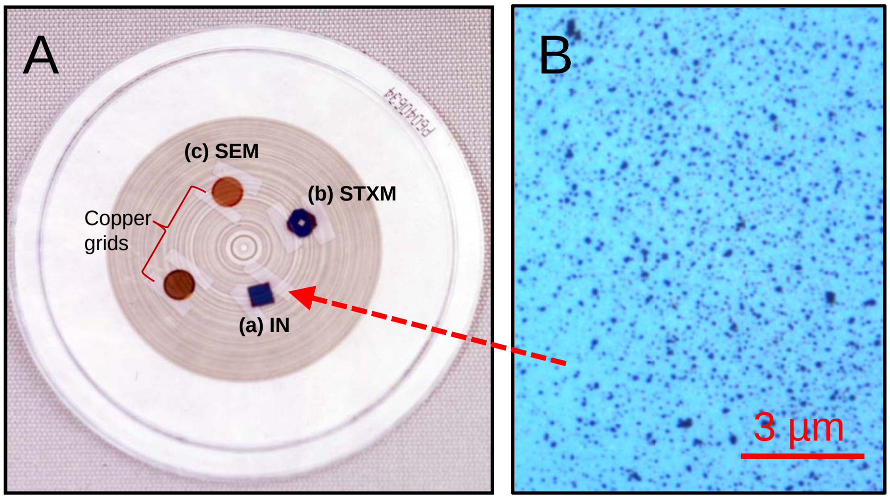

Figure 3.5: (A) An example of the set of pre-arranged substrates used to collect the particles: (a) Si_3N_4 coated silicon wafer grids, (b) silicon wafers with Si_3N_4 window, and (c) two copper grids (brown circles). (B) A typical OM image of the particles collected on a Si_3N_4 coated silicon wafer grid during CalNex campaign. The silicon wafer causes the blue background.

Pb/Zn containing inorganic particles, mixed with soot and a minor presence of organic material collected at the T0 sampling site on March 24, 2006 was also investigated[23,220,221].

CalNex Campaign

Particle samples were collected at the ground sampling site on the Caltech campus, Pasadena on May 19 and May 23, 2010 during the CalNex field campaign. A cascade Multi Orifice Uniform Deposition Impactor (MOUDI) was used to collect size–fractionated aerosol samples. The operational principle of the MOUDI is the same as the four-stage Sioutas cascade impactor used for SOA particle collection. The particle samples were collected at the 8th stage of the MOUDI corresponding to the cut–off point of 0.32 μm over 6 hour time periods on a set of pre-arranged substrates: (a) Si_3N_4 coated silicon wafer grids for ice nucleation experiments, (b) silicon wafers with Si_3N_4 window for particle analysis using STXM/NEXAFS, and (c) two transmission electron microscopy (TEM) grids for CCSEM/EDX and TEM analysis. Figure 3.5A demonstrates an example of the set of pre-arranged substrates used to collect the particles.

Two sets of particle samples were chosen for this study including three samples (A2, A3, and A4) collected on May 19 and two samples (B2 and B4) collected on May 23. A typical OM image of the particles collected on a Si_3N_4 coated silicon wafer grid during CalNex campaign is shown in Fig. 3.5B.

3.2 Particle Analyses

All of the field-collected particle analyses by STXM/NEXAFS were conducted by collaborators at Lawrence Berkeley National Laboratory. Particle analyses by CCSEM/EDX for particles collected during the CalNex campaign were conducted during my visit at Pacific Northwest National Laboratory (PNNL) and for particles collected during the MILAGRO campaign, analyses were done by collaborators at PNNL. Both single particle analytical methods are briefly described here.

3.2.1 CCSEM/EDX

A scanning electron microscopy (Quanta 3D model, FEI, Inc.) equipped with an X–ray spectrometer (EDAX, Inc.) and a Si(Li) detector was used for microscopic imaging of a few thousand individual particles and for quantitative speciation of their elemental composition. The system in the computer control mode allows setting of specific sample areas to be fully inspected unattended and thus allows analysis of significant number of particles to obtain statistical information of the investigated atmospheric aerosol samples. A detailed description of the method is described elsewhere[220–223].

For a particle sample, multiple field-of-views representing the particle sample area are set over the substrate (TEM grid) prior to particle analysis. During the analysis, a particle is recognized first when an imaging signal above the preselected threshold was detected. When the contour of the particles in the single field–of–view is detected, the electron beam rasters continuously over the particle projection area and the EDX spectra are acquired for each detected particle. The system is configured to detect and analyze particles with the equivalent diameter of projection area higher than 0.1 μm.

The elements considered in the X–ray analysis include C, N, O, Na, Mg, Al, Si, P, S, Cl, K, Ca, Mn, Fe, Zn. The elemental composition is reported in a normalized form, i.e. normalized atomic percentage. Figure 3.6 shows an SEM image and EDX analysis for particles collected at the T0 site as an example. Most of the particles show a visible coating (dark area) around particle cores as shown in Fig. 3.6A. EDX analysis was performed using a line scan style on particles. As shown in Fig. 3.6B, the line scans demonstrated that the highest carbon concentrations occur at the particle edges and sulfur is enhanced at the

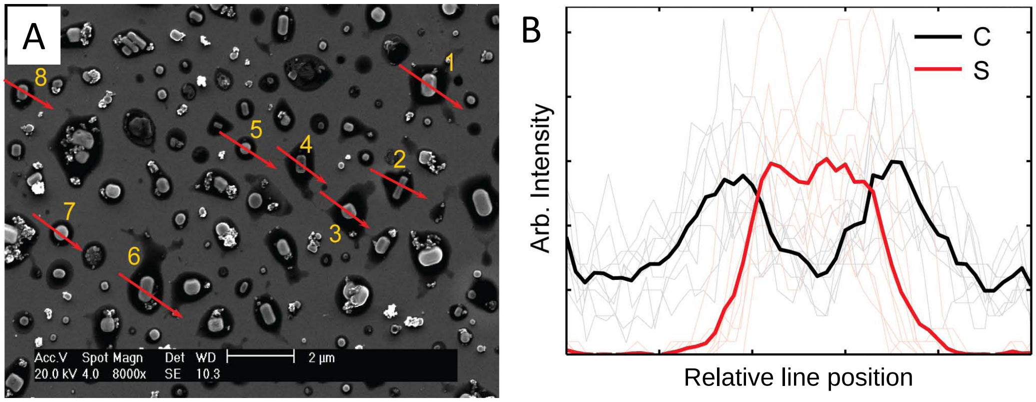

Figure 3.6: (A) An example of SEM image with lines of EDX scans for particles collected at the T0 site adapted from Moffet et al.[23]. The red arrows show the locations and directions of line scans. (B) The X-ray intensities of carbon (thick black line) and sulfur (thick red line) along the line scans averaged for a number of individual line scans represented by faint lines.

particle cores. These line scans confirm that particle cores contain S coated by carbonaceous material.

The chemical composition of an individual particle is obtained when X–ray analysis is conducted over the whole particle projection area instead of line scans. Figure 3.7 demonstrates the classification of two particle samples collected during the CalNex campaign. Each plot represents one sample with particle numbers of ∼2500. Each particle is represented as a stacked bar with colors indicating the relative atomic percent of the elements in the particle. The color map for the investigated elements is shown on the left of the figure. Then according to the normalized atomic percentages of elements, all investigated particles can be classified into different groups for each sample.

For the particle samples collected during the CalNex campaign, four types of particle are classified as follows: 1) CNO, in which particles mainly contain C, O and/or N; 2) COSNK, in which particles mainly contain C, O, S and/or N, K; 3) Na and Mg Rich, in which particles contain Na, Mg and the atomic percent of Na and Mg is larger than the total atomic percent of other investigated metals; 4) Others, the rest of the particles are included in this type. Furthermore, the chemically resolved size distributions for the collected particles can also be obtained. These two particle samples show distinguishable particles compositions. The fraction of sulfur (yellow color) containing particles for the B2 sample is significantly higher than for the A2 sample. This is also evidenced for the Na and Mg containing particles indicating the influence of a marine source. Using these chemical composition and features, one can infer possible particle sources.

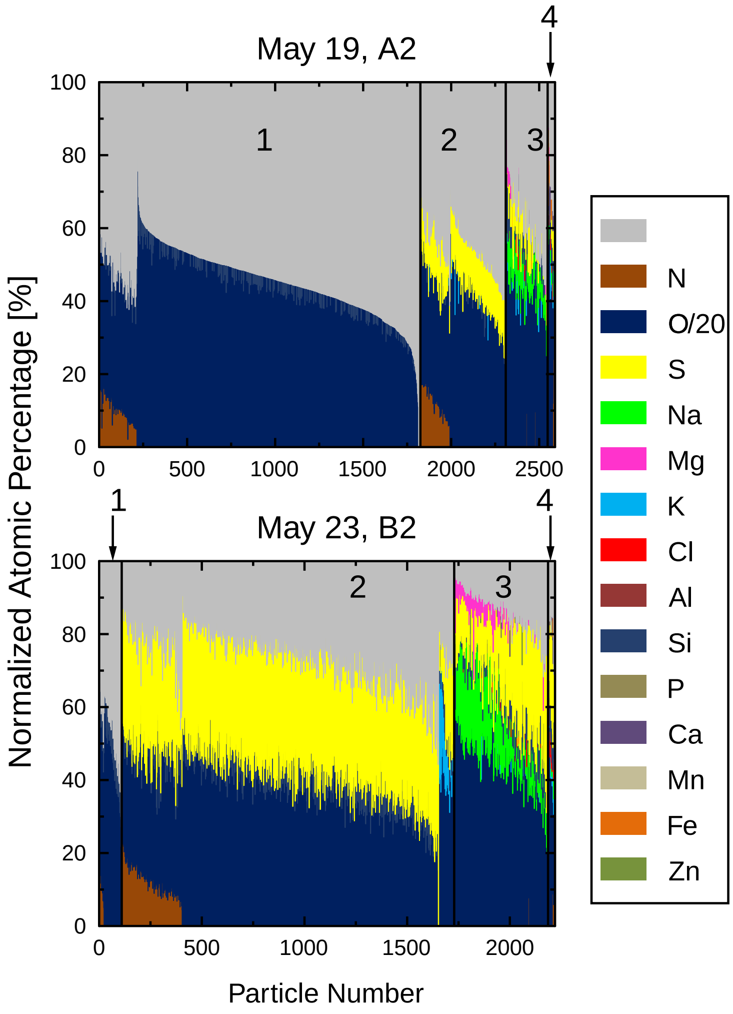

Figure 3.7: Bar plots of CCSEM/EDX data indicating elemental composition of individual particles for two particle samples collected on May19 and May 23 in Los Angeles during the CalNex campaign. The number shown in the plots indicates the particle type: (1) CNO, (2) COSNK, (3) Na and Mg Rich, and (4) Others. The colors indicate the investigated elements. See the text for more details.

3.2.2 STXM/NEXAFS

The STXM/NEXAFS analysis was conducted at beamlines 5.3.2 and 11.0.2.2 of the Advanced Light Source at Lawrence Berkeley National Laboratory. An overview for the application of this technique to atmospheric aerosols can be found in a recent review by Moffet et al.[224] and technical details on STXM are published elsewhere[225–227]. STXM/NEXAFS analysis at the carbon K–edge provides spatial mapping of the chemical composition which allows identification of three constituents including organic carbon (OC), elemental carbon (EC), and inorganic components (Inorg) within individual particles. When combined, those chemical maps yield the mixing state of aerosol particles[23,24,221].

While measuring the transmitted X–rays, images are obtained at a given photon energy by raster scanning the sample. To determine the exact peak position and obtain spatially resolved spectral information, a sequence of images for a full spectrum (∼100 energy stacks) of a particle is required. This sequence of images is referred to as a stack. From this three–dimensional data set, a spectral image is obtained. Quantitative analysis is obtained by converting the transmitted intensity signal into absorbance referred to optical density (OD), a dimensionless quantity, given by the Beer-Lambert's law:

$$OD = -ln(\frac{I(t)}{I_0}), \tag{3.1}$$

where I_0 is the incident flux transmitted through a particle-free region of the substrate (Si_3N_4 window), $I(t)$ is the flux transmitted through a particle, and t is the thickness of sample. Then OD data are used to identified different chemical components.

Figure 3.8 shows a carbon K-edge spectrum of a atmospheric carbonaceous aerosol containing potassium. The energy range below the carbon absorption edge (<283 eV) is denoted "pre–edge". The energy range above the carbon absorption edge (>320 eV) is denoted post–edge. The peak intensity at ∼285.4 eV is proportional to the amount of carbon double bonds (denoted C=C or sp^2) present in the particle. The feature at ∼288.6 eV is characteristic for the carboxyl group (COOH). Potassium has two electron transitions in the energy range of the carbon edge, namely at 297.5 eV and 300 eV. The difference between the post–edge and pre–edge absorbance is proportional to the total amount of carbon in a sample.

In this study, four energy stacks were analyzed instead of ∼100 energy stacks. Four energy stacks were taken to obtain elemental maps and allow for classification of a larger number of particles. The spatially elemental mapping

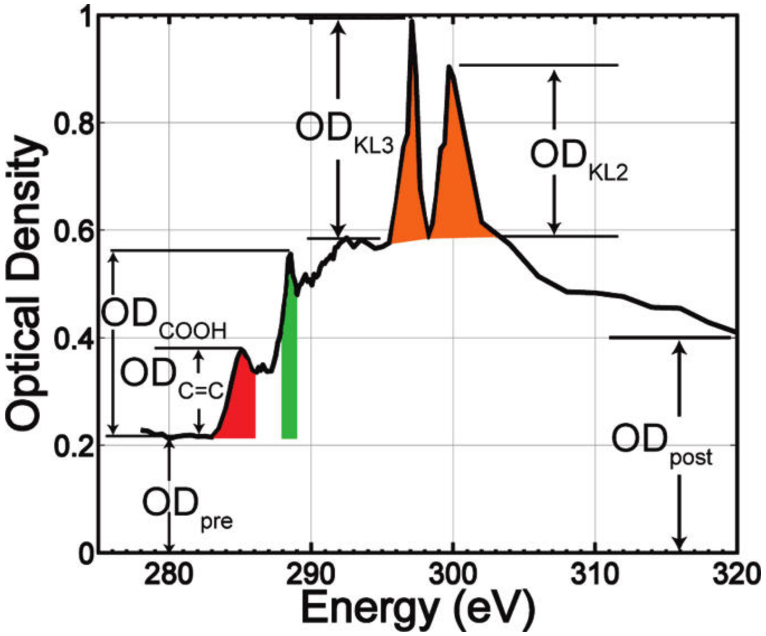

Figure 3.8: A carbon K–edge spectrum of a atmospheric carbonaceous aerosol containing potassium adapted from Moffet et al.[24]. The assignments of spectral features: "pre-edge" (OD$_{pre}$) between 278 and 283 eV, carbon–carbon double bonds (OD$_{C=C}$) shown in red, carboxylic acids (OD$_{COOH}$) shown in green, potassium edges (OD$_{KL3}$ and OD$_{KL2}$) shown in orange. OD$_{post}$ is the post-edge at 320 eV.

identifies three chemical constituents (organic carbon, elemental carbon, and inorganic species) within individual particles and when combined, yields the mixing state[24].

Figure 3.9 shows the chemical constituents mapped for particles collected on May 19 during the CalNex campaign. The pre– and post–edge OD images are shown as well as the soot map, the organic carbon map, the inorganic map, and the overlay of those three species. By comparing the pre- and post-edge OD data, the amount of carbon present in the sample is qualitatively determined. Many of the particles absorb more strongly at the post–edge, indicating that they are carbonaceous particles. Combination of the maps of soot, organic carbon, and inorganic allows the classification of particles and identification of a particle's mixing state.

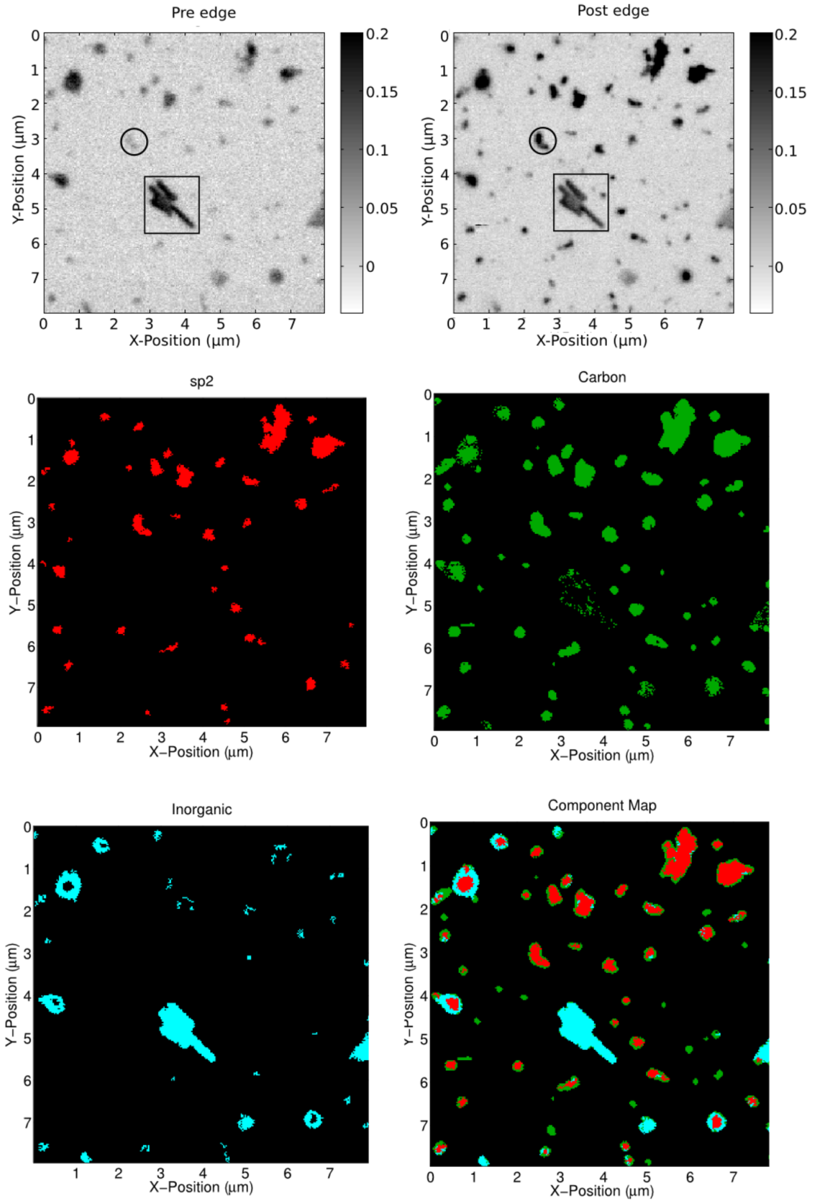

Figure 3.9: Chemical composition mapping of a particle sample collected on May 19 during the CalNex campaign (Mary K. Gilles, personal communication): OD image at the pre edge (top left), optical density image at the post edge (top right), organic carbon map (center right), inorganic species map (bottom left), and overlay of the soot (red), the organic (green), and the inorganic (turquoise) map (bottom right). An example of a carbonaceous particle and a salt crystal is highlighted by a circle and a square, respectively.

3.3 Apparatus for Ice Nucleation and Water Uptake Experiments

The onset conditions of ice nucleation and water uptake by aerosol particles are determined using a custom–built apparatus consisting of an OM and an ice nucleation cell (INC). Figure 3.10 shows the schematic of the experimental system and an image of the INC. The system allows the exposure of aerosol particles to temperatures (T_p) as low as 200 K and RH_ice up to water saturation. This apparatus has been described in the published work which is presented in Chapter 4. The detail description of the INC and experimental procedure is presented in Section 4.3 of this thesis. Here the experimental procedure is briefly described.

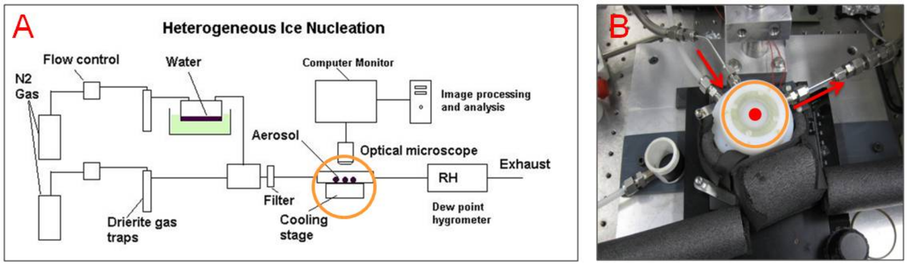

Figure 3.10: The schematic sketch of the experimental setup used for the ice nucleation and water uptake studies (left panel). (B) An image of the ice nucleation cell (INC). The orange circles indicate the INC. The red arrows indicate the inlet and outlet flows.

The particle sample on the substrate (i.e. hydrophobically coated glass slide or Si_3N_4 chip) is placed inside the INC. The entire sample area is optically monitored and the changes in particle phase and size are digitally recorded using an OM in reflected light mode. The particles are exposed to a controlled humidified N_2 (ultra high purity) gas flow at about 1 SLPM (standard liter per minute) with a constant dew point (T_d) generated by passing N_2 gas through a temperature controlled water reservoir. At the exit of the INC, T_d is determined using a chilled mirror hygrometer (GE Sensing) in a range of 203–293 K with an uncertainty of less than ±0.15 K[39,115,117,214]. Once T_d is stable, T_p is adjusted and cooled at a rate of 0.1 K min^{-1}, corresponding to an increase in RH_ice of ∼2.3 to 1.5% per minute for temperatures from 200 to 260 K, and exposed to ice supsaturation until ice formation or water uptake is observed.

Images of the particle sample are recorded at every 0.02 K, in addition to T_d and T_p.RH_ice and RH above the particles are calculated from monitored T_p and T_d using the parameterizations for water vapor pressures given by Murphy and Koop[25]. From the recorded images, the onset conditions of ice nucleation or water uptake by the particles is determined according to the changes in particle size and phase. The OM allowed us to visually identify the changes in particle size and phase due to water uptake or ice formation larger than 0.2 and 1 μm when using a magnification of 1130x and 230x, respectively. Estimates of the water vapor flux indicated that the water vapor supply was sufficient for a detectable size change of the particles by 0.2 and 1 μm due to water uptake or ice formation on deposited particles between 6 and 36 seconds at 235 K, respectively, assuming a water vapor condensation coefficient of 0.01. Ice formation is reported as immersion freezing if water uptake was observed prior to ice crystal formation and as deposition ice nucleation if no water uptake was observed prior to ice crystal formation. If two or more ice crystals are formed simultaneously, then all ice crystals are counted. Subsequent ice formation events are discarded since a uniform water vapor field may not persist when ice crystals are present in the INC.

T_p is calibrated against T_d measured from the hygrometer since in equilibrium conditions $T_\mathrm{p} = T_\mathrm{d}$. Experimental uncertainties were calculated from the maximum difference between T_p and T_d. Due to the given uncertainties of $\Delta T_\mathrm{d} < \pm 0.15$ K and $\Delta T_\mathrm{p} < \pm 0.3$ K, this resulted in a conservative uncertainty (i.e. the maximum difference between T_p and T_d) of $\Delta RH_\mathrm{ice} < \pm 11\%$ at 200 K and $\Delta RH_\mathrm{ice} < \pm 3\%$ at 260 K. Uncertainties of the reported data for the onset conditions of ice nucleation and water uptake represent one standard deviation of observed RH_ice or RH and T_p values obtained from multiple ice nucleation experiments or represent the experimental uncertainties, whichever is larger.

Chapter 4

Heterogeneous Ice Nucleation by Laboratory–Generated HULIS particles

This chapter presents the investigation of heterogeneous ice nucleation from Kaolinite, Suwannee river standard fulvic acid (SRFA), and Leonardite standard humic acid (Leonardite) particles as surrogates of HULIS typically found in atmospheric particles as a function of particle temperature (T_p), relative humidity with respect to ice (RH_ice), nucleation mode, and O_3 exposure. The effect of particle oxidation by O_3 on corresponding IN efficiencies of SRFA and Leonardite particles is assessed. Heterogeneous ice nucleation rate coefficients (J_het) are derived and applied to obtain contact angles (θ) based on CNT. The SH approach is used to derive the cumulative IN spectrum, $K(T)$, for the investigated particles. A parameterization of θ is presented which allows derivation of J_het for various organic and inorganic particles acting as deposition IN, and corresponding ice crystal production rates for application in cloud resolving models. Two simplified examples for the application of parameterization are discussed.

The sections from 4.1 to 4.6 are the reproduction of the publication of "Heterogeneous ice nucleation on particles composed of humic-like substances impacted by O_3" by B. Wang and D. A. Knopf published in the Journal of Geophysical Research, Vol. 116, D03205, 2011, with permission from the American Geophysical Union. The layout of the article as well as the section, figure, and table numberings have been adapted to match with the thesis structure.

Heterogeneous ice nucleation on particles composed of humic-like substances impacted by O_3

Bingbing Wang and Daniel A. Knopf*

Institute for Terrestrial and Planetary Atmospheres, School of Marine and Atmospheric Sciences, Stony Brook University, Stony Brook, NY 11794, USA.

* To whom correspondence should be addressed. Email:Daniel.Knopf@stonybrook.edu

Published in Journal of Geophysical Research, Vol. 116, D03205, 2011. Reproduced with permission from American Geophysical Union, copyright 2011.

4.1 Abstract

Heterogeneous ice nucleation plays important roles in cirrus and mixed-phase cloud formation, but the efficiency of organic particles to act as ice nuclei (IN) is still not well understood. Furthermore, the effect of particle oxidation by O_3 on corresponding IN efficiencies has not yet been sufficiently assessed. We present heterogeneous ice nucleation on Kaolinite, Suwannee river standard fulvic acid (SRFA), and Leonardite standard humic acid particles as a function of particle temperature (T_{p}), relative humidity with respect to ice (RH_{ice}), nucleation mode, and O_3 exposure. Ice nucleation and water uptake were studied for $T_{\mathrm{p}} > 203$ K and RH_{ice} up to water saturation using a novel ice nucleation apparatus. This study shows that SRFA, Leonardite and corresponding O_3-exposed particles can nucleate ice via different modes at relevant atmospheric conditions. These particles nucleated ice via deposition mode at $T_{\mathrm{p}} \leq 231$ K and for higher T_{p} water was taken up or ice nucleated via deposition or immersion mode. Oxidation of Leonardite and SRFA particles by O_3 lead to a decrease in deposition nucleation efficiency and to water uptake at lower temperatures for the former and to an increase in the lowest temperature at which deposition nucleation was observed for the latter. Activated IN fractions and heterogeneous ice nucleation rate coefficients (J_{het}) were derived and corresponding contact angles (θ) were calculated. A parameterization of θ as a function of RH_{ice} is presented which allows derivation of J_{het} for various deposition IN and corresponding ice crystal production rates for application in cloud resolving models.

4.2 Introduction

Aerosol particles can affect the global radiative budget directly by scattering and absorption of solar and terrestrial radiation but also indirectly by aerosol-cloud interactions which can lead to the formation of new clouds and modification of the radiative properties of existing clouds[66,89,90,97–100]. Aerosol-cloud interactions pose one of the largest uncertainties in prediction of future climate changes[89]. The strength of the aerosol indirect effect depends on the efficiency of the aerosol particles to act as cloud condensation nuclei (CCN) and IN. Whereas an increasingly improved understanding of the role of CCN on climate is being achieved[89,94,99,228], the effect of IN on the atmosphere is still insufficiently understood[66,89–91].

Ice crystals can form by homogeneous or heterogeneous ice nucleation[20]. Homogeneous ice nucleation proceeds from supercooled aqueous particles at temperatures below ~235 K. Heterogeneous ice nucleation can be initiated by a pre-existing aerosol particle, the IN, via four modes: deposition mode (the IN nucleates ice directly from supersaturated water vapor), immersion freezing (the IN immersed in a supercooled aqueous droplet nucleates ice), condensation freezing (ice nucleates during water vapor condensation onto the IN), and contact freezing (ice formation is induced by collision of supercooled droplets with IN)[20,101]. Heterogeneous ice nucleation occurs at warmer temperatures and lower supersaturations with respect to ice than homogeneous ice nucleation[20] and hence renders IN an important role in atmospheric ice formation.

Atmospheric IN can initiate ice nucleation resulting in the formation of cirrus and mixed-phase clouds. Cirrus clouds can account for one-third of the global cloud coverage and play an important role in regulating radiative fluxes[62]. These ice clouds can have a predominant warming effect[63,71,229,230]. The radiative properties of cirrus clouds are determined in part by the underlying ice nucleation mechanisms which can affect the numbers and shapes of the ice crystals[72–74]. In mixed-phase clouds, which consist of supercooled liquid droplets and ice crystals, heterogeneous ice nucleation is the only pathway for ice initiation. This in turn defines the degree of cloud glaciation with subsequent consequences for precipitation and the hydrological cycle[64,66,70,76]. Mixed-phase clouds have also been identified to have a large climatic effect in the polar regions[67–70]. For these reasons a better understanding of the underlying mechanisms governing heterogeneous ice nucleation is needed to evaluate the role of cirrus clouds and mixed-phase clouds on the global radiative budget and hydrological cycle.

Field measurements have shown that organic particles can reach altitudes where temperatures favor ice formation[2,156,231,232]. Previous studies also have shown that polar mixed-phase clouds were impacted by carbonaceous particles from biomass burning[233]. Ice crystal observations indicate that IN residues for cirrus and mixed-phase clouds contain some organic material in some instances[112,156,157,182,233]. Recently it has been shown that also anthropogenically emitted organic-containing particles can act as efficient IN under conditions for cirrus cloud formation[39]. A class of organic material extracted from atmospheric aerosol particles, termed HUmic-LIke Substances (HULIS), consists of a water soluble and an alkaline soluble fraction. Water soluble HULIS can contribute up to 60% to the aerosol water soluble organic carbon[135,138,139,142,145,234–236]. Alkaline soluble HULIS can contribute about 30 to 70% to total HULIS[145,237,238]. Suggested sources of HULIS include primary terrestrial sources, biomass burning, secondary organic aerosol formation, and marine sources[135,137–146,239]. HULIS consist of poly-carboxylic acids and resemble to some part terrestrial and aquatic humic substances and fulvic acids[135].

Previous aerosol studies employed commercially available fulvic acid and humic acid, such as SRFA and Leonardite, as surrogates of atmospheric HULIS to investigate particle properties such as growth factors and CCN properties[240–243]. Only few studies have investigated the ice nucleation efficiency of HULIS. Kanji et al.[8] showed that humic acid sodium salt and Leonardite can nucleate ice via deposition mode but this study was limited to 233 K. Fornea et al.[199] observed that Pahokee Peat soil, a humic acid from agricultural soil, are efficient IN in contact freezing mode.

During transport in the atmosphere, the organic particles will interact with atmospheric oxidants such as O_3, NO_3, and OH leading to oxidation of the organic material by heterogenous reactions[92,162]. This process, also known as chemical aging, can change the particle's composition and thus its chemical and physical properties[92,159–162]. Particle oxidation may affect the particle's IN efficiency. Only one study so far has investigated the effect of particle oxidation by gas phase O_3 on ice nucleation[3]. In the other ice nucleation studies particles were chemically aged by exposure to liquid oxidative agents such as hydrogen peroxide[169], and nitric and sulfuric acid mixtures[13]. Clearly, more experiments are needed to assess if particle oxidation results in a significant impact on the ice nucleation efficiency of organic particles.

In this study, we chose SRFA and Leonardite to generate particles serving as surrogates of atmospheric HULIS-containing particles representative of different sources such as biomass burning and marine sources. These organic proxies contain functional groups such as carboxylic and hydroxyl groups which have certain similarities compared to atmospheric HULIS[135,162]. SRFA is a water soluble organic compound extracted from a Suwannee River water sample and Leonardite is a water insoluble (alkali soluble) humic acid produced by the natural oxidation of exposed lignite[241,244]. Validation of the new experimental setup was performed by determining the IN efficiency of Kaolinite particles, a clay mineral, known to be efficient IN. We determined the IN efficiency of SRFA and Leonardite particles as a function of T_{p}, RH_{ice}, nucleation mode, and O_3 exposure.

4.3 Experimental method

4.3.1 Particle generation

Micrometer-sized particles of Kaolinite, SRFA, and Leonardite were investigated as potential IN. The particles were dry-deposited onto a hydrophobically coated glass plate (for the remainder of the manuscript referred to as substrate) from a tip of a syringe using ultra high purity N_2 gas as carrier gas.

The hydrophobic coating (a monolayer of dichlorodimethylsilane) renders any effect of the substrate on ice nucleation negligible[115,245,246]. The diameters of the deposited particles were less than 10 μm, with a mean diameter of **1.7–4.3** μm as determined using an optical microscope (OM). All particle samples were prepared in a clean bench (< 0.04 particles cm^{-3}) to avoid sample contamination by ambient particles[115]. Table 1 summarizes the range of average particle sizes, numbers, and total surface areas of the various particles samples employed in this study.

Table 4.1: The range of average particle size, number, total surface area, and IN activated fraction for the particle samples of each particle type are presented. The uncertainty in size represents 1 standard deviation.

particle type	size mean$\pm1\sigma$ (μm)	number	surface area ($\times10^{-4}$ cm^2)	IN activated fraction (%)
Kaolinite	(2.3–4.3)±2.0	660–8500	1.3–7.9	0.01–0.3
SRFA	(2.0–2.4)±1.0	2350–5350	1.4–3.8	0.02–0.13
O_3-exposed SRFA	(2.4–2.9)±1.4	1900–5300	2.0–7.3	0.02–0.16
Leonardite	(1.7–3.3)±1.0	2880–10500	3.5–6.4	0.01–0.1
O_3-exposed Leonardite	(2.0–2.3)±1.1	7300–12600	7.1–8.8	0.008–0.04

4.3.2 Ice nucleation apparatus

Heterogeneous ice nucleation was studied using a custom-built apparatus consisting of an OM and an ice nucleation cell (INC) with an inside volume smaller than 0.8 cm^3 as shown in Fig. 4.1A, based on previously developed setups[3,39,115,246,247]. This ice nucleation apparatus allows the exposure of aerosol particles to particle temperatures (T_p) as low as 200 K and RH_ice up to water saturation.

The INC was made out of high density polyethylene to minimize water adsorption which could lead to inhomogeneities of the water vapor field inside the INC. A flow diffuser was also placed in the INC to enhance mixing of the humidified gas. Independent experiments showed that deliquescence of ammonium sulfate particles, water condensation, and evaporation of water droplets occurred equally in each case across the sample area corroborating a homogeneous water vapor field within the INC. The OM coupled to the INC was operated in reflected light mode and was equipped with a digital camera and imaging software to monitor and record in situ changes in particle phase and size. The entire particle sample area was digitally monitored. The particle samples were placed onto the cooling stage within the INC. The temperature

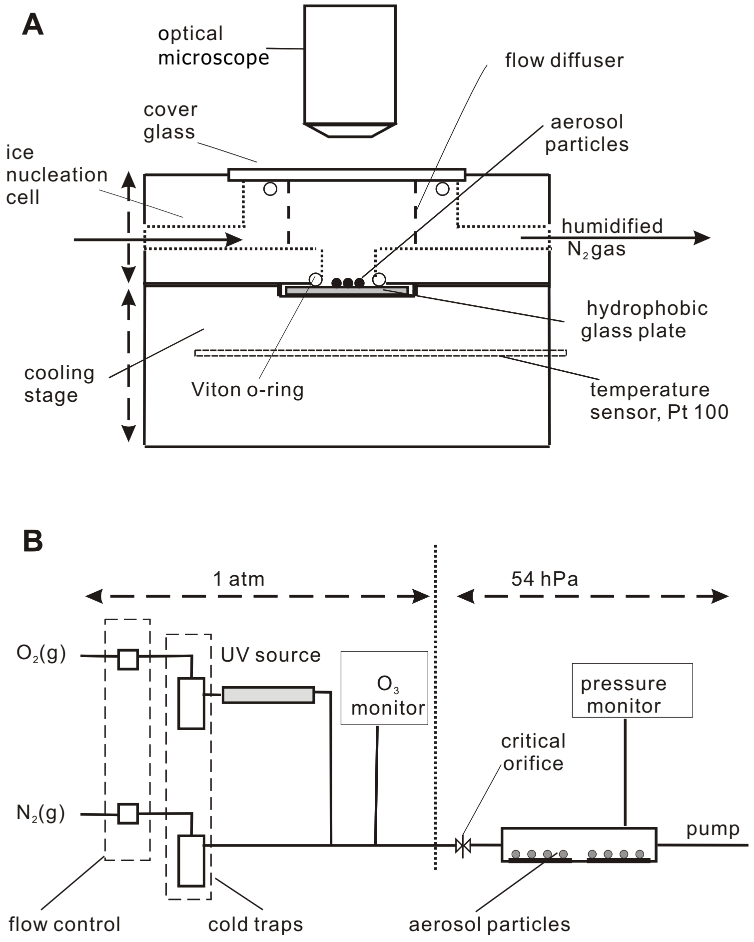

Figure 4.1: Panel A shows a technical sketch (not to scale) of the ice nucleation cell (INC) coupled to an OM. The outside diameter and the height of the ice nucleation cell are 64 mm and 14.5 mm, respectively. The dotted lines indicate the INC volume (< 0.8 cm^{-3}). Panel B shows the experimental setup for exposing particles to O_3. O_3 generation and quantification were conducted at 1 atm. Particle oxidation experiments were performed in a flow reactor at 54 hPa.

of the cooling stage was controlled by adjusting the current through a heating foil while maintaining constant cooling by supplying liquid nitrogen. The temperature sensor embedded in the cooling stage was calibrated as described below to yield T_{p}.

The particles were exposed to a controlled humidified N_2(g) flow of about 1 SLPM (standard liter per minute). The humidified N_2(g) flow was generated by passing N_2(g) through a temperature controlled water reservoir. The N_2(g) used in this study was first passed through a hydrocarbon gas trap and subsequent cold trap at 198 K filled with molecular sieve to minimize contamination by other gas phase species. The presence of a filter with pore size of 0.25 μm in diameter before the gas inlet of the INC did not have a measurable effect on the ice nucleation experiments. The water partial pressure within the humidified N_2(g) was adjusted by changing the temperature of the water reservoir and diluting the humidified flow with a second flow of dry and purified N_2(g). At the exit of the INC the dew point, T_{d}, was determined using a chilled mirror hygrometer (GE Sensing) in a range of 203–293 K with an uncertainty of ±0.15 K[39,115].

RH_{ice} and relative humidity with respect to water (RH) above the particles were calculated from monitored T_{p} and T_{d} using the following equations:

$$RH = \frac{p^{0}_{\mathrm{H_2O}}(T_{\mathrm{d}})}{p^{0}_{\mathrm{H_2O}}(T_{\mathrm{p}})}, \tag{4.1}$$

$$RH_{\mathrm{ice}} = \frac{p^{0}_{\mathrm{H_2O}}(T_{\mathrm{d}})}{p^{\mathrm{ice}}_{\mathrm{H_2O}}(T_{\mathrm{p}})}, \tag{4.2}$$

where $p^{\mathrm{ice}}_{\mathrm{H_2O}}(T_{\mathrm{p}})$ and $p^{0}_{\mathrm{H_2O}}(T_{\mathrm{p}})$ are the saturation vapor pressures over ice and water at T_{p}, respectively. $p^{0}_{\mathrm{H_2O}}(T_{\mathrm{d}})$ is the saturation vapor pressure at T_{d} representing the water partial pressure in the INC. $p^{\mathrm{ice}}_{\mathrm{H_2O}}(T_{\mathrm{p}})$, $p^{0}_{\mathrm{H_2O}}(T_{\mathrm{p}})$, and $p^{0}_{\mathrm{H_2O}}(T_{\mathrm{d}})$ were calculated using the parameterizations given by Murphy and Koop[25].

4.3.3 Experimental procedure

The particles were generated and placed onto the cooling stage within the INC and T_{p} was set to room temperature. The dew point was adjusted to about 4 K above the temperature at which ice nucleation was to be observed. The particle temperature was then decreased from room temperature to T_{d}+1 K resulting in RH_{ice}~88%. The experiment started as T_{d} was stable for at least 30 minutes. Then RH_{ice} was continuously increased by cooling T_{p} with a rate of 0.1 K min^{-1} until ice formation or water uptake was observed[3,26]. The cooling rate is relevant to rates associated with updraft speeds reported for mid- and low latitude cirrus clouds[248]. Typical experimental RH_{ice} trajectories are illustrated in Fig. 4.2A for different initial T_{p}. Each dotted line in Fig. 4.2A represents RH_{ice} trajectory for which T_{d} is constant. The change in RH_{ice} is $\sim$2.3% to 1.5% per minute for temperatures from 200 to 260 K, respectively. As T_{p} decreases by $\sim$4 K below T_{d}, RH_{ice} increases from 100% to $\sim$160% and 190% at temperatures of 260 and 200 K, respectively.

Images of the particles were recorded every 0.02 K, i.e., every 12 seconds, while simultaneously recording the experimental time, T_{d}, and T_{p}. The onset of ice nucleation or water uptake by the particles was determined by the change of the particle size and phase from the recorded images. The OM allowed us to visually identify the changes in particle size and phase due to water uptake or ice formation of larger than 0.2 and 1 μm when using a magnification of 1130x and 230x, respectively. Estimates of the water vapor flux indicated that the water vapor supply was sufficient for a detectable size change of the particles by 0.2 and 1 μm due to water uptake or ice formation on deposited particles between 6 and 36 seconds at 235 K, respectively, assuming a water vapor condensation coefficient of 0.01. At higher temperatures the time needed to establish the detectable size change is significantly faster (i.e. 5 s instead of 36 s) due to a higher water partial pressure. We report ice formation as immersion freezing if water uptake was observed prior to ice crystal formation and as deposition ice nucleation if no water uptake was observed prior to ice crystal formation. Thus, immersion freezing events which occur within $<$ 6 and 36 seconds may be misinterpreted as deposition nucleation by our system. Here we report ice nucleation onsets, i.e., T_{p} and RH_{ice} values at which the first ice crystal was observed. In some instances multiple ice crystals formed simultaneously. Then all the initially formed ice crystals were counted. Subsequent ice formation events were discarded since a uniform RH field may not persist when ice crystals are present in the INC.

After an ice nucleation experiment T_{p} was calibrated following previously applied methods[3,26,195] which is outlined below. Prior to repetition of the experiment, the particle sample was warmed up to 275 K to ensure complete sublimation of ice crystals and exclude the possibility of preactivation[246]. For blank substrates and each particle type, the experiment was repeated at least 3 times for each particle sample employing minimum 3 independent samples for each investigated T_{p}.

4.3.4 Calibration

Temperature calibration was conducted following previous methods[3,26,195]. T_{p} was calibrated against T_{d} by measuring the 2-D projected surface area

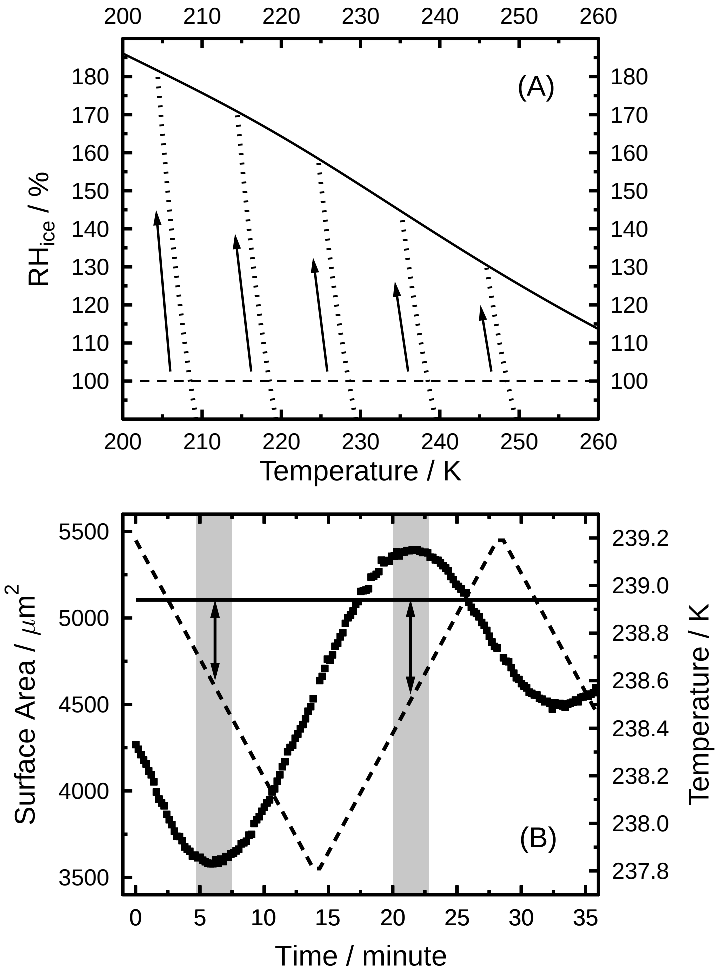

Figure 4.2: Panel A shows typical experimental RH_{ice} trajectories. The dashed and solid lines indicate ice saturation and water saturation, respectively. The dotted lines indicate RH_{ice} trajectories for which T_{d} was constant and T_{p} changed by 0.1 K min^{-1}. Panel B shows the changes in surface area and particle temperature during a calibration experiment. The dashed and black lines represent T_{p} and T_{d}, respectively. The black squares represent surface area of one ice crystal determined by OM. The gray bars indicate when the ice crystal maintained a constant surface area. The arrows indicate the deviation between T_{p} and T_{d}.

(SA) of ice crystals. At constant T_d, ice crystals grow or shrink (SA increases or decreases) when T_p is decreased or increased, respectively. A calibration experiment is shown in Fig. 4.2B. At the beginning of the calibration experiment in presence of at least one ice crystal, when T_p is higher than T_d, thus $RH_\mathrm{ice} < 100\%$, resulting in sublimation of the ice crystal and corresponding decrease in SA. Subsequently, RH_ice is increased by decreasing T_p at 0.1 K min^{-1}. When the ice crystal maintains a constant SA as indicated by the gray bar in Fig. 4.2B, $RH_\mathrm{ice} = 100\%$ indicating that the temperature of the substrate is equal to T_d. Further decrease of T_p results in growth of the ice crystal corresponding to an increase of SA. The determined difference between T_d and T_p **represents** the temperature offset for which T_p has to be calibrated. The conservative experimental uncertainties were calculated from the uncertainties of $\Delta T_\mathrm{d} < \pm 0.15$ K and $\Delta T_\mathrm{p} < \pm 0.3$ K resulting in $\Delta RH_\mathrm{ice} < \pm 11\%$ for 200 K and $\Delta RH_\mathrm{ice} < \pm 3\%$ for 260 K. Error bars presented for the data in this study indicate on standard deviation of observed RH_ice and T_p values or above discussed experimental uncertainties in RH_ice and T_p whichever is larger.

4.3.5 Ozone exposure system

Atmospheric particle O_3 exposure of ~40 ppb for two weeks was achieved using the flow system shown in Fig. 4.1B. This results in an O_3 exposure of 4.8×10^{-2} atm s which was calculated from the O_3 partial pressure (P_{O_3}) and the time particles were exposed to O_3 as $P_{O_3} \cdot t$[160,161]. To generate O_3, a N_2(g) flow and a O_2(g) flow were first passed through a hydrocarbon gas trap and subsequent cold trap at 198 K for further purification. O_3 was generated by passing the O_2(g) through an ultraviolet source operated at 254 nm (Jelight Inc.) and subsequently mixed with a dry N_2(g) flow. The O_3-containing flow was introduced into a flow reactor consisting of a 35 cm long denuder with inner diameter of 2 cm in which the particle samples or blank substrates were placed. An O_3 monitor (2B Technologies) working at atmospheric pressure was used to measure inlet gas pressure and the concentration of O_3 every 10 seconds based on the absorption of UV light by O_3 at 254 nm.

In the laboratory we mimic the atmospheric O_3 exposure by employing a higher O_3 concentration which allows us to reduce the experimental exposure time. The entire system was flushed thoroughly with ultra high purity N_2(g) before placing the samples inside the flow reactor. The particle samples were exposed to O_3 concentrations of ~85 ppm for 3 hours in the flow reactor at 54 hPa. This approach assumes that the O_3 exposure and thus the degree of particle oxidation behaves linearly with O_3 concentration. If oxidation occurs as a second order or higher reaction order, the efficiency of the heterogeneous oxidation process may change significantly with O_3 concentration and, hence, laboratory O_3 exposure may lead to a different degree of oxidation when compared to the atmospherically relevant one[166]. Volatilization of organic material due to O_3 oxidation, e. g. as observed for the reaction of O_3 with liquid oleic acid[249], cannot be ruled out. However, the primary aim of the laboratory O_3 exposure experiments of SRFA and Leonardite particles is to detect any significant effect of heterogeneous oxidation on the particles' ice nucleation efficiency which is detectable under these experimental conditions.

4.3.6 Chemicals

Kaolinite dust was purchased from Fluka. Leonardite and SRFA were purchased from International Humic Substance Society (IHSS). Millipore water (resistivity $\geq$18.2 MΩ cm) was used for humidification. O_2 (99.99%) and N_2 (99.999%) were purchased from Praxair.

4.4 Results and Discussion

4.4.1 Ice nucleation on Kaolinite particles

Validation of the novel INC was performed by determining the ice nucleation onsets of Kaolinite particles which are known to be efficient IN[3,26–29]. Before conducting the ice nucleation experiments, the quality of the hydrophobic coating and thus the effect of the substrate on ice nucleation was determined by measuring the ice nucleation onsets of particle free substrates. Figure 4.3 shows that ice nucleation or water uptake on blank substrates occurred at RH_{ice} from 121% to 168% for temperatures from 251 to 208 K. These RH_{ice} values indicate the experimental maximum achievable RH_{ice} values at corresponding temperatures for which an effect of the substrate on ice nucleation can be ruled out. In other words, ice formation observed at RH_{ice} values lower than the maximum RH_{ice} derived from blank substrates can be attributed to ice nucleation initiated by the deposited particles. The OM technique allowed visual confirmation that ice nucleation was induced by particles and not by the substrate and that at the same time no water condensed on the particle free area of the substrate. As shown in Fig. 4.3, O_3-exposed substrates show similar maximum RH_{ice} values suggesting that O_3 exposure did not significantly affect the quality of the hydrophobic coating for our experimental conditions. This finding is corroborated by a previous study of the photo-reactivity of alkylsiloxane self assembled monolayers (SAM) on SiO_2 surfaces showing that O_3 did not have a significant effect on the degradation of the monolayer[250].

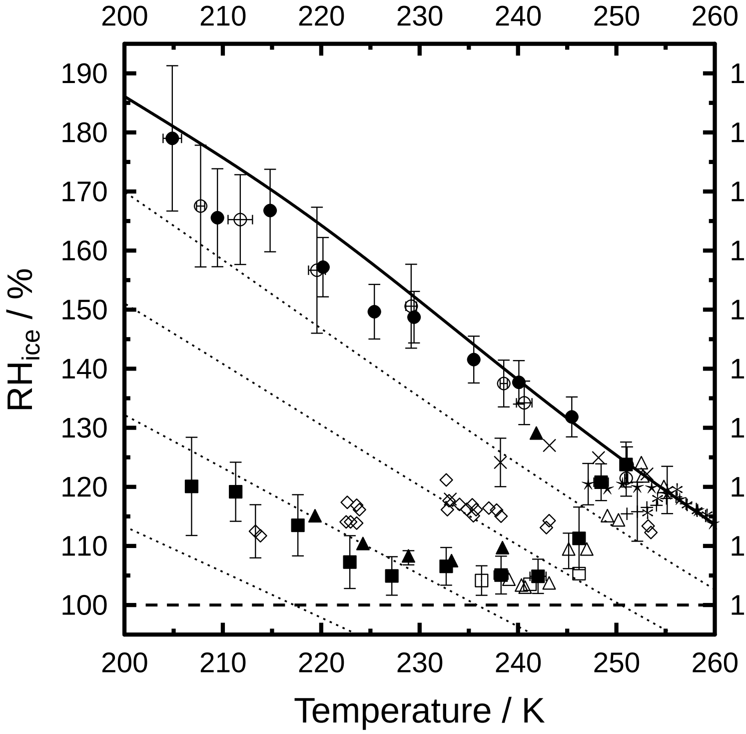

Figure 4.3: Ice nucleation onset conditions of blank substrates and Kaolinite particles are shown. The open and filled circles show the onsets for unexposed and O_3-exposed blank substrates, respectively. The filled squares represent ice nucleation onsets for Kaolinite particles. Solid and dash lines indicate water saturation and ice saturation, respectively. The diagonal dotted lines indicate 90, 80, 70, and 60% *RH* from the upper right to the bottom left[25]. Previous ice nucleation data employing Kaolinite are shown as open triangles[3], open squares[26], open diamonds[27], pluses[28], stars[29], filled triangles[30], asterisks[31] and crosses[32]. Corresponding representative error bars are given on the selected data points.

Figure 4.3 shows the ice nucleation onsets for Kaolinite particles as a function of T_p and RH_ice observed here and data from previous studies[3,26–32]. The Kaolinite particle sample characteristics are given in Table 1. Our data show that Kaolinite particles induced ice formation via deposition mode at 102–124% RH_ice for temperatures below 251 K. At 251 K some ice formation events (6 out of 9 experiments) occurred at ∼124% RH_ice which corresponds to water saturation without indication of water uptake prior to ice formation. For the remaining experiments at 251 K, water uptake was observed first and followed by immersion freezing. Dymarska et al.[3] reported water uptake by Kaolinite particles prior to ice formation at 252.5 K. Previous studies also reported the highest temperatures for deposition ice nucleation range from 251 to 254 K[27–29,31,32]. The RH_ice ice nucleation onset decreased from 124% at 251 K to ∼105% at 243–220 K similar to previous studies[3,26,30] and then increased to 120% at 207 K. Our results corroborate that Kaolinite particles are very efficient IN inducing ice nucleation as low as 102% RH_ice in agreement with previous studies[3,26–32].

4.4.2 Ice nucleation on SRFA and O_3-exposed SRFA particles

Figure 4.4A shows ice nucleation onsets and water uptake by SRFA and O_3-exposed SRFA particles as a function of T_p and RH_ice. The corresponding particle sample characteristics are summarized in Table 1. For $T_\mathrm{p} \leq 231$ K, ice nucleated on SRFA particles at mean RH_ice values of 137–148% which were well below water saturation and no water uptake was observed indicating that ice nucleation occurred via deposition mode. At 236 and 241 K, ice formation events occurred either via deposition mode or immersion freezing. Water uptake was first observed and followed by immersion freezing for 4 out of 10 experiments and 3 out of 12 experiments at 236 and 241 K, respectively. For the remaining experiments at 236 and 241 K ice nucleated on SRFA particles via deposition mode. At 246 K, all ice formation events occurred via immersion freezing in which water uptake was observed prior to ice nucleation at 98% RH. At 251 K, water uptake was first observed at 99% RH on SRFA particles but only in some cases (3 out of 9 experiments) followed by immersion freezing.

For O_3-exposed SRFA particles, all ice formation events occurred via deposition mode at $T_\mathrm{p} \leq 241$ K which is about 10 K warmer compared to SRFA particles. This implies that oxidation by O_3 enhanced the ice nucleation efficiency of the investigated SRFA particles by up to 10 K. For $T_\mathrm{p} \leq 231$ K, ice nucleation occurred on O_3-exposed SRFA particles via deposition mode at mean RH_ice values of 137–150% which is in a similar range as for SRFA

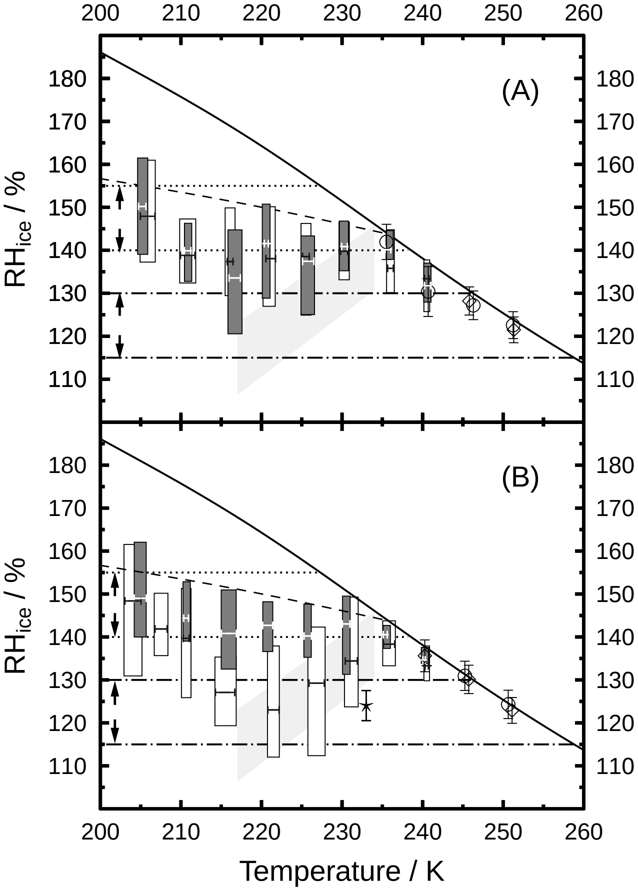

Figure 4.4: The onset conditions for ice nucleation and water uptake as a function of T_p and RH_{ice} are shown in panel A for SRFA and O_3-exposed SRFA particles and in panel B for Leonardite and O_3-exposed Leonardite particles. For both panels: The white and gray bars show the ranges of observed ice nucleation onsets with mean onset RH_{ice} indicated by the horizontal lines within the bars for deposition ice nucleation on unexposed and O_3-exposed particles, respectively. The open circles and open diamonds indicate the mean onset values of water uptake by unexposed and O_3-exposed particles, respectively. Solid line is the same as in Fig. 4.3. The dashed line represents RH_{ice} thresholds for homogeneous ice nucleation of an aqueous droplet[33]. Light gray shaded area indicates bounds of continental cirrus onset formation[16]. RH_{ice} values between horizontal paired dash-dotted and dashed lines indicated by arrows represent the lower limits for cirrus formation conditions in the northern and southern hemisphere, respectively[17]. The star in panel B represents deposition ice nucleation onset on Leonardite particles[8].

particles. At 246 K, all ice formation events occurred via immersion freezing in which water uptake by O_3-exposed SRFA particles was observed prior to ice nucleation. At 251 K, water uptake was first observed at 98% RH on O_3-exposed SRFA particles but only in some cases (3 out of 12 experiments) followed by immersion freezing.

Water uptake for SRFA and O_3-exposed SRFA particles occurred close to water saturation. This is expected since SRFA particles possess a small growth factor of 1.1 at 90% RH for 295–303 K[241,243]. Here, our data suggest that oxidation by O_3 renders SRFA particle surfaces more IN efficient and less favorable to water uptake.

4.4.3 Ice nucleation on Leonardite and O_3-exposed Leonardite particles

Figure 4.4B shows ice nucleation onsets and water uptake by Leonardite and O_3-exposed Leonardite particles as a function of T_p and RH_ice. Table 1 lists the corresponding particle sample characteristics. For both Leonardite and O_3-exposed Leonardite particles, water uptake occurred at 98% RH for $T_\mathrm{p} \geq 246$ K. At 246 K, in some cases initial water uptake was followed by ice formation via immersion freezing on both Leonardite and O_3-exposed Leonardite particle samples.

Figure 4.4B shows that RH_ice ice nucleation onsets for Leonardite particles possess a strong temperature dependence. Leonardite particles nucleated ice via deposition mode at mean RH_ice values of 123–148% for $T_\mathrm{p} \leq 241$ K. 14 additional ice nucleation experiments using 2 more independent Leonardite particle samples were conducted at 221 and 227 K to further corroborate the observed temperature dependency of the RH_ice ice nucleation onsets. We observed significant numbers of ice nucleation events that occurred as low as 112% RH_ice for T_p between 221 and 227 K.

O_3-exposed Leonardite particles nucleated ice via deposition mode at mean ice nucleation onsets of 140–149% RH_ice at $T_\mathrm{p} \leq 236$ K. At 241 K, only 40% of the ice formation events (4 out of 10 experiments) occurred via deposition mode. For the remaining experiments at 241 K, ice nucleated via immersion freezing after water uptake at 98% RH. Figure 4.4B indicates that O_3-exposed Leonardite particles nucleated ice in average 10 to 20% RH_ice higher compared to unexposed Leonardite particles for T_p between 215 and 227 K. Although RH_ice ice nucleation onsets for O_3-exposed Leonardite particles partly overlap with those for Leonardite particles, the data suggest that oxidation by O_3 decreases the IN efficiency of Leonardite particles between 215 and 227 K. Leonardite and O_3-exposed Leonardite particles can nucleate ice via different modes over a wide temperature range from 204 to 251 K at relevant atmospheric RH_{ice} values.

Few studies investigated the ice nucleation efficiency of HULIS particles[8,199]. Kanji et al.[8] reported that Leonardite particles can nucleate ice via deposition mode at 124% RH_{ice} at 233 K which is in agreement with our data within the uncertainties of both studies. It is commonly assumed that the efficiency of IN depends on active sites which can be associated with cracks, cavities, chemical and physical bonds allowing the enhanced interaction with water vapor[20]. Leonardite particles contain both hydrophobic and hydrophilic acids and SRFA particles only contain hydrophobic organic acids as stated by the International Humic Substance Society (http://www.ihss.gatech.edu). The hydrophilic component of Leonardite may facilitate the formation of hydrogen bonds with water molecules resulting in more active sites than SRFA. If hydrophilic groups affect ice nucleation, it would be expected that Leonardite induces ice nucleation at lower RH_{ice} than SFRA. Our data show that RH_{ice} ice nucleation onsets for Leonardite are lower than the ones for SFRA for T_{p} between 215 and 227 K. Thus, the presence of hydrophilic groups may contribute to the higher ice nucleation efficiency of Leonardite particles compared to SRFA particles.

For all investigated particle samples, we did not observe a significant relationship between observed ice nucleation onsets and particle size, number, and surface area. Table 1 summarizes the ranges in particle size, number, and surface area for the various samples investigated here. Table 1 indicates that particle size, number, and surface area remained within one order of magnitude. The resulting minor effect on ice nucleation onset is in part corroborated by previous studies indicating that a decrease of the particle loading by 3 orders of magnitude increases the ice nucleation onset from 102 to 115% RH_{ice} and a decrease of total particle surface area by up to three orders of magnitude resulted in an increase of the ice nucleation onset by about 10%[8,196]. Thus, potential changes in corresponding ice nucleation onsets may be well within our experimental uncertainties.

4.4.4 Effect of particle oxidation on ice nucleation

Oxidation of organic particles by atmospheric trace gases can lead to the formation of hydrophilic functional groups on the particle surface[161,162,251–253] that may change the ice nucleation efficiency of the particles. Figure 4.4A shows that oxidation by O_3 renders SRFA particles more ice nucleation efficient in deposition mode at temperatures between 236 and 241 K. Thus particle oxidation by O_3 may enhance the ice nucleation efficiency of SRFA particles by formation of hydrophilic functional groups. However, below 231 K, RH_{ice} ice nucleation onsets for deposition ice nucleation on O_3-exposed SRFA particles are similar to those for SRFA particles. This suggests that the chemical nature of the surface, such as hydrophilic groups, may not be the only determining factor for ice nucleation.

In the case of Leonardite particles, particle oxidation by O_3, however, renders the particles less ice nucleation efficient for the temperature range of 215 to 225 K as shown in Fig. 4.4B. The reason for these changes in IN efficiency is not clear. Leonardite particles can react with ozone with reactive uptake coefficients of 3.8×10^{-6} to 3.7×10^{-5}[254]. Our data suggest that oxidation of Leonardite particles by O_3 results in deactivation of active sites for a specific temperature range. If this is due to a chemical alteration of the particle surface, i.e., changes in chemical bond structures by addition of new hydrophilic sites or replacement of existing sites, or physical alteration, i.e., restructuring of cracks and cavities due to volatilization of organic material, could not be determined with our experimental method.

Only few studies have investigated the effect of oxidation of organic particles on ice nucleation efficiency[3,13,169]. Garten and Head[169] found that oxidation of wood char particles by suspending those in hydrogen peroxide may lead to higher IN efficiency.[13] showed that oxidation of soot particles by immersing particles in concentrated nitric and sulfuric acid mixture may render the soot particle more IN active. Dymarska et al.[3] indicated that oxidation of soot by gas-phase O_3 did not have a significant effect on the heterogeneous IN efficiency of soot particles at temperatures above 240 K. The data presented here show that O_3 oxidation can have different impacts on the ice nucleation efficiency of SRFA and Leonardite particles. Our data suggest that there is not a clear relationship between particle hydrophilicity and ice nucleation efficiency, and thus other factors may also govern the nucleation process.

4.4.5 IN activated fraction and heterogeneous ice nucleation rate coefficient

Here we report ice nucleation onsets at which the initially formed ice crystals were observed. The OM technique is sensitive to each individual ice nucleation event. Thus, the IN activated fraction is mainly defined by the number of deposited particles. Table 1 gives the range of derived IN activated fractions for the particles samples employed in this study. The IN activated fractions range from 0.008% to 0.3%. Kaolinite as the most efficient IN investigated in this study exhibits the highest IN activated fraction.

The experimental ice nucleation data obtained here were employed to derive heterogeneous ice nucleation rate coefficients (J_{het}) which are defined as the number of nucleation events per area of ice nucleus and time (cm^{-2} s^{-1}). The analysis of the experimental data has been described in detail previously[197,213]. Here we briefly introduce the data analysis. For a given temperature interval (ΔT), different numbers of ice nucleation events may occur. J_{het} as a function of temperature was derived using the following formula

$$J_{\mathrm{het}}\left(T^{i}\right) = \frac{n_{\mathrm{f}}^{i}}{t_{\mathrm{tot}}^{i} \cdot S^{i}}, \tag{4.3}$$

where $J_{\mathrm{het}}\left(T^{i}\right)$ is the average heterogeneous ice nucleation rate coefficient at the mean freezing temperature of ice nucleation events (T^{i}) within the ith temperature interval, n_{f}^{i} is the number of observed ice nucleation events and t_{tot}^{i} is the total observation time in the ith temperature interval, and S^{i} accounts for the particle surface area available for the ice nucleation within the ith temperature interval. The product $t_{\mathrm{tot}}^{i} \cdot S^{i}$ for the ith temperature interval is given by the sum of the contributions from the samples which remain unfrozen and samples that nucleate ice[197] according to

$$t_{\mathrm{tot}}^{i} \cdot S^{i} = \sum_{j=1}^{n_{\mathrm{f}}^{i}} \left(\frac{T_{\mathrm{st}}^{i} - T_{\mathrm{f},j}^{i}}{c_{\mathrm{r}}}\right) S_{j}^{i} + \frac{\Delta T}{c_{\mathrm{r}}} S_{\mathrm{uf}}^{i}, \tag{4.4}$$

where T_{st}^{i} is the start temperature of the ith temperature interval, $T_{\mathrm{f},j}^{i}$ is the freezing temperature and S_{j}^{i} is the particle surface area available for the jth nucleation event occurring within the ith temperature interval, c_{r} is the cooling rate applied in the experiments, and S_{uf}^{i} is the total particle surface area that remain unfrozen until the end of the ith temperature interval. In this study, ΔT of 0.02 K was chosen corresponding to the temperature interval between two sequentially recorded images which allow to discriminate nucleation events. Surface areas were estimated from the number and sizes of the particles deposited on the substrate using OM and assuming the particles have spherical geometry. The particles most likely exhibit non-ideal geometry including cracks, cavities, or intrusions. Thus, our assumption will result in an underestimation of the actual particle surface area and yield an upper limit of J_{het}.

Figure 4.5 presents the derived J_{het} values for deposition ice nucleation for the different particle types studied here as a function of temperature. For all investigated particle types J_{het} is a strong function of temperature as expected from classical nucleation theory (CNT)[20]. Figure 4.5A shows that J_{het} for SRFA particles increases by two to three orders of magnitude within 2 K for the investigated particle temperatures. For example, J_{het} increases from 12

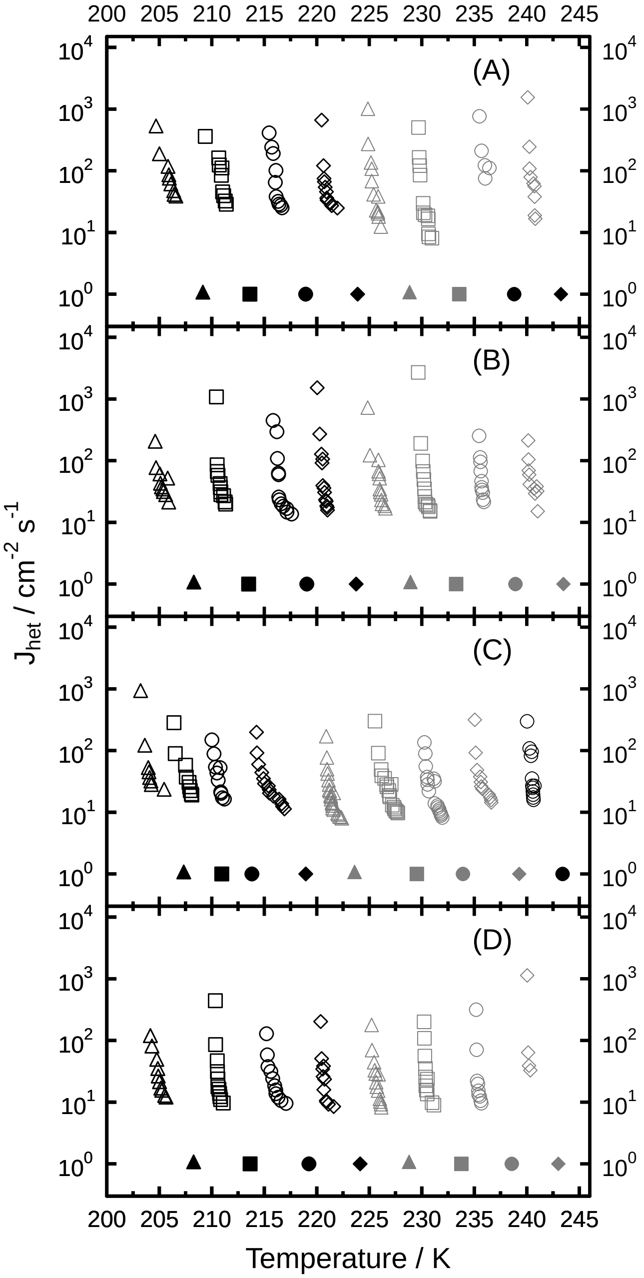

Figure 4.5: Experimentally derived J_{het} values as a function of temperature for deposition ice nucleation are shown for SRFA (A), O_3-exposed SRFA (B), Leonardite (C), and O_3-exposed Leonardite (D) particles. Each open symbol type in corresponding gray level represents ice nucleation experiments conducted at same T_{d}. Filled symbols represent corresponding temperatures at which $RH_{\mathrm{ice}} = 100\%$.

cm^{-2} s^{-1} to 940 cm^{-2} s^{-1} within 1.2 K from 226.1 K to 224.9 K. Figure 4.5B presents J_{het} for O$_3$-exposed SRFA particles. The corresponding maximum of J_{het} ranges from 190 to 2700 cm^{-2} s^{-1} for the observed temperatures. For T_{p} below 231 K O$_3$-exposed SRFA particles exhibit similar J_{het} values as for SRFA particles. As shown in Figs. 4.5C and D, maximum J_{het} values for Leonardite and O$_3$-exposed Leonardite particles range from 140 to 870 cm^{-2} s^{-1} and from 110 to 1130 cm^{-2} s^{-1}, respectively, for the observed temperatures.

4.4.6 Contact angle

CNT can be employed to describe heterogeneous nucleation in atmospheric cloud models[255,256] and to analyze laboratory data[26,35,106]. A key parameter in determining IN efficiency is the contact angle (θ). θ for an ice embryo formed on an IN characterizes the relationship of surface free energies among the three involved interfaces including water vapor, ice embryo, and IN. Here, we calculated θ from the experimentally derived J_{het} for the different particle types employed in this study following previous methods[26,35]. J_{het} is defined as

$$J_{\mathrm{het}} = A \cdot exp(\frac{-\Delta F_{\mathrm{g,het}}}{kT}), \tag{4.5}$$

where A is a pre-exponential factor, $\Delta F_{\mathrm{g,het}}$ is the free energy of formation of the ice germ, k is the Boltzmann constant, and T is the temperature. Assuming that an ice embryo on a curved solid substrate can be described as a spherical cap, the free energy of ice embryo formation is given by[20]

$$\Delta F_{\mathrm{g,het}} = \frac{16\pi M_{\mathrm{w}}^2 \sigma_{\mathrm{i/v}}^3}{3[RT\rho ln S_{\mathrm{ice}}]^2} \cdot f(m,x), \tag{4.6}$$

where M_{w} is the molecular weight of water, $\sigma_{\mathrm{i/v}}$ is the surface tension at the ice-vapor interface, R is the universal gas constant, ρ is the density of ice, S_{ice} is the saturation ratio with respect to a planar ice surface, $f(m,x)$ is the geometric factor, and x is the ratio of the radius of the substrate to the radius of spherical ice germ. m is the compatibility parameter. θ usually is defined by the compatibility parameter, $m = \cos(\theta)$[105]. Assuming the radius of the particle substrate is much larger than the radius of the ice germ which is a good approximation for aerosol particles, then $f(m,x)$ is defined, without considering curvature adjustment which is negligible for aerosol sizes > 0.1 μm[20,106], as follows

$$f(m) = \frac{m^3 - 3m + 2}{4}. \tag{4.7}$$

To calculate θ, the free energy of ice germ nucleation was calculated from experimentally derived J_{het} assuming A = 10^{25} cm^{-2} s^{-1} [20,26,35]. Then, θ was calculated using Eqns. 4.6 and 4.7 with $M_{\text{w}} = 18.015$ g mol^{-1}, $\rho = 0.92$ g cm^{-3}, and $\sigma_{\text{i/v}} = 106$ mJ m^{-2} [20,26,35].

The derived θ allows for comparing the IN efficiencies of different particle types. Particles with smaller θ values are more efficient IN. Figure 4.6A shows θ as a function of temperature for all particle types employed in this study. Here, the uncertainty in θ is mostly affected by the uncertainty in RH_{ice} and only to a lesser extent by J_{het}. For example, increasing J_{het} by one order of magnitude, leaving all other parameters the same, changes θ by ~0.3°. SRFA, O_3-exposed SRFA, and O_3-exposed Leonardite particles possess θ values of ~27°. Leonardite particles exhibit a wider range of θ from 20.9 to 27.5° and thus can serve as more efficient IN at temperatures from 215 to 227 K as indicated in Fig. 4.4B. θ for Kaolinite particles ranges from 10.1 to 21.7° at the observed temperatures in agreement with previously determined θ [26,30] as shown in Fig. 4.6A. Overall the organic particles studied here exhibit larger θ values and thus are less efficient IN than Kaolinite particles at temperature between 200 to 250 K.

Figure 4.6B shows θ as a function of RH_{ice} for the particles employed in this study and previous deposition ice nucleation data for Kaolinite, Arizona Test Dust, Muscovite, Montmorillonite, Quartz, Calcite, Saharan dust, dust collected in Spain, Fe_2O_3, MgO, and SiO_2 particles[26,30,34–36]. θ derived here and in previous studies Eastwood et al.[26], Kulkarni and Dobbie[34], Kanji and Abbatt[35] show a very similar trend with RH_{ice} ice nucleation onsets and can be very well represented by

$$\theta = a + b \cdot ln(RH_{\text{ice}} + c), \tag{4.8}$$

where a = -13.428, b =10.4731, $c = -95.785$, and RH_{ice} between 100% and 160%. The correlation coefficient, R^2, for this fit yields 0.98. It is remarkable that these different particle types which nucleate ice for a wide range of temperature and RH_{ice} onsets show a similar behavior with respect to RH_{ice} when expressed as θ. However, θ derived by Welti et al.[30], and Saunders et al.[36] deviate significantly from the other laboratory derived contact angles. The reason for this could lie in the different experimental techniques and methods to derive J_{het} and RH_{ice} necessary to calculate θ.

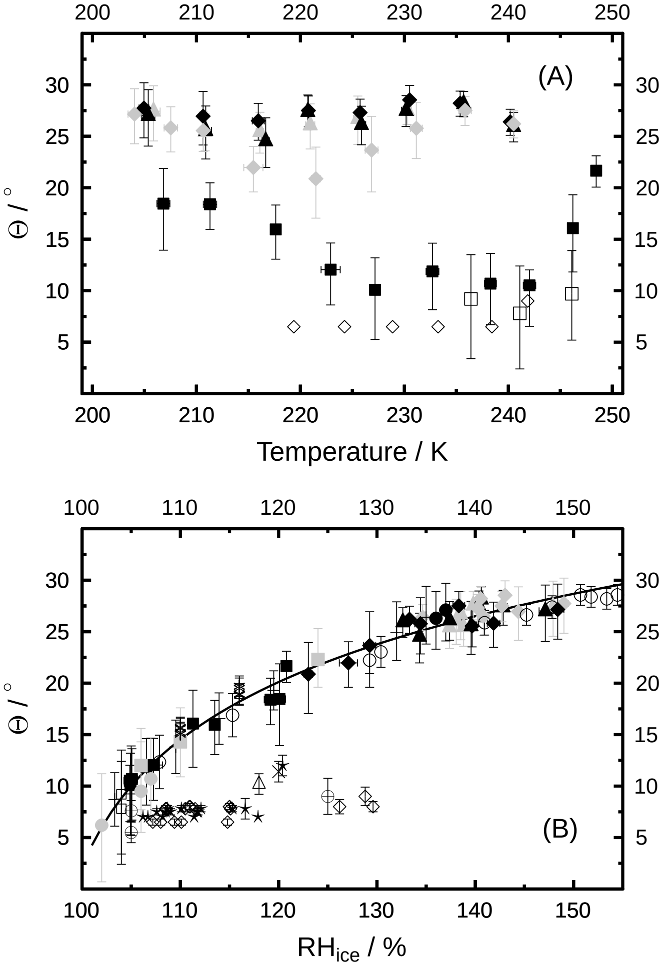

Figure 4.6: Panel A shows the contact angle (θ) as a function of temperature for Kaolinite (filled squares), Leonardite (gray diamonds), O_3-exposed Leonardite (black diamonds), SRFA (gray triangles), O_3-exposed SRFA (black triangles). θ data for Kaolinite from previous studies by Eastwood et al.[26] and Welti et al.[30] are shown as open squares and open diamonds, respectively. Panel B shows θ as a function of RH_{ice} for Kaolinite (filled squares), Leonardite (gray diamonds), O_3-exposed Leonardite (black diamonds), SRFA (gray triangles), and O_3-exposed SRFA (black triangles) derived in this study, and Calcite (pluses), Muscovite (gray filled circles), Montmorillonite (ray filled squares), Kaolinite (open squares), and Quartz (black filled circles)[26], montmorillonite (stars) and Kaolinite (open diamonds)[30], Saharan dust and dust collected in Spain (asterisks)[34], Arizona Test Dust (open circles)[35], and Fe_2O_3 (circles with pluses), MgO (crosses), and SiO_2 (open triangles)[36]. Thin black line represents a logarithmic fit according to Eqn. 4.8.

4.5 Atmospheric implication

Field measurements have shown that organic material can contribute a significant mass fraction to atmospheric aerosol particles[1]. Here we showed that SRFA, Leonardite, and corresponding O_3-exposed particles can serve as IN for a wide range of temperatures and RH_{ice}. The observed onset conditions for cirrus cloud formation by Ström et al.[17] and Haag et al.[18] during the INCA (Interhemispheric differences in cirrus properties from anthropogenic emissions) field study and by Heymsfield and Miloshevich[16] for continental cirrus are shown in Fig. 4.4. Haag et al.[18] reported ice formation in the southern hemisphere (SH) was initiated predominantly by homogeneous nucleation and in the northern hemisphere (NH) by homogeneous and selective heterogeneous nucleation. Heymsfield and Miloshevich[16] derived bounds for the ice nucleation onset of cirrus clouds using field observations of quasi-steady-state orographic clouds and cirrus clouds. In addition, Fig. 4.4. shows RH_{ice} thresholds for homogeneous ice nucleation of an aqueous droplet with 2.5 μm in diameter corresponding to a homogeneous ice nucleation rate coefficient of $\sim 4\times 10^{10}$ cm^{-3} s^{-1}[33].

Figure 4.4 shows that the RH_{ice} ice nucleation onsets of SRFA and O_3-exposed SRFA particles via deposition mode are lower than those for homogeneous ice nucleation at $T_{\mathrm{p}} < 235$ K and are close to the lower bound of cirrus cloud onset conditions observed in the SH[17,18] suggesting that SRFA and O_3-exposed SRFA particles may act as IN under these conditions. Leonardite particles form ice at much lower RH_{ice} onsets compared to homogeneous ice nucleation. The observed RH_{ice} onsets of Leonardite particles coincide in part with the observed cirrus cloud onset conditions in the NH[17,18] and continental cirrus cloud formation[16]. However, O_3-exposed Leonardite particles show ice nucleation onsets closer to the cirrus cloud onset conditions in the SH[17]. The data presented here indicate that SRFA, O_3-exposed SRFA, Leonardite, and O_3-exposed Leonardite particles can initiate ice formation via heterogeneous ice nucleation under atmospheric conditions typically observed for cirrus formation.

Initial water uptake and subsequent immersion freezing of SRFA, Leonardite, and corresponding O_3-exposed particles at temperatures ≥ 236 K indicate that these particles can initiate ice formation relevant for the formation of mixed-phase clouds[70,233]. Overall, ice nucleation data presented here suggest that HULIS-containing atmospheric particles have the potential to play a role in both cirrus and mixed-phase cloud formation irrespective of the degree of oxidation by O_3.

The parameterization of Θ with RH_{ice} allows estimation of J_{het} and ice crystal production rates ($P_{\mathrm{ice}}^{\mathrm{het}}$) when the cloud onset formation conditions are known. For this analysis, we assume Θ to be independent of temperature in the temperature range for cloud activation. This is justified first by the experimental findings that Θ does not change significantly within 10 K. Secondly, typical ice supersaturations for initiation of ice nucleation are achieved within a decrease of about 4 K in the temperature of the IN compared to the dew point of the surrounding environment[25,33]. For a particular ice nucleation onset the corresponding θ value can be read off Fig. 4.6B and using Eqns. 4.3, 4.6, and 4.7, J_{het} can be readily derived. If the available aerosol surface area per volume of air, A_p, is known, then $P_{\mathrm{ice}}^{\mathrm{het}} = A_p \cdot J_{het}$ in units of ice particles cm^{-3}(air) s^{-1}. The final maximum ice crystal concentrations are also constrained by the available water vapor and possible mass transfer due to the Wegener-Begeron-Findeisen process[77–79]. The proposed parameterization of θ, valid for a wide range of insoluble particles nucleating ice via deposition mode, and corresponding J_{het} derived as a function of T and RH_{ice} can be useful in applications such as cloud resolved modeling studies but also for post analysis of field observations to describe the evolution of the ice phase.

4.6 Summary

The heterogeneous ice nucleation efficiency of laboratory generated Kaolinite, Leonardite, and SRFA particles was investigated as a function of temperature, relative humidity, nucleation mode, and O_3 exposure. Ice nucleation and water uptake were studied using a novel ice nucleation apparatus which allows control of particle temperature as low as 203 K and relative humidity up to water saturation. Validation of the new experimental setup was performed by determining the IN efficiency of Kaolinite particles. The results corroborate that Kaolinite particles are very efficient IN inducing ice nucleation via deposition mode at 102–124% RH_{ice} for temperatures between 207 and 251 K in agreement with previous studies.

SRFA particles nucleated ice via deposition mode at 125–161% RH_{ice} for temperatures $\leq$ 230 K. At 236 and 241 K, ice formation occurred either via deposition mode or immersion freezing. At temperatures $\geq$ 246 K water uptake was first observed and followed by immersion freezing. The observed RH_{ice} ice nucleation onsets of SRFA particles are lower than those for homogeneous ice nucleation of aqueous droplets for temperatures below 231 K[33] and close to the observed lower bound of cirrus cloud onset conditions typical for the southern hemisphere[17,18]. Leonardite particles nucleated ice via deposition mode at 112–162% RH_{ice} for temperatures $\leq$ 241 K and at higher temperatures water uptake and in some cases subsequent immersion freezing was observed. The observed RH_{ice} ice nucleation onsets of Leonardite particles coincide in part with the cirrus onset conditions observed in the northern hemisphere[17,18] and continental cirrus cloud formation[16].

O_3-exposed SRFA particles nucleated ice via deposition mode at temperatures $\leq$ 241 K indicating that oxidation by O_3 can enhance the ice nucleation efficiency. But at temperatures $\leq$ 231 K ice nucleation occurred on O_3-exposed SRFA particles at similar RH_{ice} ice nucleation onsets as for SRFA particles. O_3-exposed Leonardite particles nucleated ice via deposition mode at 131–162% RH_{ice} for temperatures $\leq$ 236 K. At 241 K, ice formation occurred either via deposition mode or immersion freezing on O_3-exposed Leonardite particles and at higher temperatures water uptake and in some cases subsequent immersion freezing were observed. O_3-exposed Leonardite particles nucleated ice in average 10–20% RH_{ice} higher compared to unexposed particles for temperatures between 215 and 227 K suggesting that oxidation by O_3 renders Leonardite particles less efficient IN in this temperature range. These results indicate that particle oxidation by O_3 may have different impacts on the ice nucleation efficiency of the organic particles studied here. More ice nucleation studies taking into account particle oxidation by atmospheric trace gases are needed to assess its importance on the ice nucleation efficiency of organic particles.

We have shown that SRFA, Leonardite, and corresponding O_3-exposed particles can nucleate ice via deposition mode at atmospheric conditions typical for cirrus cloud formation. Immersion freezing induced by SRFA, Leonardite and corresponding O_3-exposed particles at temperatures $>$ 236 K indicates that these organic particles can induce ice formation at atmospheric conditions relevant for mixed-phase clouds. Our results suggest that HULIS-containing particles can play important roles in both cirrus and mixed-phase cloud formation processes.

Experimentally derived heterogeneous ice nucleation rate coefficients were applied to calculate contact angles using classical nucleation theory. The contact angles determined here and from previous studies representing various types of IN demonstrate a very similar behavior as a function of RH_{ice} onsets. A parameterization of contact angle as a function of RH_{ice} onsets was derived which allows determination of the corresponding heterogeneous ice nucleation rate coefficients assuming that the contact angle does not change within the temperature range of cloud activation. This yields, if onset conditions for cloud formation are known, ice crystal production rates and corresponding ice crystal number concentrations for deposition ice nucleation. The proposed deposition ice nucleation parameterization can provide a valuable tool for post analysis of observed atmospheric ice crystal formation for a wide range of different IN and for application in cloud resolving modeling studies.

Here ends the publication:

Heterogeneous ice nucleation on particles composed of humic-like substances impacted by O_3

Bingbing Wang and Daniel A. Knopf*

Institute for Terrestrial and Planetary Atmospheres, School of Marine and Atmospheric Sciences, Stony Brook University, Stony Brook, NY 11794, USA.

* To whom correspondence should be addressed. Email:Daniel.Knopf@stonybrook.edu

Published in Journal of Geophysical Research, Vol. 116, D03205, 2011.

4.7 J_{het} Values for Kaolinite and K Values for HULIS Surrogates and Kaolinite

Cumulative IN spectra, K, in units of cm^{-2}, were derived from the ice nucleation experimental data for the investigated kaolinite and SRFA, and Leonardite, and corresponding O_3-exposed particles serving as surrogates of HULIS typically found in atmospheric particles. $K(T)$ is derived representing the number of ice active sites on the particle surface which have nucleated ice between temperature, T, and the temperature which corresponds to RH_{ice} =100%.

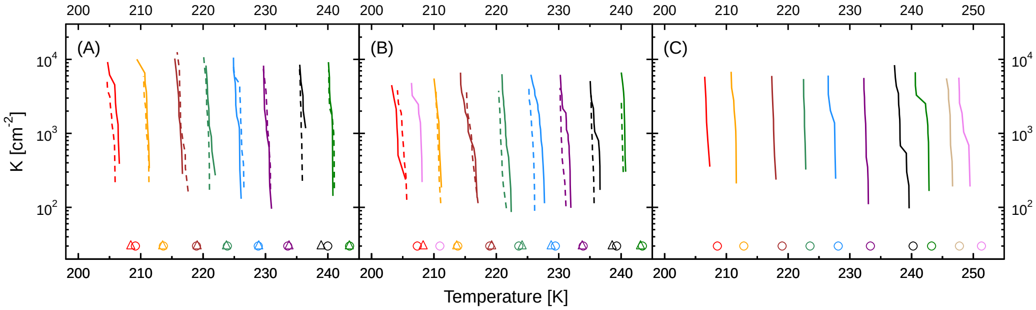

Figure 4.7: Experimentally derived cumulative ice nuclei spectra, $K(T)$, for deposition ice nucleation as a function of temperature for (A) SRFA (solid lines) and O_3-exposed SRFA (dashed lines) particles, (B) Leonardite (solid lines) and O_3-exposed Leonardite (dashed lines) particles, and (C) kaolinite particles. Individual color represents the ice nucleation experiments conducted from the same starting temperature at which RH_{ice} = 100%. The open circle and triangles represent starting temperatures for unexposed and exposed particles, respectively.

The experimentally obtained deposition ice nucleation onsets shown in Figs. 4.3 and 4.4 and the particle surfaces shown in Table 4.1 are used to derive $K(T)$ values according to Eqns. 2.29 and 2.30. ΔT of 0.02 K is applied corresponding to the temperature difference between two sequentially recorded images. $K(T)$ values for the investigated particles are presented in Fig. 4.7. $K(T)$ exhibits a strong temperature dependence for all investigated samples similar to J_{het} shown in Fig. 4.5. Decreasing the particle temperature results in more active sites being activated and thus the density of ice active site increases. For example, $K(T)$ for SRFA particles shown in Fig. 4.7A increases by about 2 orders of magnitude from ~100 to about 10000 cm^{-2} within ~3 K. As shown in Fig. 4.7B, the maximum K values of Leonardite particles are higher than those of the O_3-exposed Leonardite particles at temperatures between 215 and 230 K. This most likely is due to a higher ice nucleation efficiency of Leonardite particles at this temperature range. The $K(T)$ derived for kaolinite particles are very similar to those of SRFA and Leonardite particles, although kaolinite particles are more efficient deposition IN.

The experimental ice nucleation data were used to derived J_{het} for kaolinite particles using the same method as for HULIS surrogates as described above. Figure 4.8 presents the experimentally derived J_{het} values for deposition ice nucleation from kaolinite particles as a function of temperature. J_{het} is a strong function of temperature as expected from CNT[20]. The strong temperature dependency of J_{het} for kaolinite particles is similar to that for HULIS surrogates as shown in Fig. 4.5. J_{het} increases for kaolinite particles by two orders of magnitude within 2 K for the investigated particle temperatures. For example, for particle temperatures of ~250 K, J_{het} increases from 17 cm^{-2} s^{-1} to 995 cm^{-2} s^{-1}.

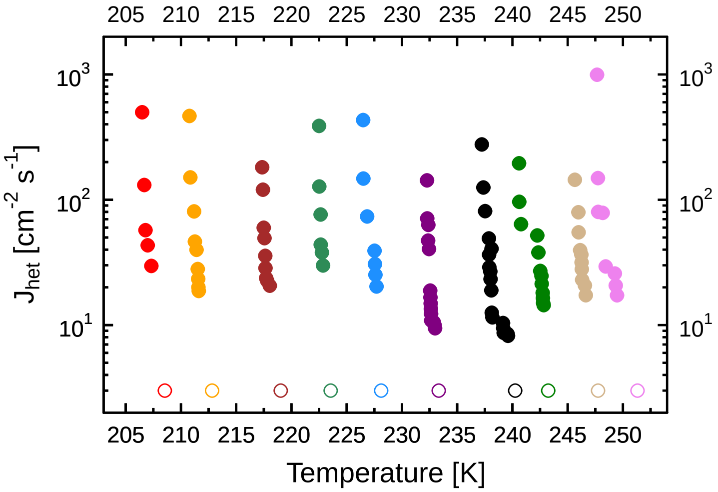

Figure 4.8: Experimentally derived J_{het} values as a function of temperature for deposition ice nucleation from kaolinite particles. Individual colors represent the ice nucleation experiments conducted of the same starting temperature for which $RH_{\mathrm{ice}} = 100\%$. The open circles represent starting temperatures.

4.8 Application of Contact Angle Parameterization and Ice Production Rates

As discussed in section 4.5, the proposed parameterization of θ can be useful in applications such as cloud resolved modeling studies but also for post analysis of field observations to describe the evolution of the ice phase. Here we give examples for the application of this parameterization.

Assuming two types of IN which nucleate ice at 110% and 140% RH_{ice}, according to the parameterization of θ, the corresponding θ for these two types of IN is 14.6° and 26.4°, respectively. The determined θ in turn yields J_{het} for different temperatures using Eqns. 4.3, 4.6, and 4.7. Figure 4.9A presents J_{het} values as a function of T and RH_{ice} for these two types of IN. For this example we assume that θ is constant with temperature, i.e., the active site inducing deposition ice nucleation does not change with temperature which is a valid assumption for solid particles. Parameterized J_{het} reflects expected behaviors such as: i) lower θ yields higher J_{het} at lower RH_{ice} values and ii) J_{het} increases with increasing RH_{ice} at constant temperature. Thus, if ice nucleation RH_{ice} and T onsets are known the corresponding J_{het} values, covering conditions before and after cloud formation, can be derived. This parameterization can also be applied to yield deposition ice nucleation rates for variable IN efficiencies, and thus ice crystal production rates, as a function of T and RH_{ice} for employment in cloud resolving models.

Ström et al.[17] reported that cirrus cloud formation in the NH was observed at minimum 115% RH_{ice} at mean observed temperatures of ∼225 K. According to Eqn. 4.8, this yields a θ value of 17.7°. Figure 4.9B shows J_{het} values as a function of RH_{ice} for T from 245 to 205 K and $\theta = 17.7°$. To represent the cirrus cloud formation process, we assume a particle trajectory in which T decreases from 226.3 to 223.8 K with a lapse rate of 8.2 K km^{-1} leading to a corresponding increase in RH_{ice} from 100% to 130%. For selected T and RH_{ice}, the corresponding J_{het} values are shown in Fig. 4.9B as filled circles and are summarized in Table 4.2.

From the aerosol size distribution observed in the NH during the INCA study (Table 1 in Kärcher and Ström[248]), the particle surface area concentration (A_p) of ∼2.5 μm^2 cm^{-3} can be derived assuming the particles are spherical. Ice crystal production rates ($P_{\mathrm{ice}}^{\mathrm{het}}$) are calculated from $P_{\mathrm{ice}}^{\mathrm{het}} = A_p \cdot J_{het}$. Derived J_{het} and $P_{\mathrm{ice}}^{\mathrm{het}}$ values along the particle trajectory are given in Table 4.2. At 224.8 K and 118% RH_{ice}, $P_{\mathrm{ice}}^{\mathrm{het}}$ is 6.8×10^{-2} cm^{-3}(air) s^{-1} yielding the formation of 4080 ice crystals per liter of air in one minute. In other words, in one minute an ice crystal concentration of ∼4.1 cm^{-3} is reached which is comparable to the observed mean concentration of ∼5.3 cm^{-3}[248]. The final ice crystal

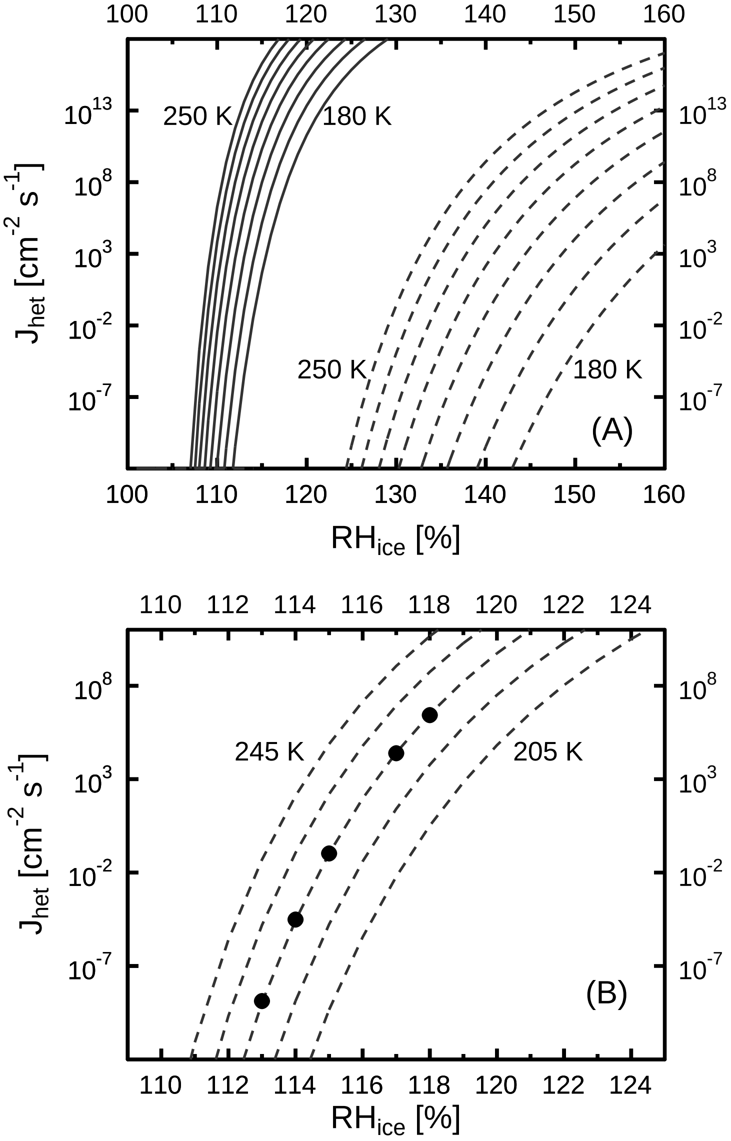

Figure 4.9: Panel A shows J_{het} values as a function of RH_{ice} for constant T ranging from 250 to 180 K given in 10 K steps for IN with θ of 14.6° and 26.4° as solid and dashed lines, respectively. Panel B shows J_{het} values as a function of RH_{ice} for constant T ranging from 245 to 205 K given in 10 K steps for IN with $\theta = 17.7°$. The filled circles indicate J_{het} values at selected T and RH_{ice} given in Table 4.3 along a particle trajectory assuming a lapse rate of 8.2 K km^{-1}.

Table 4.2: Derived heterogeneous ice nucleation rate coefficients (J_{het}) and ice crystal production rates ($P_{\mathrm{ice}}^{\mathrm{het}}$) representative of cirrus cloud formation conditions observed in the northern hemisphere during the INCA study[17,18]. J_{het} and $P_{\mathrm{ice}}^{\mathrm{het}}$ are given at selected T and RH_{ice} values indicated by filled circles in Fig. 4.9B. See text for more details.

Temperature K	RH_{ice} %	J_{het} $\mathrm{cm^{-2}s^{-1}}$	$P_{\mathrm{ice}}^{\mathrm{het}}$ $\mathrm{cm^{-3}(air)\ s^{-1}}$
225.2	113	1.3×10^{-9}	3.3×10^{-16}
225.1	114	3.1×10^{-5}	7.8×10^{-13}
225.0	115	1.1×10^{-1}	2.8×10^{-9}
224.9	117	2.4×10^{4}	6.0×10^{-4}
224.8	118	2.7×10^{6}	6.8×10^{-2}

numbers depend on the available IN concentration and water vapor. Table 4.2 also indicates that our parameterization captures the rapid increase in J_{het} and $P_{\mathrm{ice}}^{\mathrm{het}}$ for small changes in T and RH_{ice} emphasizing the high sensitivity of heterogeneous ice nucleation on the environmental parameters.

Field studies have shown that biomass burning is a significant source of HULIS[143–146,257] and that biomass burning plumes can reach the upper troposphere where temperatures favor ice nucleation[151,231,232,258]. Particle number densities of ∼140 $\mathrm{cm^{-3}}$ and particle diameters of 90–2000 nm were observed in biomass burning plumes[231,232] which are similar to the particle number densities and sizes observed in the SH during the INCA study[17]. As discussed above, HULIS type particles may nucleate ice via heterogeneous nucleation at similar thresholds with respect to T and RH_{ice} as cirrus clouds in the SH as shown in Fig. 4.4[17]. Cirrus cloud formation in the SH was identified to occur via homogeneous ice nucleation at ∼140% RH_{ice} at mean observed temperatures of ∼225 K[17,18].

Here we compare ice crystal production rates from heterogeneous ice nucleation on solid HULIS type particles ($P_{\mathrm{ice}}^{\mathrm{het}}$) and from homogeneous ice nucleation on aqueous droplets ($P_{\mathrm{ice}}^{\mathrm{hom}}$) assuming both types of particles nucleate ice at 140% RH_{ice} and 225 K. Under these conditions $\theta = 26.4°$ according to Eqn. 4.8. We employed the aerosol size distribution observed in the SH (Table 1 in Kärcher and Ström[248]) and assumed spherical particles to derive $A_p = 2$ $\mu\mathrm{m^{-2}\ cm^{-3}}$ and particle volume concentration (V_p) of 0.9 $\mu\mathrm{m^{-3}\ cm^{-3}}$. Again, we assume a particle trajectory in which T decreases from 226.5 to 224 K with a lapse rate of 8.2 K $\mathrm{km^{-1}}$ leading to an corresponding increase in RH_{ice} from 120% to 155%. At 224.9 K and 141% RH_{ice} J_{het} is 3.1×10^{4} $\mathrm{cm^{-2}\ s^{-1}}$ resulting in $P_{\mathrm{ice}}^{\mathrm{het}} = 6.2\times10^{-4}\ \mathrm{s^{-1}\ cm^{-3}(air)\ s^{-1}} = 37\ \mathrm{L^{-1}(air)\ min^{-1}}$. The water activity based ice nucleation theory[33] was employed to derive the corresponding homogeneous ice nucleation coefficient, J_{hom}. $P_{\mathrm{ice}}^{\mathrm{hom}}$ is calculated from $P_{\mathrm{ice}}^{\mathrm{hom}} = V_p \cdot J_{hom}$. This yields $J_{hom} = 5.8\times10^{-3}$ cm^{-3} s^{-1} resulting in $P_{\mathrm{ice}}^{\mathrm{hom}} = 5.2\times10^{-15}$ cm^{-3}(air) s^{-1} = 3.1×10^{-10} L^{-1}(air) min^{-1} under the same conditions.

Table 4.3: Heterogeneous (J_{het}) and homogeneous ice nucleation rate coefficients (J_{hom}) with corresponding heterogeneous ($P_{\mathrm{ice}}^{\mathrm{het}}$) and homogeneous ice crystal production rates ($P_{\mathrm{ice}}^{\mathrm{hom}}$) derived for cirrus cloud formation onset conditions observed in the southern hemisphere during the INCA study[17,18]. See text for more details.

Temperature K	RH_{ice} %	J_{het} cm^{-2}s^{-1}	$P_{\mathrm{ice}}^{\mathrm{het}}$ cm^{-3}(air) s^{-1}	J_{hom} cm^{-3}s^{-1}	$P_{\mathrm{ice}}^{\mathrm{hom}}$ cm^{-3}(air) s^{-1}
224.9	141	3.1×10^{4}	6.2×10^{-4}	5.8×10^{-3}	5.2×10^{-15}
224.8	143	1.1×10^{6}	2.2×10^{-2}	62	5.6×10^{-11}
224.6	146	1.1×10^{8}	2.2	9.4×10^{6}	8.5×10^{-6}
224.3	151	4.3×10^{10}	860	1.2×10^{14}	110

Clearly, under the observed cirrus cloud onset conditions, heterogeneous ice nucleation is the dominant process leading to initial ice crystal formation. As shown in Table 4.3, at 224.8 K and 143% RH_{ice}, $P_{\mathrm{ice}}^{\mathrm{het}}$ yields 2.2×10^{-2} cm^{-3}(air) s^{-1} resulting in the formation of ~1300 ice crystals per liter of air in one minute. In one minute, an ice crystal concentration of ~1.3 cm^{-3} can form under these conditions which is comparable to the mean ice crystal concentration of 1.2 cm^{-3} observed in the SH[248]. As indicated in Table 4.3, if RH_{ice} increases to 146%, $P_{\mathrm{ice}}^{\mathrm{het}}$ is still several orders of magnitude higher than the corresponding $P_{\mathrm{ice}}^{\mathrm{hom}}$. Although the maximum ice crystal concentrations are limited by the available water vapor and possible mass transfer due to the Wegener-Begeron-Findeisen process[77–79], heterogeneous ice nucleation and not homogeneous ice nucleation may be the dominant ice nucleation mechanism to account for these high ice crystal concentrations. These calculations indicate that heterogeneous ice nucleation on HULIS type particles can be important for atmospheric ice cloud formation processes even at ambient conditions close to the onset of homogeneous ice nucleation.

These examples show that the proposed parameterization of θ and corresponding J_{het} derived as a function of T and RH_{ice} can be useful in applications such as cloud resolved modeling studies but also for post analysis of field observations to describe the evolution of the ice phase.

Chapter 5

Heterogeneous Ice Nucleation by Field–Collected Particles

This chapter presents the investigation of heterogeneous ice nucleation and water uptake from different types of anthropogenic and marine impacted particles collected during the MILAGRO and CalNex field campaigns. The chemical composition of the investigated particles is determined by CCSEM/EDX and STXM/NEXAFS. The effect of chemical composition on the particles' ice nucleation efficiency and water uptake are discussed. The ice nucleation efficiencies of field-collected and laboratory-generated particles are compared. Experimentally obtained deposition ice nucleation onsets are used to derive J_{het}, $K(T)$, θ, and IN activated fraction.

Part of the results discussed in section 5.1 have been presented in the publication, "Heterogeneous nucleation of ice on anthropogenic organic particles collected in Mexico City" published by D. A. Knopf, B. Wang, A. Laskin, R. C. Moffet, and M. K. Gilles in Geophysical Research Letters, Vol. 37, L11803, 2010.

5.1 Ice Nucleation by Particles Collected during the MILAGRO Campaign

5.1.1 Particle Samples and Chemical Composition

During the MILAGRO campaign, 5 particle samples were collected on March 22, 2006 including three samples (ST0a, ST0b, and ST0c) collected at the T0 sampling site, one sample (ST1) collected at the T1 sampling site, and one sample (ST2) collected at the T2 sampling site. In addition, a particle sample collected at the T0 sampling site on March 24, 2006 is also investigated for chemical analyses and ice nucleation experiments.

Table 5.1 summarizes the particle number density on the substrate, mean particle diameter, and the surface area available for ice nucleation determined by the CCSEM/EDX analysis for the investigated samples. The mean particle diameter is defined as the equivalent circle diameter of the 2–D projected area of the particle observed from the microscopy images. The mean particle diameter ranges from 0.44 to 0.65 μm. The particle number density ranges from 1.4 to 5.0 $\times$ 10^5 mm^{-2}. Combining the particle density, mean diameter, and the sample area observed in the ice nucleation experiments, the particle surface area available for ice nucleation was determined ranging from 4.8 to 8.1 $\times$ 10^{-2} mm^{-2}.

Table 5.1: The sampling location, sampling time (local time), and mean particle size in diameter, particle number density on substrate, surface area of particles available for ice nucleation, and range of IN activated fractions of the investigated samples are presented.

Sample and sampling time	Diameter (μm)	Particle density ($\times 10^5$ mm^{-2})	Surface area ($\times 10^{-2}$ mm^2)	IN activated fraction ($\times 10^{-5}$)
ST0a, 05:35	0.44	3.8	8.0	0.8–1.2
ST0b, 12:35	0.56	1.5	4.8	2.1–7.3
ST0c, 14:20	0.65	1.4	6.3	2.1–9.6
ST1, 13:00	0.51	3.1	8.1	1.5–3.1
ST2, 14:30	0.66	1.5	6.6	2.1–9.4
M1, 05:00	0.52	2	5.0	1.6–7.2

Figure 5.1 shows a typical SEM image for (a) particles collected on March 22 and (b) particles on the M1 sample collected on March 24. The majority of the particles collected on March 22 are coated with organic material and appear in near spherical shapes whereas the particles of the M1 sample exhibit non–spherical, needle-like shapes.

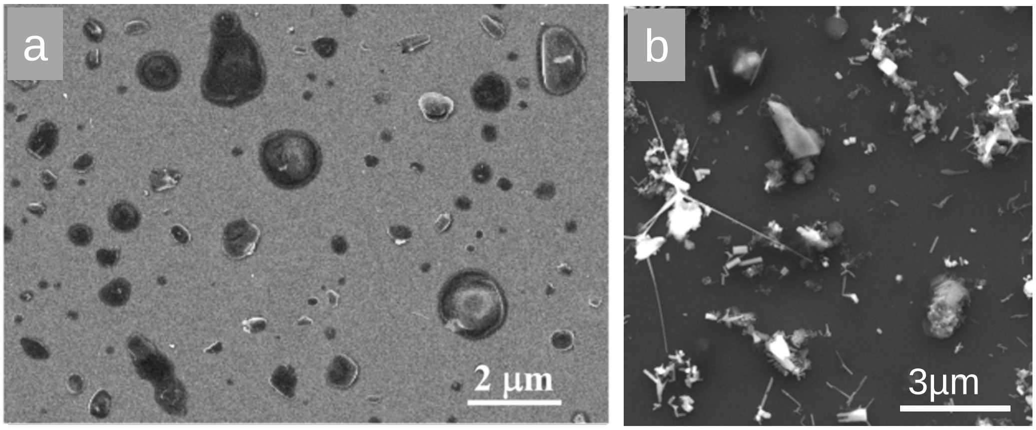

Figure 5.1: A typical SEM image for (a) particles collected on March 22 and (b) particles on the M1 sample collected on March 22. The dark areas indicate organic material.

Figure 5.2 shows the particle–type compositions for samples derived from STXM/NEXAFS collected at different time during the day. Close to the source at the T0 site, particles consist of dust, sulfate species, and particles coated by secondary organics. Significant amount of organic material is associated with every particle measured which is confirmed by CCSEM/EDX and STXM/NEXAFS analyses of a statistically significant number of particles[23]. As shown in Fig. 5.2, the particle-type composition at T0 did not change substantially during the day. Transport from T0 to T1 and T2 led to a significant increase in organic material due to the photochemical formation and processing of SOA[22,23,219].

The M1 particle sample contains a major fraction of internally mixed particles consisting of Pb/Zn chlorides and nitrates which represented the majority of the fine mode particles as determined by a number of complementary techniques, including aerosol time–of–flight mass spectrometer (ATOFMS), CCSEM/EDX, and STXM/NEXAFS[221]. The particle sample was collected after a heavy rainfall resulting in a decreased background aerosol concentration and this is when ATOFMS detected a peak of Pb/Zn–containing particles. The number percentage of the Pb/Zn–containing particles accounts for 61% as detected by ATOFMS and 73% as determined by CCSEM/EDX. These particles were typically mixed with soot indicating a combustion source and their unique single particle chemical compositions closely match signatures indicative of waste incineration[221]. Moffet et al.[221] concluded that many Zn–rich particles composed of $Zn(NO_3)_2{\cdot}6H_2O$ and ZnO possess needle-like structures as shown in Fig. 5.1. For these reasons, this sample was chosen for ice nucle-

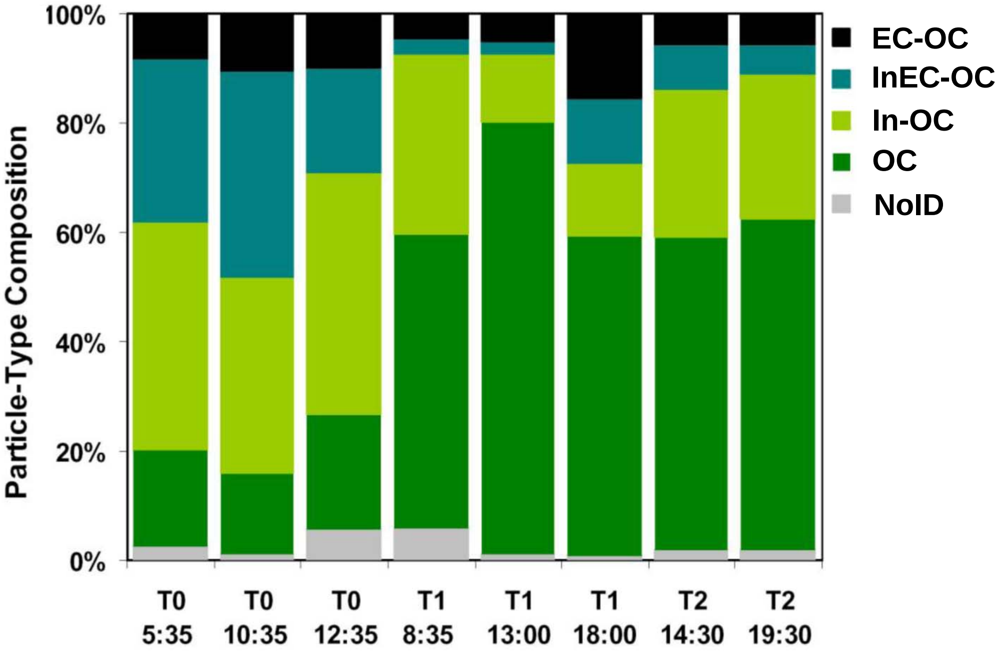

Figure 5.2: The classification of particle types for samples collected at the T0, T1, and T2 sampling site in and around Mexico City based on STXM/NEXAFS analysis. STXM/NEXAFS analysis distinguishes the following components within individual particles: OC–organic carbon, In–inorganic material, and EC–elemental carbon. Combinations of these components are used to define four major particle classes. The OC component is present in all particles. NoID class corresponds to particles that could not be assigned to a specific class because of the low signal to noise.

ation measurements of particles representative of waste incineration[221].

5.1.2 Water Uptake and Ice Nucleation

T0, T1 and T2 samples collected on March 22

Figure 5.3 shows the ice nucleation data for 5 samples collected at T0, T1, and T2 sites on March 22, 2006. The ice nucleation onsets of a blank substrate are also shown, indicating the maximum RH_{ice} values achievable in our experiments. The observed ice nucleation onsets for the three particle samples collected at the T0 site do not show a significant difference within the experimental uncertainties. Thus, the experimental data obtained from these three samples are combined. The same procedure is applied to the two

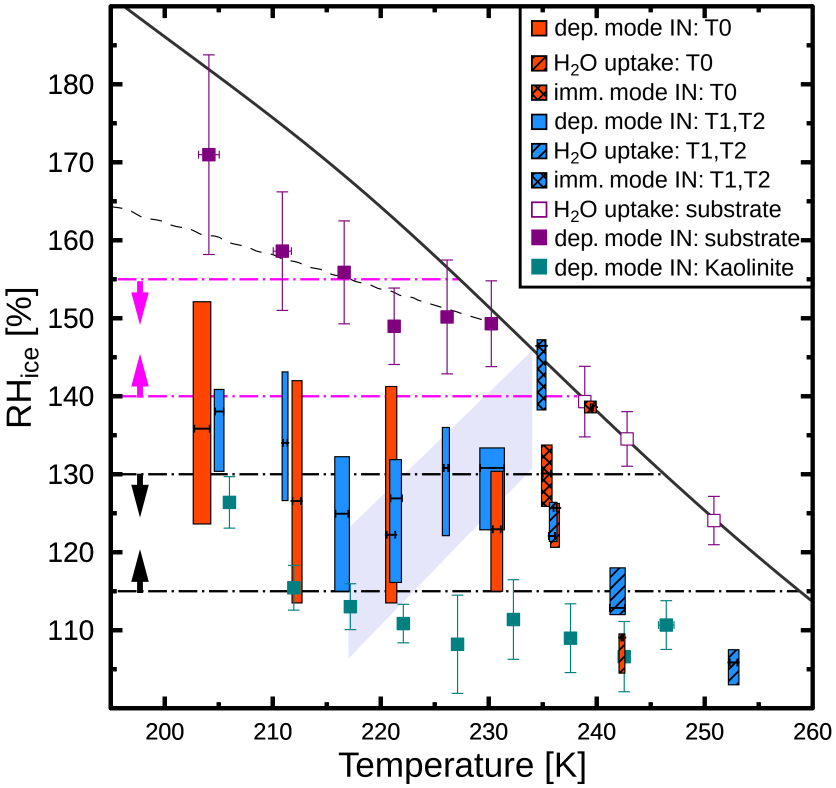

Figure 5.3: Experimentally determined range of heterogeneous ice nucleation onsets of particles sampled in (red bars) and around (blue bars) Mexico City. Shaded and hatched bars represent conditions at which water uptake and immersion freezing were observed, respectively. The horizontal solid lines within the bars indicate the mean IN onsets calculated from multiple observations. Water uptake and ice formation on blank substrates are shown as open and filled purple boxes, respectively. Heterogeneous ice nucleation onsets for Kaolinite particles are shown as dark green solid squares. The dashed line represents RH_{ice} thresholds for homogeneous ice nucleation from an aqueous droplet adapted from Koop et al.[33]. The remaining lines and symbols are identical to those in Fig. 6.1

samples collected at the T1 and T2 sites. The onsets of heterogeneous ice nucleation via deposition mode determined for particle samples collected at the T0 sampling site are shown as red bars in Fig. 5.3. Particles took up water at $T_\mathrm{p} > 230$ K and about 83% RH, and in some cases, demonstrated immersion freezing. Blue bars represent heterogeneous ice nucleation onsets measured for particle samples from the T1 and T2 sites. At the T1 and T2 sites the number of entirely organic particles and extent of organic coating increased substantially[23]. Deposition ice nucleation was observed at $T_\mathrm{p} <$ 230 K. At higher temperatures water uptake was observed and in some cases was followed by immersion freezing. Water uptake on T1 and T2 particle samples also occurred at ~83% RH. Compared to the ice nucleation onset of Kaolinite particles, the particles collected in and around Mexico City can be as efficient at temperatures below 220 K as shown in Fig. 5.3.

Figure 5.3 shows no significant difference in ice nucleation onsets between particles from different sites or time periods. This supports the premise that the outermost layers of organic material may control the IN propensity of the sampled particles; however, effects of inorganic material cannot be entirely ruled out. Increasing organic material in the particles did not significantly affect the heterogeneous ice nucleation efficiency of the particles. This may be attributed to a very thick organic coating so that any additional organic material has little impact on heterogeneous ice nucleation. Additional possibilities include the formation of new IN coupled with the deactivation of IN within the urban plume[259] and particle coagulation. The insensitivity of heterogeneous ice nucleation to additional photochemical processing may facilitate the modeling of ice cloud formation.

The onset conditions for cirrus formation reported for the "Interhemispheric differences in Cirrus properties from Anthropogenic emissions" (INCA) experiment for the northern and southern hemispheres at mean temperatures of ~225 K are also shown in Fig. 5.3. The heterogeneous ice nucleation onsets reported in this study coincide well with onset conditions of cirrus formation typical for the northern hemisphere, i.e. $RH_\mathrm{ice} > 115\%$ at temperatures of 205 to 235 K. Heymsfield and Miloshevich[16] observed that ice formation for orographic wave clouds and cirrus clouds could start as low as ~110% RH_ice which indicates a heterogeneous ice nucleation process. The ice nucleation onsets determined here coincide with these continental cirrus cloud formation via heterogeneous ice nucleation. These results suggest that anthropogenic particles from the urban environment of Mexico City can act as IN under typical tropospheric conditions. Analysis of the INCA data concluded that the northern hemisphere cirrus conditions are controlled by homogeneous and by selective heterogeneous freezing whereas ice crystals are formed predominantly by homogeneous ice nucleation in the cleaner southern hemisphere[17,18].

M1 sample collected on March 24

Figure 5.4 shows that above 231 K water uptake by the particles was observed at 84–89% *RH* followed by immersion freezing at 90–100% *RH*. Below 231 K, these particles nucleated ice via deposition mode between 115 and 148% RH_{ice} with mean onset values of 126–133%.

Figure 5.4 shows that these particles exhibit similar ice nucleation efficiencies via deposition ice nucleation below 231 K as the anthropogenic organic-dominated particles on March 22 which are referred to as MILAGRO organic particles for the remainder of the text. Both organic–dominated and inorganic-dominated particles from this heavily polluted environment can serve as very efficient deposition IN. Pb/Zn-containing particles nucleated ice via immersion freezing after taking up water and possessed higher ice nucleation efficiencies than MILAGRO organic particles. For comparison, the onset conditions of ice nucleation by lead iodide (PbI_2)[37], Pb–containing Kaolinite[38], and Kaolinite[39] are shown in Fig. 5.4. Below 210 K, Pb/Zn–containing particles exhibited high ice nucleation efficiencies that were comparable to Kaolinite particles. Cziczo et al.[38] have shown that Pb–containing Kaolinite particles can serve as efficient IN at temperatures between 235 K and 245 K. An early study by Detwiler and Bernard[37] showed that PbI_2 particles, which were applied in cloud seeding, also exhibit high ice nucleation efficiencies similar to Kaolinite particles. Previous studies have shown that ZnO particles could also serve as IN at 253 K and 263 K[260]. Pb/Zn chlorides and nitrates are soluble in water whereas ZnO is insoluble; thus it would be expected that after water uptake, the insoluble components present in the M1 sample, such as ZnO, served as IN. In summary, these field–collected Pb/Zn-containing particles have a high potential to act as IN via deposition and immersion freezing, corroborating previous studies using laboratory generated particles.

5.2 Particles Collected during the CalNex Campaign

5.2.1 Particle Samples

Particle samples were collected at the ground sampling site on the Caltech campus, Pasadena, CA, during the CalNex field campaign. Two sets of particle samples were chosen for this study including three samples (A2, A3, and A4) collected on May 19 and two samples (B2 and B4) collected on May 23.

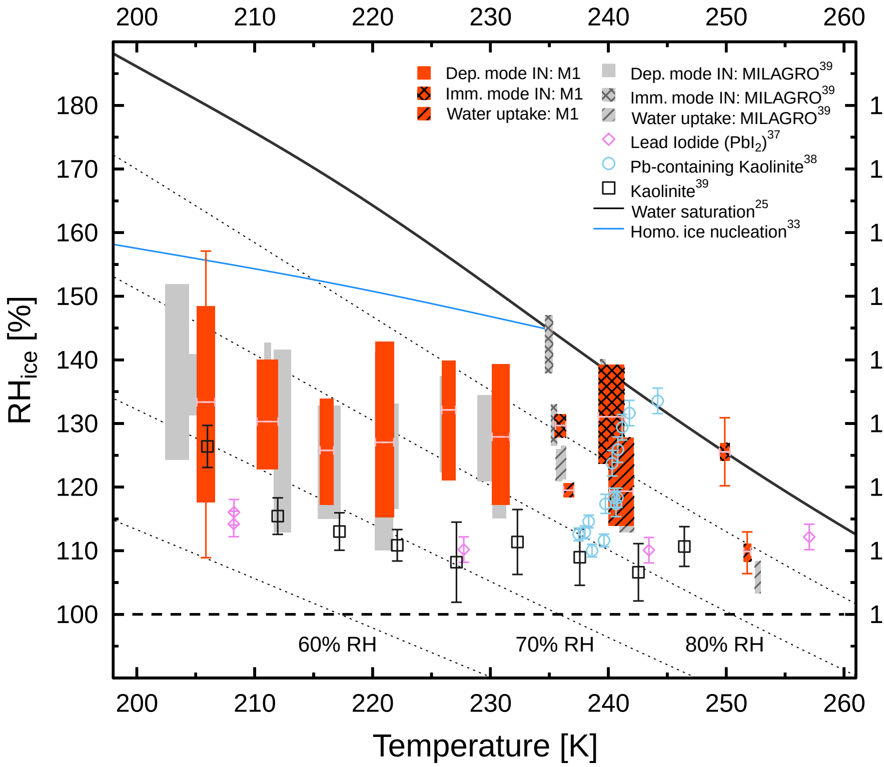

Figure 5.4: The onset conditions for ice nucleation and water uptake as function of temperature and RH_{ice} for particles of the M1 sample are presented in red. The red and gray bars and corresponding shaded and hatched bars are defined as in Fig. 5.8. The horizontal solid lines within the bars indicate the mean ice nucleation onsets. Ice nucleation by lead iodide (PbI_2) from Detwiler and Bernard[37], Pb–containing Kaolinite from Cziczo et al.[38], and Kaolinite from Knopf et al.[39] are shown as diamonds, circles, and squares, respectively. Uncertainties are given on selected temperatures. Corresponding representative error bars are given for the selected data points. The blue solid line represents the RH_{ice} threshold for the homogeneous freezing limit from Koop et al.[33]. The gray bars and corresponding shaded and hatched bars represent conditions of deposition ice nucleation, water uptake, and immersion freezing by MILAGRO organic particles as shown in Fig. 5.3. The remaining lines are identical to those in Fig. 4.3

Table 1 summarizes the particle number density on the substrate and mean particle sizes determined by the CCSEM/EDX analysis for the investigated samples. The mean particle diameter ranged from 0.26 to 0.52 μm. The particle number density ranged from 0.2 to 2.3 × 10^6 mm^{-2}. Combining the particle density, mean diameter, and the sample area observed during the ice nucleation experiments, the particle surface area available for ice nucleation was determined as 0.05 to 0.26 × 10^{-2} mm^{-2}.

Table 5.2: The sampling location, sampling time (local time), and mean particle size in diameter, particle number density on substrate, surface area of particles available during for ice nucleation, and range of IN activated fractions of respective samples are presented.

Sample and sampling time	Diameter (μm)	Particle density ($\times 10^6 \mathrm{mm}^{-2}$)	Surface area $\times 10^{-2}$ (mm^2)	IN activated fraction ($\times 10^{-6}$)
A2, 06–12	0.32	2.3	26	0.6–1.6
A3, 12–18	0.37	1.6	24	0.9–3.4
A4, 18–24	0.39	1.8	24	0.6–2.4
B2, 06–12	0.47	0.8	18	1.8–6.5
B4, 18–24	0.26	0.6	9.0	1.1–7.3

Typical SEM images of the investigated particle samples are shown in Fig. 5.5. Soot particles identified by STXM/NEXAFS, which primarily are produced during combustion processes, are less transparent to the electron beam in the STEM (Scanning Transmitted Electron Microscopy) imaging mode of SEM and thus appear darker than the remaining organic material (see images of the A2, A3, and A4 samples). The high atomic number elements, such as sulfur as identified by CCSEM/EDX analysis, most likely present as sulfate, are also less transparent in STEM images as compared to their thin organic coatings (see images of the B2 and B4 samples). The particle samples collected during the CalNex campaign exhibit visible organic coatings of various thicknesses for the majority of the particles. The coatings of particles on the A2, A3, and A4 samples are thicker than for particles on the B2 and B4 samples (see images in Fig. 5.5). More particles of the A3 sample contain soot/inorganic inclusions than particles of the A2 and A4 samples. Particles of the A2 and A4 samples show near spherical shapes whereas particles of the A3 sample are non–spherical.

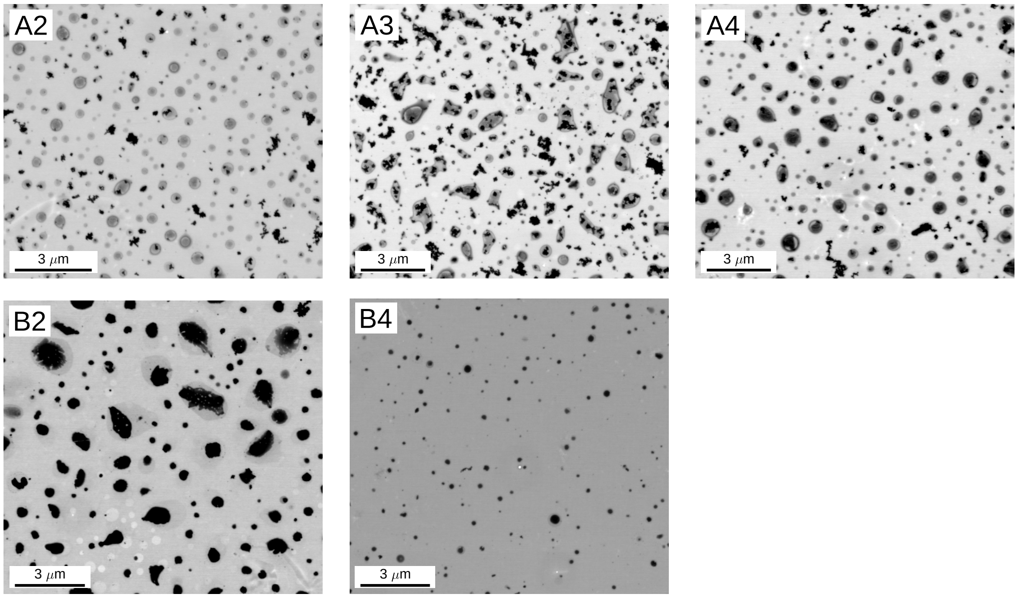

Figure 5.5: Typical SEM images obtained by using STEM (Scanning Transmitted Electron Microscopy) detector for aerosol particles of the A2, A3, A4, B2, and B4 samples collected during the CalNex campaign.

5.2.2 Chemical Composition

As shown in Chapter 3, the chemical composition of individual particles obtained by CCSEM/EDX analysis can be presented by the normalized atomic percentages of elements allowing particles to be classified into different groups. The normalized atomic percentages of elements and classification of particles on the investigated 8 samples collected on May 19 and 23 during CalNex campaign are shown in Fig. 5.6. The normalized atomic percentages of elements for individual particles are shown as stacked bars with the colors indicating the elements. CCSEM/EDX analysis provides the elemental composition for a significant number of individual particles ranging from ∼1100 to 7600 per sample as shown in Fig. 5.6.

The particles in each sample are sorted and classified into different particle types according to CCSEM/EDX and STXM/NEXAFS analyses as described in Chapter 3. The percentage number fraction of the different particle types for each sample as determined by CCSEM/EDX and STXM/NEXAFS is summarized and presented in Fig. 5.7A and B, respectively.

For the samples collected on May 19, as shown in the upper panel of Fig. 5.6, a significant number fraction of particles on the A1, A2, and A3

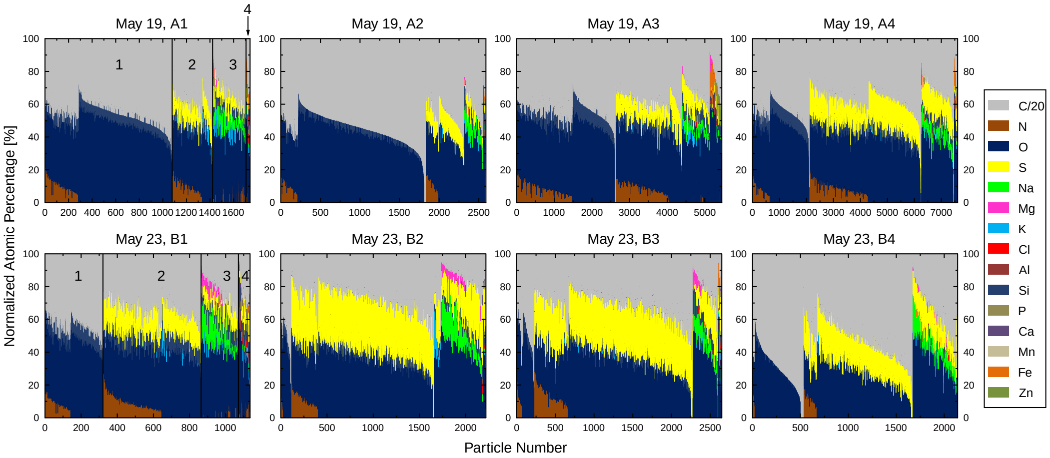

Figure 5.6: Bar plots of CCSEM/EDX data showing elemental composition of individual particles for the samples collected on May 19 and May 23 in Los Angeles during the CalNex campaign. Each plot represents one sample with investigated particle numbers ranging from ~1100 to 7600. Each particle is represented as a stacked bar with colors giving the relative atomic percent of the elements in the particle. The color map for the investigated elements is shown on the right of the figure. The particles are classified into four types as follows: (1) CNO, (2) CNOS, (3) Na/Mg rich, and (4) Others. The particle type is indicated by the number on the plots for the A1 and B1 samples.

samples mainly contains C, N, and O elements which could be organic material or soot particles. As shown in Fig. 5.7A, the fraction of the CNO type particles decreases from 71, to 48 to 28% for A2, A3, to A4 sample, respectively. The number fraction of the CNOS containing particles (CNOS type, likely sulfate) on the A2, A3, and A4 samples increases from 19, to 33, to 54%, respectively. In addition, the normalized atomic percentage of sulfur (yellow) in the CNOS type particles increases which is most evident for the A4 sample as shown in Fig. 5.6. This may due to new particle formation from the oxidation of SO_2 or the aging process of existing particles due to condensation of H_2SO_4[140,163,164]. The A3 particle sample exhibits a higher number fraction of Fe–containing particles (3%) which is included in the fourth particle type compared to the other particle samples (less than 1%). This indicates that the A3 particle sample may have been impacted by a dust event or an industrial plume.

As shown in Fig. 5.6, for the samples collected on May 23, all four particle samples were dominated by CNOS type particles, especially, B2 and B3 sam-

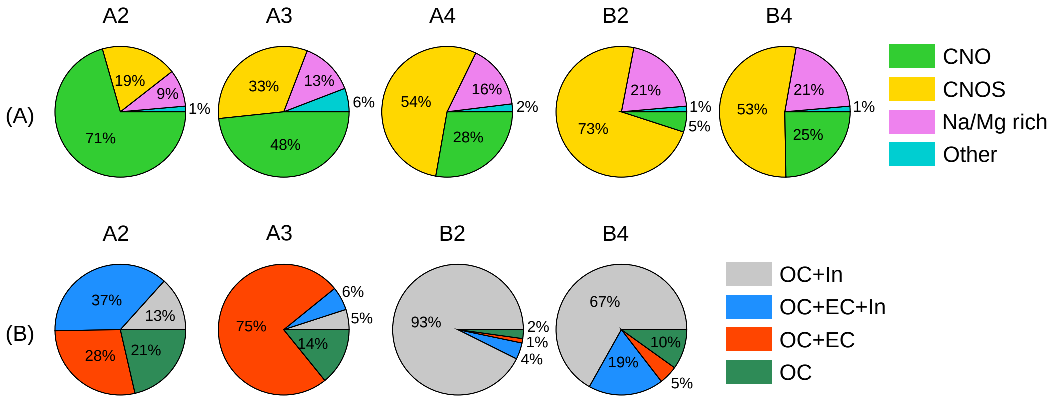

Figure 5.7: The percentage number fraction of identified particle types for each sample as classified by CCSEM/EDX (panel A) and by STXM/NEXAFS (panel B). See text for more details.

ples. As shown in Fig. 5.7, the CNOS particle type contributes 73% and 53% of the particles present in the B2 and B4 samples, respectively. The number fraction of Na and Mg containing particles which are indicative of sea salt was enhanced in the B2 and B4 samples compared to the A2 and A3 samples, especially for the number fraction of Mg–containing particles present in the B2 sample which was ∼10% compared to <1% for the A2 and A3 samples. Overall, CCSEM/EDX analysis indicated that the A2 and A3 samples mainly contained soot associated with organics whereas the particles of the B2 and B4 consisted of sulfate and sea salt indicating the impact of marine sources.

STXM/NEXAFS provides the speciation of the carbonaceous content of individual particles and the mixing state of aerosol particles for the A2, A3, B2, and B4 samples. STXM/NEXAFS analysis classifies four types of particles: (1) OC: particles are mainly carbonaceous; (2) OC+EC: soot with organic coatings; (3) OC+EC+In: particles are coated with organics and have soot and inorganic inclusions; and (4) OC+In: Inorganic particles most of which have a thin organic coating. The STXM/NEXAFS analysis of a statistically significant number of identified particles (up to 760) shows that the majority of particles from A2, A3, B2, and B4 samples possess an organic coating. The percentage number fraction of the different particle types for each sample is shown in Fig. 5.7B.

STXM/NEXAFS analysis of particles indicated that the A2 and A3 samples consisted of particles which were internally and externally mixed with soot/inorganic and organic material, whereas the majority of the particles on the B2 and B4 samples contained a mixture of inorganic and organic material. A total of ~65% of the particles present in the A2 sample fell into two classes: soot with organics (OC+EC), or soot with inorganics and organics (OC+EC+In). Similarly, about 80% of the particles present in the A3 sample fell into these two categories. This indicates that the A2 and A3 samples were affected by anthropogenic sources, such as combustion products from traffic related emissions. In addition, the A3 sample showed an increase of carboxylic groups associated with the particles compared to particles of the A2 sample likely due to heterogeneous oxidation of soot particles by atmospheric trace gases such as O_3, NO_3, and OH during the day[261–264]. The B2 and B4 samples are dominated by inorganic particles containing some organics in the form of a thin coating. The B4 sample contains more particles with soot inclusions and more purely organic particles compared to the B2 sample as shown in Fig. 5.7B. The B2 and B4 samples were much less carbonaceous than the A2 and A3 samples.

The chemical composition indicates that the A2, A3, and A4 particle samples were mainly affected by anthropogenic sources whereas the B2 and B4 particle samples were significantly impacted by marine sources.

5.2.3 Water Uptake and Ice Nucleation

The ice nucleation onset conditions and water uptake by the particles of the A2, A3, A4, B2 and B4 samples were investigated. Ice nucleation experiments were started at low temperatures (below 225 K) where deposition ice nucleation occurs in the absence of liquid water. Subsequently ice nucleation experiments were conducted at a higher temperature range. At higher temperatures, i.e., above 230 K, water uptake and immersion freezing may occur and lead to a change of particle morphology. To investigate if potential morphology changes due to hydration/dehydration cycles affect the deposition ice nucleation efficiency, the ice nucleation experiments were repeated. For the majority of the cases, no significant difference in the ice nucleation efficiency due to previous ice formation and water uptake was observed. For the following discussions, the ice nucleation data of both experimental runs were used.

A2, A3, and A4 Samples

The range of ice nucleation onset conditions and water uptake by particles of the A2, A3, and A4 samples is presented in Fig. 5.8A. Figure 5.8A shows that above 230 K, water uptake by particles of the A3 and A4 samples was observed at RH ranging from 78 to 87%. Figure 5.9 presents in more detail the mean onset RH values for water uptake as a function of particle temperature

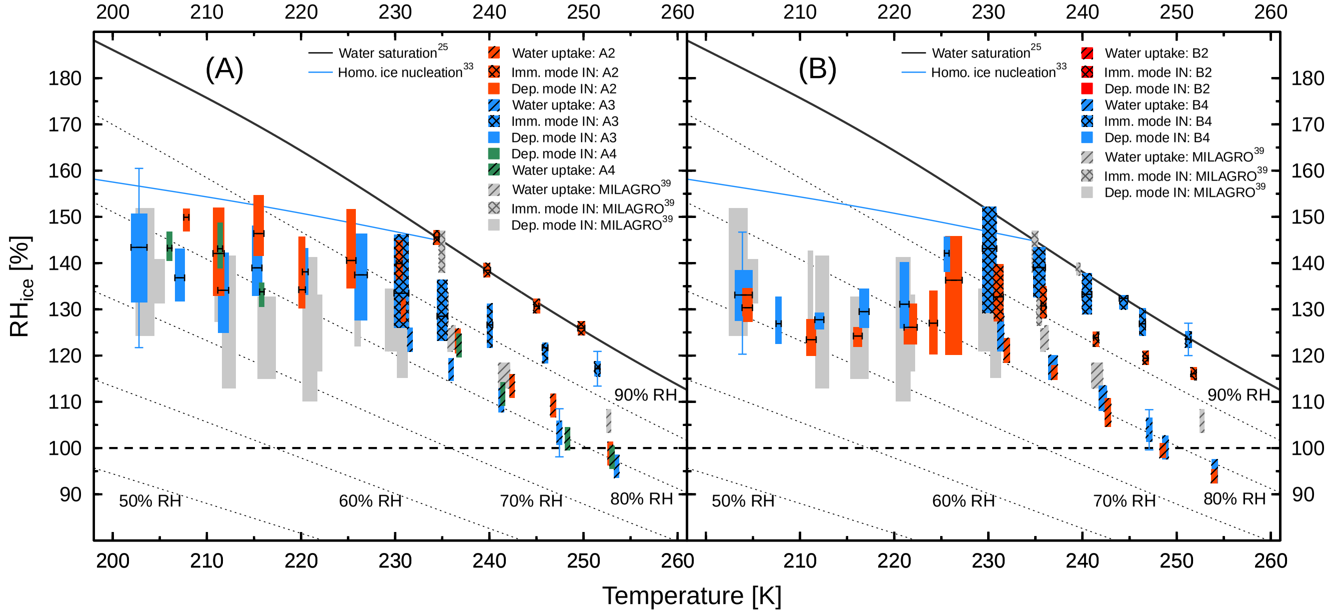

Figure 5.8: The range of onset conditions for ice nucleation and water uptake as a function of temperature and RH_{ice}. Panel A: A2, A3, and A4 particle samples collected on May 19 are indicated as red, blue, and green bars, respectively. Panel B: B2 and B4 particle samples collected on May 23 are indicated as red and blue bars, respectively. The bars and corresponding shaded and hatched bars represent conditions of deposition ice nucleation, water uptake, and immersion freezing, respectively. The horizontal solid lines within the bars indicated the mean ice nucleation onsets. Corresponding representative error bars are given for the selected data points. The black solid and dashed lines indicate water saturation (100% RH) and ice saturation (100% RH_{ice}), respectively. The diagonal dotted lines (top right to bottom left) indicate 90%, 80%, 70%, 60%, and 50% RH. The blue solid line represents the RH_{ice} thresholds for homogeneous ice nucleation of an aqueous droplet with 0.3 μm in diameter corresponding to a homogeneous ice nucleation rate coefficient of about 1.2×10^{12} cm^{-3} s^{-1}. The gray bars and corresponding shaded and hatched bars represent conditions of deposition ice nucleation, water uptake, and immersion freezing by MILAGRO organic particles as shown in Fig. 5.3.

for all investigated samples. Water uptake by the particles of the A3 and A4 samples occurred between 79 and 86% *RH* for temperatures between 272 K and 231 K, respectively. Particles of the A2 sample took up water at *RH* of 81–87% which is a few percent higher than those for particles of the A3 sample. This demonstrates that the particles of the A3 sample were on average more hydrophilic than those of the A2 sample. This may be due to the increased number of carboxylic groups present on particles of the A3 sample. In general, for the particles collected during the CalNex campaign the mean values of *RH* onsets for water uptake increased 3–6% as the particle temperature decreased by 22–35 K. For example, the *RH* onsets of water uptake for the particles of the A4 sample increase from ∼80 to 86% within 35 K when particle temperatures decreased from 272 to 237 K.

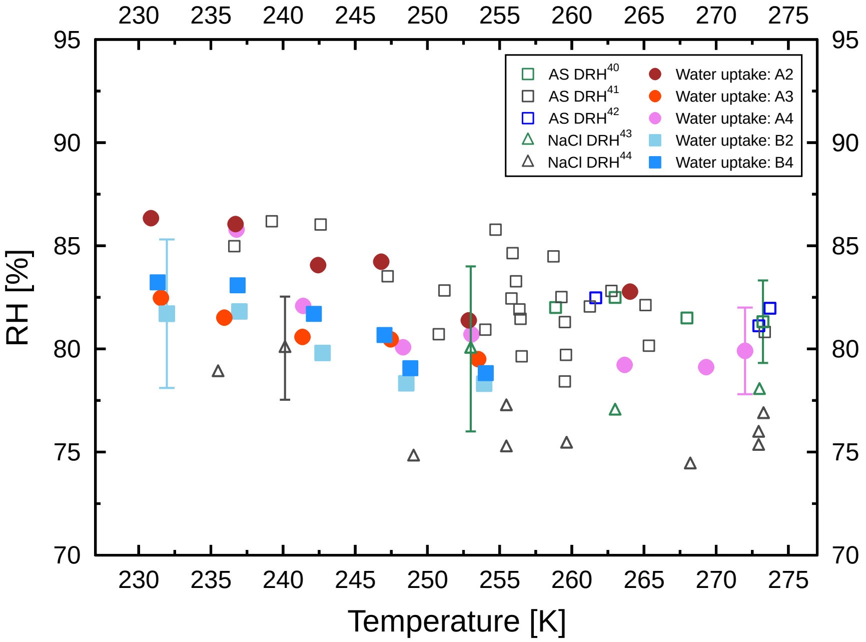

Figure 5.9: The mean onset *RH* values for water uptake by particles of the A2, A3, A4, B2, B4, and M1 samples as a function of temperature. Deliquescent relative humidity (DRH) values of ammonium sulfate (AS) are shown as squares from Onasch et al.[40] (green), Braban et al.[41] (black), and Parsons et al.[42] (blue). DRH of NaCl are shown as green and black triangles from Czizco and Abbatt[43] and Koop et al.[44], respectively. Representative error bars are given for the selected temperatures.

Above 230 K, ice nucleation occurred after water uptake via immersion freezing at *RH* of 91–100% and 84–95% for particles of the A2 and A3 samples, respectively. The particles of the A3 sample showed significant higher ice nucleation efficiency via immersion freezing than those of the A2 sample as presented in Fig. 5.8A. Water uptake by the particles of the A4 sample was observed at *RH* values similar to the particles of the A3 sample but ice formation was not observed until reaching water saturation. Figure 5.8A demonstrates that below 230 K the particles of the A2 sample nucleate ice via deposition mode at mean RH_{ice} values of 134–150%, which are well below water saturation and the homogeneous freezing limit[33]. The particles of the A3 sample exhibited lower mean RH_{ice} onsets for deposition ice nucleation than those of the A2 samples except at 220 K. However, those differences lie within the experimental uncertainties. The enhancement of carboxylic groups on particles of the A3 sample had no significant effect on deposition ice nucleation compared to the particles of the A2 sample.

Ice nucleation and water uptake by particles of the A2, A3, and A4 samples is compared to MILAGRO organic particles. As shown in Fig. 5.8A, the particles of the A2 sample took up water at *RH* values similar to the MILAGRO organic particles above 230 K. However, the particles of the A2 and A3 samples exhibited a significantly higher propensity to nucleate ice via immersion freezing compared to the MILAGRO organic particles, which only nucleated ice in some instances as shown in Fig. 5.3. For temperatures between 210 and 223 K, the particles of the A2, A3, and A4 samples demonstrated lower deposition ice nucleation efficiencies.

B2 and B4 Samples

Figures 5.8B and 5.9 show that the particles of the B2 and B4 samples first took up water at 77–86% *RH* in the temperature range of 230–275 K, and then induce immersion freezing when *RH* was further increased. The *RH* onsets for water uptake increased by 3–6% as particle temperatures decrease by about 22 K for both B2 and B4 particle samples. Adachi et al.[265] showed that sulfate–containing particles collected on May 30, June 13, and June 15 during the CalNex campaign deliquesced at $(80\pm4)\%RH$ at 298.15 K as determined using an environmental TEM. This is similar to *RH* values for water uptake by the particles of the B2 sample which contain a large amount of sulfur as determined by CCSEM/EDX analysis.

Above 230 K, Fig. 5.8B demonstrates that particles of the B2 sample induce immersion freezing at *RH* values of 85–94% after water uptake. They also showed higher ice nucleation efficiency than the particles of the B4 sample which induced immersion freezing at *RH* values of 89–100%. Particles of the

B2 and B4 samples nucleated ice at mean RH_{ice} values from 123 to 142% via deposition mode below 230 K. The RH_{ice} onset values for the particles of the B4 sample (nighttime) were on average ~2–5% RH_{ice} higher than the particles of the B2 sample (morning). However, within the experimental uncertainties, the particles of the B4 sample exhibited similar deposition ice nucleation efficiencies compared to the particles of the B2 sample. The data demonstrate that the particles of B2 and B4 samples are very efficient ice nuclei which can induce deposition ice nucleation at RH_{ice} as low as 120%.

The particles of the B2 and B4 samples showed similar deposition ice nucleation efficiencies below 230 K as MILAGRO organic particles. However, particles of the B2 and B4 samples exhibited significantly higher efficiencies to nucleate ice via immersion freezing above 230 K compared to MILAGRO organic particles. Particles of the B2 morning sample were impacted by marine sources and showed a higher propensity to form ice via both deposition nucleation and immersion freezing compared to the particles of the A2 morning sample, which were affected by anthropogenic sources as shown in Fig. 5.8.

5.3 Ice Nucleation Analysis of Field-Collected Particles

The data analysis here does not attempt to determine if the underlying heterogeneous ice nucleation process is stochastic or deterministic in nature due to the heterogeneity and complexity of investigated ambient particles. However, the experimental data are analyzed using both CNT and SH approach for future interpretation and implementation in ice nucleation and cloud resolving models.

The experimentally obtained deposition ice nucleation onsets are used to to derive J_{het}, K, θ, and IN activated fraction for all the investigated field-collected particle samples based on the the same methods described in previous Chapters.

5.3.1 J_{het} and K for MILAGRO Particle Samples

Experimentally derived J_{het} and $K(T)$ values for deposition ice nucleation for particle samples collected during the MILAGRO campaign as a function of temperature are presented in Fig. 5.10. J_{het} values are a strong function of temperature and increase exponentially by ~2 orders of magnitude as shown in Fig. 5.10. J_{het} values for all MILAGRO particle samples are similar due to the similar deposition ice nucleation efficiencies as discussed above. The

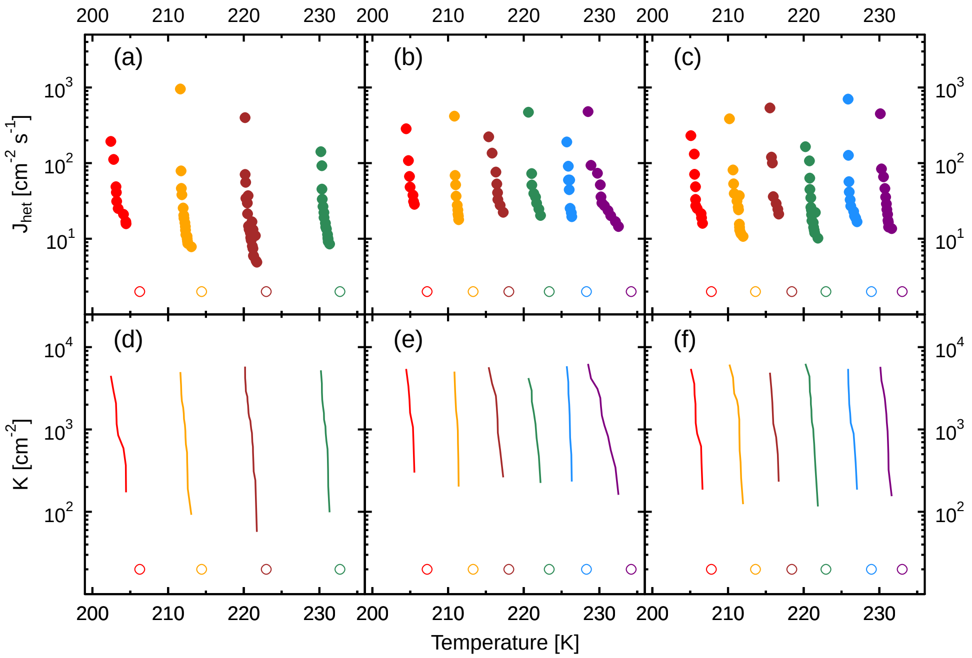

Figure 5.10: Experimentally derived heterogeneous ice nucleation coefficients, $J_{\rm het}$, and cumulative ice nuclei spectra, $K(T)$, for deposition ice nucleation as a function of temperature. $J_{\rm het}$ values are given in panel (a), (b), and (c) and $K(T)$ in panel (d), (e), and (f) for the T0, T1/T2, and M1 samples, respectively. Individual colors represent the experiments conducted from the same starting temperature at which $RH_{\rm ice} = 100\%$. The open circles represent corresponding starting temperatures.

derived $K(T)$ also demonstrates a strong temperature dependence for all the particle samples as shown in Fig. 5.10d, e, and f. $K(T)$ increases by $\sim$1–2 orders of magnitude within a few degrees Kelvin from $\sim$100 to $\sim 10^4$ cm^{-2}.

5.3.2 $J_{\rm het}$ and K for CalNex Particle Samples

Experimentally derived $J_{\rm het}$ and $K(T)$ values for deposition ice nucleation for particle samples collected during the CalNex campaign were presented in Fig. 5.11. For the same initial particle temperatures, $J_{\rm het}$ increased exponentially by $\sim$1–2 orders of magnitude within a few degrees Kelvin. The particle samples exhibited similar $J_{\rm het}$ values whereas the B4 particle sample exhibited slightly higher $J_{\rm het}$ values than the other samples at similar temperatures due to the higher ice nucleation efficiencies of particles present in the B4 sample. Although $K(T)$ exhibited a similar temperature dependence for all investi-

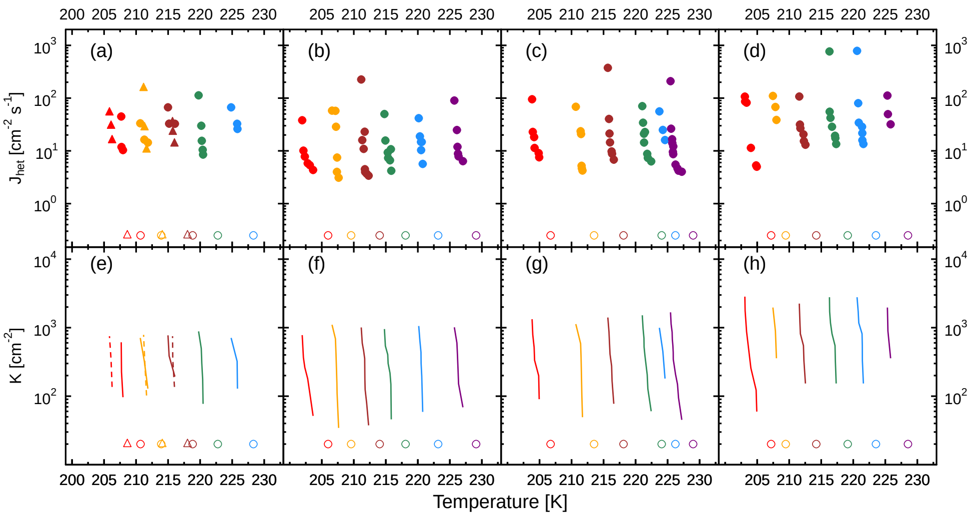

Figure 5.11: Experimentally derived heterogeneous ice nucleation coefficients, J_{het}, and cumulative ice nuclei spectra, $K(T)$, for deposition ice nucleation as a function of temperature. J_{het} values are given for (a) A2 (circles) and A4 (triangles), (b) A3, (c) B2, and (d) B4 particle samples. $K(T)$ are given for (e) A2 (solid lines) and A4 (dashed lines), (f) A3, (g) B2, and (h) B4 particle samples. Individual colors represent experiments conducted at the same starting temperature at which $RH_{\text{ice}} = 100\%$. The open symbols represent corresponding starting temperatures.

gated samples, the maximum $K(T)$ values for the B2 and B4 particle samples were relatively higher compared to those of the other particle samples as shown in Fig. 5.11 which most likely was due to a higher ice nucleation efficiency.

5.3.3 IN Activated Fraction

The ranges of IN activated fractions are presented in Table 5.1 and 5.2 for particle samples collected during the MILAGRO and CalNex campaign, respectively. For A2, A3, and A4 samples, the IN activated fraction ranged from ∼0.6 to ∼3.4 $\times 10^{-6}$ whereas for B2 and B4 samples it ranges ∼1.1 to ∼7.3 $\times 10^{-6}$ as shown in Table 5.2. This indicated that particles on the B2 and B4 samples were more efficient IN than particles on the A2, A3, and A4 samples in deposition mode as shown in Fig. 5.8. For particle samples collected during the MILAGRO campaign, all the investigated samples exhibited a similar range of IN activated fraction which ranged from ∼0.8 to ∼9.6 $\times 10^{-5}$. This was due to similar ice nucleation efficiency of the investigated particles as shown in Fig. 5.3 and 5.4. In general, the IN activated fraction for particle samples collected during the CalNex campaign was about one order lower than those of particle samples collected during the MILAGRO campaign. This difference was mainly due to the difference in total particle number available for ice nucleation.

5.3.4 Contact Angle of Field-Collected Particles

The mean θ values for the investigated field-collected particles as a function of temperature and RH_{ice} are shown in Fig. 5.12a and b, respectively. The uncertainty in θ is mainly due to the uncertainty in RH_{ice} and to a lesser extent by J_{het} as discussed in Chapter 4. The investigated particle samples have mean θ values ranging from ∼20° to 28° for deposition ice nucleation. In general, the B2, B4, and MILAGRO particle samples exhibit lower mean θ values indicating a higher ice nucleation efficiencies. This can be seen from Figs. 5.8 and 5.4 showing that the particles on these samples nucleate ice at lower mean onset RH_{ice} compared to the particles on the A2, A3, and A4 samples at same temperatures. For comparison, θ for Kaolinite particles is also presented in Fig. 5.12a. Overall, the investigated field-collected particle samples studied here exhibit larger θ values and thus are less efficient IN than Kaolinite particles at temperature between 215 to 250 K. Below 215 K, θ derived from Kaolinite and from the field-collected particles come closer indicative of similar ice nucleation efficiencies.

Figure 5.12b shows the mean θ values for deposition ice nucleation as a function of onset RH_{ice} for the field-collected particle samples and θ for various organic and inorganic particle types which have been presented in Fig. 4.6. Figure 5.12b also shows the proposed parameterization of θ as a function of onset RH_{ice} given in Chapter 4. As shown in Fig. 5.12b, θ for the investigated field–collected particles, which possess various chemical composition and morphology, fit well with the parameterization within the experimental uncertainties.

5.4 Effects of Particle Morphology and Chemical Composition

For temperatures above 231 K, the chemical composition of the particles impacted by anthropogenic and marine sources affect the water uptake and immersion freezing efficiencies. Particles of the A3 sample that contain more carboxylic functional groups on the particle may be more hydrophilic and thus take up water at lower RH than particles of the A2 sample. Particles present in the B2 and B4 samples exhibit water uptake behaviors similar to

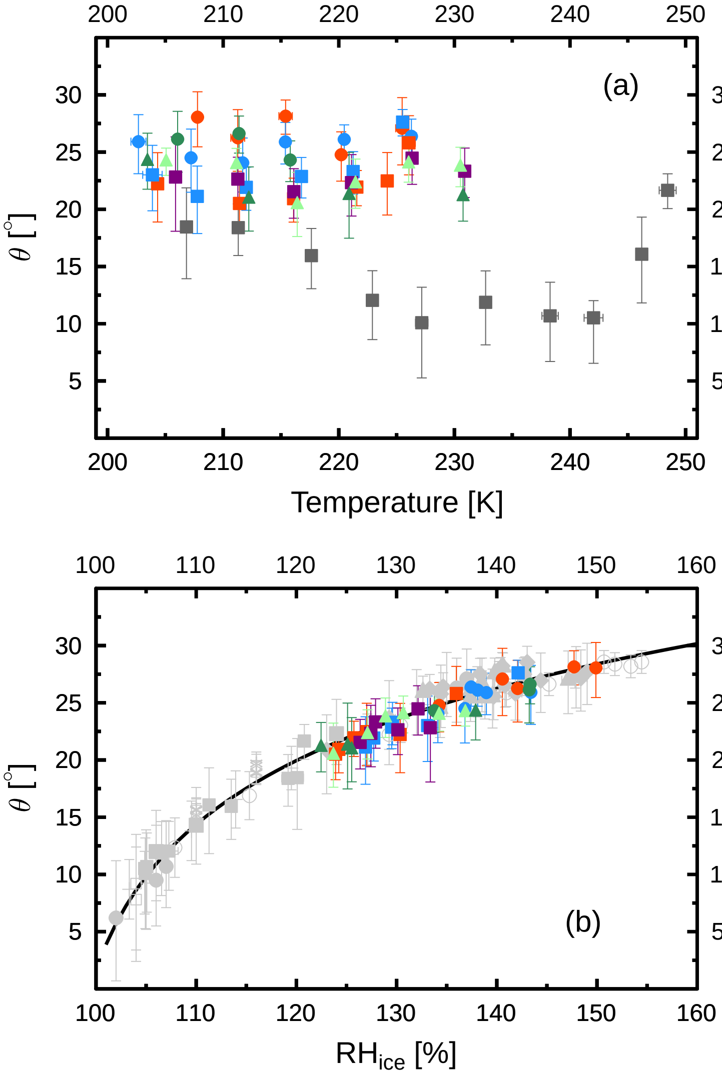

Figure 5.12: The mean values of contact angles, θ, calculated from experimentally derived J_{het} for deposition ice nucleation (a) as a function of temperature and (b) as a function of RH_{ice}. Red, blue, and green colored circles represent the A2, A3, and A4 particle samples, respectively. Red, blue, and purple squares represent the B2, B4, and M1 particle samples, respectively. Light green and green triangles represent the T0 and T1/T2 samples, respectively. The solid line represents the parameterization of θ as a function of RH_{ice} according to Eq. 4.8 and gray symbols represent θ values for various particle types as shown in Fig. 4.6.

each other. For comparison, the deliquescence relative humidity (DRH) of ammonium sulfate and NaCl below 275 K[40–44] are shown in Fig. 5.9. The DRH of ammonium sulfate increases from ∼80 to 86% whereas DRH of NaCl increases from ∼75 to 80% as temperature decreases from 275 to 235 K. The mean onset values of water uptake by particles on the A2, A3, A4, B2, and B4 samples exhibit a similar temperature dependency compared to ammonium sulfate and NaCl particles.

Immersion freezing is triggered by the insoluble components of the particles. Thus, the insoluble cores play an important role in determining immersion freezing efficiencies of the particles. The differences in immersion freezing onsets among the A2, A3, and A4 particle samples is most likely due to the differences of the insoluble components of the inclusions. As discussed above, particles on the A2 and A3 samples are efficient immersion freezing IN and the majority of those contain soot. Although the efficiency of soot particles serving as IN remains unclear[3,9,10,12,13,196,199,203,204,266–269], several studies have shown that soot particles could act as IN[12,196,199,203,204,268,269]. The particles with an enhanced number of carboxylic groups may contribute to the higher immersion freezing efficiency of the A3 sample compared to the A2 sample since the carboxylic groups may provide more hydrogen bonding sites to attract water molecules[20]. The number fraction of particles containing metals including Fe, Zn, Ca and Al elements, is ∼6% for the A3 particle sample compared to ∼1% for the A2 particle sample as determined by CCSEM/EDX analysis. In particular, the Fe–containing particles account for 3% of the A3 particles compared to 0.6% for the A2 particle sample. This indicates that the particles of the A3 sample may consist of mineral dust inclusions which could result in the corresponding higher immersion freezing efficiencies.

No water uptake is observed prior to deposition ice nucleation below 230 K for all investigated particle samples. The chemical and physical characteristics of particle surfaces, such as chemical functional groups, hygroscopicity, and morphology, determine corresponding deposition ice nucleation efficiencies[13,20,214]. As discussed above, the particles on the A3 sample have more carboxylic functional groups but do not exhibit significantly different deposition ice nucleation efficiencies than those on the A2 sample. Thus, the abundance of carboxylic groups in particles may have a minor effect on deposition ice nucleation. With less or thinner organic coatings present, the inclusions may affect deposition ice nucleation as indicated by the contrasting ice nucleation efficiencies between particles on the sulfate-dominated B2 and B4 samples and particles on the A2 and A3 samples.

It is commonly assumed that the efficiency of heterogeneous ice nucleation depends on active sites which can be associated with defects, cracks, cavities, and chemical and physical bonds allowing the enhanced interaction with water vapor[20]. Here, we can only hypothesize about the different deposition ice nucleation efficiencies of the various particle samples. The number of these morphological irregularities on the particle surface which initiate ice nucleation, for instance through a “negative Kelvin effect”, i.e. a decrease in the ice vapor pressure due to a concave curvature of entrained water or ice within a cavity, may result in different ice nucleation efficiencies.

The organic coating of the particles collected during the CalNex campaign may be in an amorphous solid state at freezing temperatures[179,209,270] and thus may provide a sufficient number of active sites to initiate deposition ice nucleation. The coating of particles on the A2, A3, and A4 samples may be in an amorphous state and thus exhibit similar morphological irregularities on the particle surface resulting in similar deposition ice nucleation efficiencies as observed. For particles of the B2 and B4 samples which contain more inorganic inclusions associated with less or incomplete organic coatings, the inorganic inclusions of particles may exist in a crystalline state and/or penetrate the organic coating and thus may provide more active sites than particles of the A2, A3, and A4 samples which possess an organic coating with a smoother surface structure. In turn, this renders the particles of the B2 and B4 samples more efficient in deposition ice nucleation than those of A2, A3, and A4 samples. Particles of the B2 and B4 samples may exhibit similar morphology and thus similar numbers of active sites, resulting in insignificant differences in the corresponding deposition ice nucleation efficiencies is insignificant. The crystalline state and corresponding surface irregularities of the particles on the M1 sample may also provide more deposition ice nucleation active sites. Overall, the results discussed above indicate that physical state and morphology may be the dominant factors controlling deposition ice nucleation. However, these factors may ultimately depend on the chemical nature of the particle compounds which governs the phase state at these low temperatures.

5.5 Comparison with Previous Studies

Organic material in the particle phase can affect the phase transition of aerosol particles[178]. Organic particles may also exhibit different phases as discussed in Chapter 2. Different phases of the organic species may result in different interactions with water vapor affecting the ice nucleation efficiency of the particles. This indicates that the complex organic and organic-containing atmospheric aerosol particles may behave differently compared to purely organic particles or particles with a simple mixture of organics. In this section, the ice nucleation efficiency of atmospheric aerosol particle collected during the

MILAGRO and CalNex field campaigns are compared with those of laboratory-generated organic and organic-containing particles serving as proxies of atmospheric aerosol particles.

Figure 5.13 shows heterogeneous ice nucleation data from previous studies compared with the data for particles collected during the CalNex and MILAGRO campaign. As discussed in Chapter 1, in general, most of the laboratory-generated organic or organic-containing particles fall into two separate classes: very efficient IN which activate at ∼115% RH_{ice} or inefficient IN that activate at $RH > 90\%$. Ice nucleation onsets observed from field-collected particles in this study are in stark contrast to previous ice nucleation data of laboratory-generated organic particles. Laboratory-generated particles rarely exhibit ice nucleation efficiencies similar to those of field-collected particles presented in this study. One such example of agreement, above 230 K, are the soot particles investigated by Möhler et al.[9], Dymarska et al.[3], and Kanji et al.[45] which could nucleate ice at RH value ($> 90\%$) similar to the field-collected particles from the CalNex campaign. Below 230 K, soot particles coated with H_2SO_4 induced ice formation at RH_{ice} values similar to the field-collected particles but most likely via immersion freezing[9,12]. On the other hand, illite coated with SOA and pure SOA exhibit lower ice nucleation efficiencies compared to the field-collected particles[11]. In general, ice nucleation data derived from controlled, less complex, laboratory-generated particles do not well represent the ice nucleation behavior of field-collected particles.

Figure 5.13 compares ice nucleation onsets by the field-collected and laboratory generated particles with onsets of continental cirrus formation[16] and cirrus formation reported during the INCA field study[17,18]. Heymsfield and Miloshevich[16] observed that ice formation for orographic wave clouds and cirrus clouds could start as low as ∼110% RH_{ice} which indicates a heterogeneous ice nucleation process. Haag et al.[18] and Ström et al.[17] concluded that cirrus cloud formation in the Southern Hemisphere was initiated predominantly by homogeneous ice nucleation at RH_{ice} between 140 and 155% whereas in the Northern Hemisphere cirrus cloud formation occurred via homogeneous and selective heterogeneous nucleation at RH_{ice} between 115 and 130% at mean temperatures of ∼225 K. The ice nucleation onsets measured here for the investigated different particle types collected in different anthropogenically affected regions, coincide well with the observed conditions for cirrus cloud formation. The majority of the laboratory studies however indicate that carbonaceous particles (soot and organic particles) are inefficient IN under conditions relevant for cirrus formation[16–18] as shown in Fig. 5.13. Only a small part of reported ice nucleation data from laboratory-generated particles coincides with onset conditions relevant for cirrus formation. From these results, we conclude that

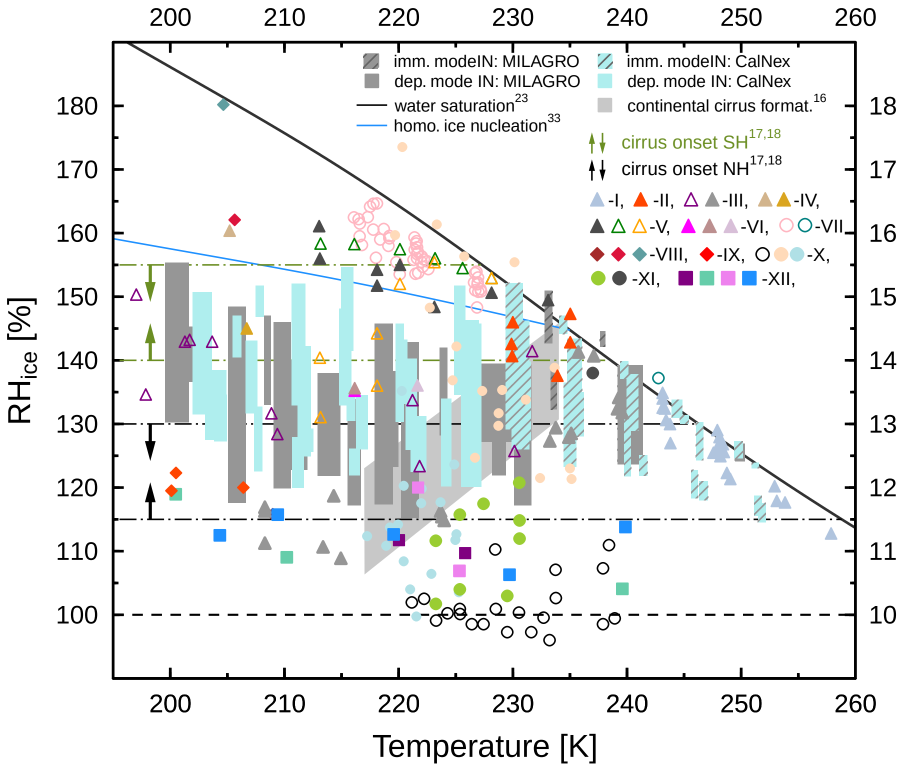

Figure 5.13: Heterogeneous ice nucleation onsets of the particles collected during the MILGRO and CalNex campaign indicated as gray and light cyan bars. Laboratory-generated particles and cirrus cloud formation conditions from previous studies are adapted from Knopf et al.[39]. The individual symbols listed in the figure legend correspond to ice nucleation measurements from the following particles: I, Ozone oxidized soot from Dymarska et al.[3]; II, graphite spark generated soot from Kanji et al.[45]; III, sulfuric acid coated soot, and uncoated soot from Möhler et al.[9]; IV, soot containing different amounts of sulfur from Möhler et al.[10]; V, soot, soot coated with a monolayer, and multiple layers of sulfuric acid from DeMott et al.[12]; VI, three different types of soot from Koehler et al.[13]; VII, biomass burning particles from two studies from DeMott et al.[14] and Petters et al.[15]; VIII, SOA coated Arizona test dust, SOA coated illite, and pure SOA from Möhler et al.[11]; IX, glassy citric acid from Murray et al.[46]; X, hydrated NaCl from Wise et al.[47], glutaric acid, and glutaric acid-ammonium sulfate from[5]; XI, NaCl from two studies from Wise et al.[47] and Wagner et al.[48]; XII, ammonium sulfate from four studies from Wise et al.[49], Shilling et al.[4], Abbatt et al.[50], and Knopf[51]. The remaining lines and symbols are identical to those in Fig. 5.3.

current laboratory proxies of organic particles are not sufficiently representative to infer heterogeneous ice nucleation efficiency of anthropogenic organic material.

5.6 Conclusions

The experimental ice nucleation data demonstrate that anthropogenically affected and marine impacted particles with various chemical and physical properties exhibit distinctly different ice nucleation efficiencies and can serve as efficient IN at atmospheric conditions typical for cirrus and mixed phase clouds. The ice nucleation onsets of the investigated field-collected particles from different anthropogenically affected locations coincide with the observed conditions for cirrus cloud formation. This indicates the potential link between aerosol particle composition generated by, or modified by human activities, and ice cloud formation processes, and thus climate if the human activities persist over significant spatial and temporal values.

The chemical composition of the particles impacted by either anthropogenic or marine sources affects the water uptake and immersion freezing at temperatures relevant to mixed-phase cloud formation. Aged particles which contain more carboxylic functional groups are more hydrophilic and thus take up water at lower RH. The chemically different insoluble inclusions of the particles yield different immersion freezing efficiencies. For deposition ice nucleation at temperatures relevant to cirrus cloud formation, the physical properties and morphologies of particles may play an important role in controlling the ice nucleation efficiency. The reason for this behavior is not entirely clear but most likely due to the formation of an amorphous phase of the organic material providing active sites to nucleate ice at low temperatures typical for deposition nucleation. Thus, the particles' chemical and physical properties have different effects on corresponding ice nucleation efficiencies which also depends on the nucleation mode and temperature regime.

Compared to the existing literature data, ice nucleation onsets observed for field-collected particles in this study are in stark contrast to previous ice nucleation data on laboratory-generated organic particles. Current laboratory proxies of organic particles are not sufficiently representative to infer heterogeneous ice nucleation efficiency of anthropogenic organic material. Clearly, more ice nucleation studies using field-collected particles combined with in–depth analyses of particle chemical and physical properties are necessary to assess their impact on atmospheric ice crystal formation and subsequent effects on the hydrological cycle and climate. The development of novel analytical techniques capable of observation of ice nucleation at the microscopic level of individual particles are needed to examine ice nucleation active sites and to investigate the effects of chemical composition and morphological features on the ice nucleation efficiency of atmospheric particles.

Chapter 6

Heterogeneous Ice Nucleation by Laboratory–Generated Amorphous Secondary Organic Aerosol Particles

This chapter presents the determination of heterogeneous ice nucleation and water uptake by amorphous SOA particles with different O/C ratios generated from the oxidation of naphthalene with OH radicals and O_3, serving as surrogates of anthropogenic SOA particles. Experimentally obtained deposition ice nucleation onsets are used to derive J_{het}, $K(T)$, θ, and IN activated fraction. The upper limits of the glass transition temperature (T_g) as a function of RH for the amorphous SOA particles are derived, based on the theoretical frame work proposed by Koop et al.[19]. The observed heterogeneous ice nucleation and water uptake onset by amorphous aerosol particles for different relevant atmospheric temperature and RH regimes are discussed.

In collaboration with Boston College and Aerodyne Research. Inc., the generation and collection of amorphous SOA particles were conducted at Boston College. The chemical and physical properties of investigated SOA particles were determined and analyzed by my collaborators.

6.1 Characteristics of Laboratory-Generated Amorphous SOA Particles

6.1.1 O/C Ratios of Particles

SOA particles were generated via gas–phase oxidation of naphthalene with OH radicals and O_3, followed by homogenous nucleation of gas phase products. Three types of SOA particles with atomic O/C ratio of 1.0, 0.54, and 0.27 were generated by changing the OH exposure of naphthalene in the PAM flow reactor to $\sim 2.8 \times 10^{11}$, 1.0×10^{12}, and 2.2×10^{12} molec cm^{-3} s, respectively. Assuming typical 24-hour average ambient OH concentration of 1.5×10^{6} molec cm^{-3},[271] these three different OH exposures correspond to oxidation times of ~2, 8, and 17 days. Experiments were conducted at RH of ~30±5% depending on the temperature in the PAM flow reactor (22–32°C) at different UV lamp settings for OH generation. During particle collection, the mass spectra of SOA particles were recorded by an Aerodyne time–of–flight aerosol mass spectrometer and used to derive the O/C ratio of SOA particles[272,273]. Table 6.1 summarizes the mean particle diameter, particle number density on the substrate, and total surface area of particles available for ice nucleation as determined using an optical microscope.

Table 6.1: The mean particle diameter, particle number density on substrate, total surface area of particles available for ice nucleation, and range of IN activated fractions of the investigated samples are listed.

Sample	O/C Ratio	Diameter (μm)	Number density ($\times 10^{4}$ mm^{-2})	Surface area ($\times 10^{-2}$ mm^{2})	IN activated fraction ($\times 10^{-4}$)
High O/C	1.0	0.74	1.2	1.1	0.9–6.7
Medium O/C	0.54	1.06	3.0	5.4	0.4–2.3
Low O/C	0.27	0.73	3.9	3.0	0.3–1.1

6.1.2 Amorphous State of Particles

When an aerosol particle impacts with a surface, part of the particle's kinetic energy is dissipated during the deformation process and part is transferred elastically into kinetic energy of rebound. Particles will bounce off the impaction surface if the rebound energy is larger than the adhesion energy. In general, harder materials, larger particles or greater impact velocity will lead to a larger bounce probability, although the roughness of the collecting surface also plays a significant role[205,206,274,275]. For example, a liquid droplet will deform and tend to adhere to a smooth surface whereas a solid glass marble is more likely to bounce off upon collision.

In a cascade impactor, the collection efficiency for aerosol particles depends on particle size, shape, morphology and physical state during the impacting process[274,275]. The bounce of particles (e.g., solid and larger particles) perturbs the particle collection as larger particles are transferred to lower stages upon bouncing. Virtanen et al.[205] utilized this characteristic feature of an impactor as a tool for examining the physical state of aerosol particles using an electrical low-pressure impactor (ELPI). When particle bounce occurs in an ELPI, an excess current is measured in the lowest impactor stages due to the charges carried by the bounced particles. By analyzing the difference in bounce-affected measured currents with ideal non-affected currents, Virtanen et al.[205] quantified the degree of bounce, the bounce factor of the particles, by the fraction of the excess current relative to the idealized signal. Particles with different phase states would exhibit different bounce factors. For example, crystalline ammonium sulfate particles have a bounce factor range from 0.1 to 1[205,206] whereas amorphous solid polystyrene particles exhibit a bounce factor of 0.3–0.5[205]. In contrast, the bounce factor of dioctyl sebacate (liquid droplets with a moderate viscosity) is less than 0.05[205].

Virtanen et al.[205] showed that SOA particles with mean diameters of 40–120 nm generated from the O_3- and OH–initiated oxidation of pine exhibited a bounce factor of 0.2–0.4. Virtanen et al.[205] also showed that the bounce factor for atmospheric SOA is between 0.05 and 0.3. The observed bounce factor strongly suggested that the biogenic SOA particles are in an amorphous solid rather than a liquid state[205,205]. In this study, for the SOA particles generated from the oxidation of naphthalene with OH radicals and O_3, the bounce factor of 0.6±0.2 was determined at room temperature and $\sim$35% RH. Thus, under these conditions, the SOA particles exhibited an amorphous semi–solid and probably solid state.

6.2 Water Uptake and Ice Nucleation

The onset conditions for heterogeneous ice nucleation and water uptake by amorphous SOA particles were determined using two independent samples for each O/C ratio. Figure 6.1 summarizes the range of onset conditions for heterogeneous ice nucleation and water uptake for the investigated amorphous SOA particles.

Above 230 K, water uptake by the SOA particles was observed and followed by immersion freezing in some cases. As shown in Fig. 6.1, SOA particles with high O/C ratio took up water at mean values of 80–85% RH between 230 and

250 K. For some cases, between 241 and 230 K, immersion freezing occurred after water uptake. SOA particles with medium and low O/C ratio also took up water but at higher RH values compared to particles with high O/C ratio. Between 230 and 242 K, SOA particles with medium and low O/C ratios also initiated ice nucleation via immersion freezing after water uptake. For all the SOA particle samples, no ice nucleation was observed above 242 K.

Below 230 K, the SOA particles with high O/C ratio nucleate ice via deposition mode as low as 135% RH_{ice} with mean values of 141–149% as shown in Fig. 6.1. The RH_{ice} ice nucleation onset slightly increased as temperature decreased. Although, in a few cases, the SOA particles with medium and low O/C ratio nucleated ice at RH_{ice} of 123–135% at temperatures between 215 and 225 K, the mean onset RH_{ice} values are very similar. In general, the SOA particles with different O/C ratios nucleated ice at similar mean RH_{ice} values and thus exhibited similar deposition ice nucleation efficiencies, independent of O/C ratio, as shown in Fig. 6.1. For all investigated particles it appears that the mean onset RH_{ice} value increases from ∼140% at 225 K to ∼150% at 203 K.

As discussed above, these SOA particles adopt an amorphous semi–solid and probably an amorphous solid state at room temperature and ∼35% RH. The organic particles in an amorphous semi–solid state might deliquesce upon increasing humidity in a gradual deliquescence process under our experimental conditions[19,205,209]. This humidity–induced phase transition also occurs for the investigated amorphous SOA particles at temperatures between 230 and 250 K as indicated by the observed water uptake at 80–95% RH. A aerosol particle in an amorphous solid state may form a liquid/viscous shell and a semi-solid or solid core due to slow water diffusion into particles, in particular at lower temperatures[19,209,210]. For temperatures between 230 and 250 K, the diffusion coefficient of water ($D_{\mathrm{H_2O}}$) in an amorphous solid particle would be $\sim10^{-13}$ cm^2 s^{-1} to $\sim10^{-15}$ cm^2 s^{-1}.[209,210] For the SOA particles with size ∼0.7–1.1 μm, according to Eq. 2.7, the e–folding time of equilibration, i.e., the time after which the concentration in the particle core deviates by less than a factor of 1/e from the equilibrium value, would be more than 1 hour, and up to few days, at temperatures between 230 and 250 K. $D_{\mathrm{H_2O}}$ could be less than 10^{-17} cm^2 s^{-1} at 200 K[209,210] resulting in a much longer e–folding time of equilibration. Under our experimental time scale (∼40 min) and change rates in RH (∼ 1–2%/min), the complete deliquescence of amorphous solid SOA particles can be ruled out. Thus, SOA particles with an aqueous shell and a solid core could form and serve as IN and induce immersion freezing.

So far only two studies have investigated the ice nucleation efficiency of SOA particles[11,171]. Möhler et al.[11] showed that at 205 K the coating of SOA

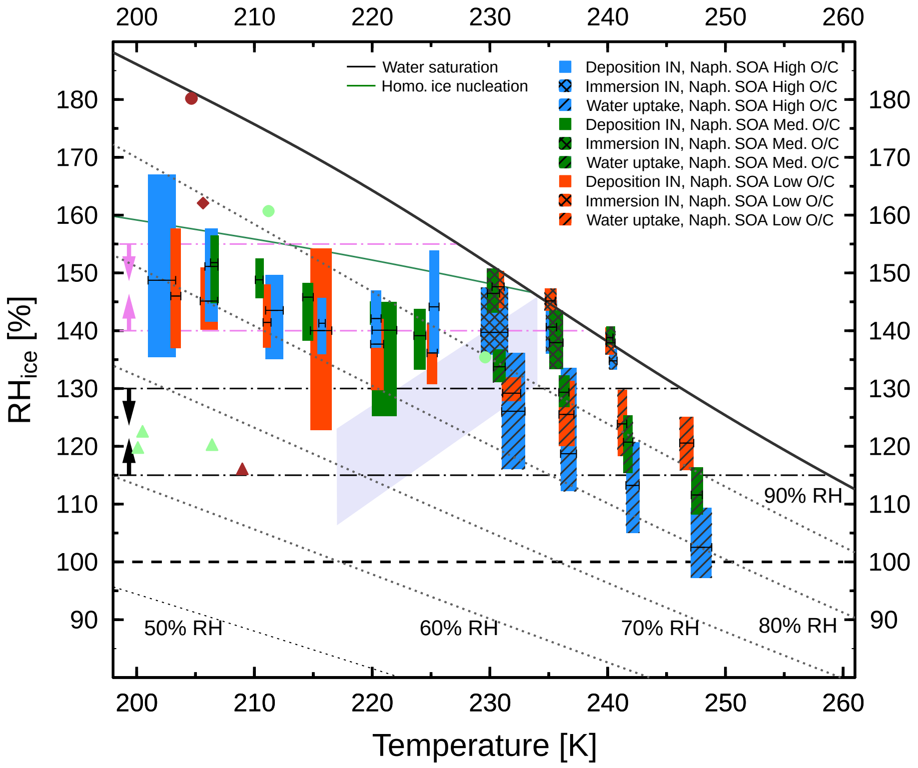

Figure 6.1: Experimentally determined range of onset conditions for ice nucleation and water uptake by SOA particles with high (1.0), medium (0.54), and low (0.27) O/C ratio indicated by the blue, green, and red bars, respectively. Corresponding shaded and hatched bars represent conditions of water uptake and immersion freezing, respectively. The horizontal solid lines within the bars indicate the mean onset values. Ice nucleation data from previous studies of SOA coated Arizona test dust (brown triangle), SOA coated illite (brown diamond), and pure SOA (brown circle) by Möhler et al.[11] and glassy (light green triangles) and liquid (light green circles) citric acid particles by Murray et al.[46] are shown. The green line indicates the homogeneous freezing limit adapted from Koop et al.[33]. Light gray shaded area indicates bounds of continental cirrus formation from Heymsfield and Miloshevich[16]. The RH_{ice} ranges between horizontal paired lines with corresponding arrows indicate the lower limits for cirrus formation conditions in northern (black dash-dotted lines) and southern hemisphere (pink dash-dotted lines) from Ström et al.[17] and Haag et al.[18].The remaining lines are identical to those in Fig. 4.3.

stemming from the reaction of α–pinene with O_3 suppressed ice nucleation of mineral dust and that pure SOA particles are not efficient IN as shown in Fig. 6.1. This is in contrast to the amorphous SOA particles investigated in this study. The reason is not clear. One possible reason may be that the SOA particles generated from different precursor gases and oxidants adopt different phase states[19,130]. Prenni et al.[171] investigated the ice nucleation of SOA particles generated by the ozonolysis of VOCs mixtures. Prenni et al.[171] did not observed ice nucleation in detectable quantities at 243 K and 100% RH. This result agrees with our data showing the SOA particles did not nucleate ice above 242 K. Only one study has investigated the ice nucleation efficiency of an amorphous solid organic particle under conditions of the upper troposphere[46]. In that study, Murray et al.[46] showed that glassy citric acid particles at temperatures below 212 K can nucleate ice via deposition mode. But at temperatures above 212 K, the citric acid particles adopted a liquid state and nucleated ice homogeneously as shown in Fig. 6.1[46].

Koop et al.[19] suggest that the glass transition temperature (T_g) for SOA material is at ∼230 K and 70–95% RH as shown in Fig. 2.3. Since the investigated SOA particles are in an amorphous semi-solid state at room temperature, the particles may transfer to a solid (i.e., glassy) state at lower temperatures due to an increase in viscosity when temperature decreases[19,209]. Under the experimental time scales in this study, this solid state of particles hinders the water uptake by particles and thus formation of aqueous film on the particles due to the extremely low $D_{\mathrm{H_2O}}$ at temperatures below 230 K. This would explain that SOA particles nucleate ice preferentially via deposition mode instead of undergoing water uptake and then deliquescence. The mean RH_{ice} values for deposition ice nucleation are about 10–15% lower than the homogeneous ice nucleation limit[33]. Thus, the heterogeneous ice nucleation from the presence of amorphous semi–solid or solid SOA particles in the upper troposphere can compete with homogeneous ice nucleation from aqueous droplets for cirrus cloud formation.

The efficiency of heterogeneous ice nucleation is commonly assumed to depend on active sites which can be associated with defects, cracks, cavities, and chemical and physical bonds allowing enhanced interaction with water vapor[20]. The number of these morphological irregularities on the particle surface which initiate ice nucleation, for instance through a “negative Kelvin effect”, i.e. a decrease in the ice vapor pressure due to a concave curvature of entrained water or ice within a cavity, may result in different ice nucleation efficiencies[20]. If deposition ice nucleation is mainly governed by surface morphology (this has to be investigated), the solid particle surfaces may provide sufficient active sites to induce ice nucleation. This would explain why the SOA particles investigated here can induce deposition ice nucleation at RH_{ice} well below the homogeneous ice nucleation limit[33].

As discussed in Chapter 2, Koop et al.[19] suggest that the T_g of SOA compounds more strongly depends on molecular mass than on O/C ratio. For this reason, one may argue that the investigated particles, despite having different O/C ratios, may have similar viscosities and thus a similar phase or morphology. The observed similar deposition ice nucleation efficiencies for the SOA particles with different O/C ratio might be explained by the particles' similar amorphous phases. The bulk atomic O/C ratio may have only a minor impact on deposition ice nucleation efficiency and that lies within the experimental uncertainty. Thus, for these reasons, ice nucleation results would show no significant difference in RH_{ice} ice nucleation onsets .

6.3 Ice Nucleation Analysis of SOA Particles

The experimentally obtained deposition ice nucleation onsets are used to to derive $J_{\text{het}}(T)$, $K(T)$, θ, and IN activated fraction for laboratory-generated amorphous SOA particles based on the the same methods described in previous Chapters.

6.3.1 J_{het} and K for SOA Particles

Experimentally derived $J_{\text{het}}(T)$ and $K(T)$ values for deposition ice nucleation for the investigated laboratory-generated amorphous SOA particles are presented in Fig. 6.2. J_{het} values are a strong function of temperature and increase exponentially by ~2 orders of magnitude as shown in Fig. 6.2. The particles with high O/C exhibit slightly higher J_{het} values than those of particles with medium and low O/C ratios at the same temperatures. The total surface area of SOA particle samples with high O/C ratio available for ice nucleation is ~3–5 times less then those of particle samples with medium and low O/C ratio as shown in Table 6.1. It would be expected from CNT that particles with a lower surface area require higher RH_{ice} to nucleate ice. This, in turn, would indicate that the investigated SOA particle samples with high O/C ratio would have a sightly higher ice nucleation efficiency, although the mean ice nucleation onset RH_{ice} was not significantly different within the experimental uncertainty. The derived $K(T)$ also demonstrates a strong temperature dependence for all the particle samples as shown in Fig. 6.2. $K(T)$ increases by ~1–2 orders of magnitude within a few degrees Kelvin.

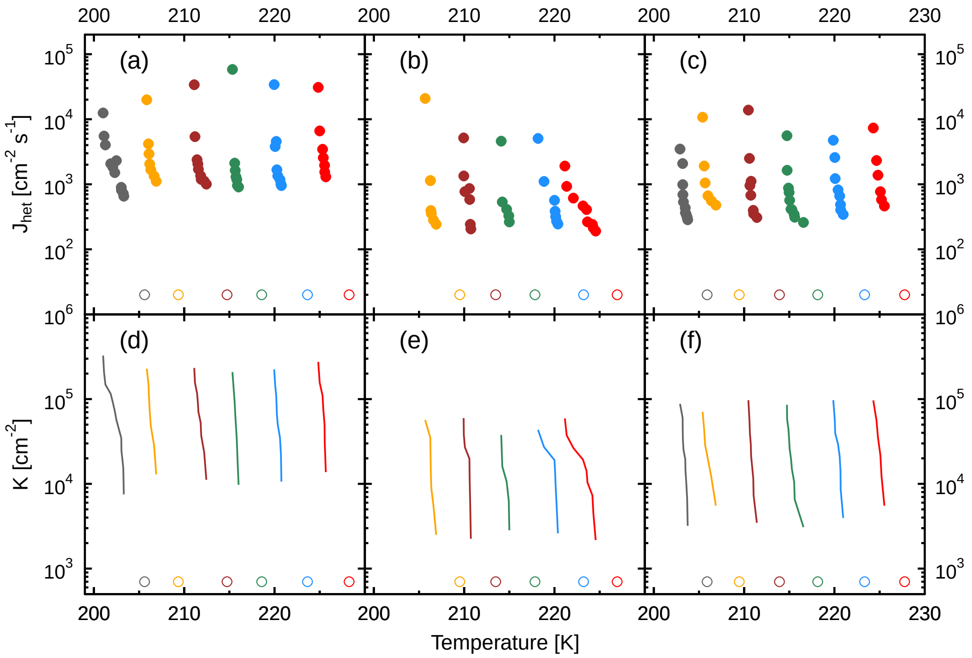

Figure 6.2: Experimentally derived $J_{\text{het}}(T)$ and $K(T)$ for deposition ice nucleation by laboratory–generated amorphous SOA particles. J_{het} values are given for particle samples with (a) high (1.0), (b) medium (0.54), and (c) low (0.27) O/C ratio. $K(T)$ are given for particle samples with (d) high (1.0), (e) medium (0.54), and (f) low (0.27) O/C ratio. Individual colors represent experiments conducted at the same starting temperature at which $RH_{\text{ice}} = 100\%$. The open symbols represent corresponding starting temperatures.

6.3.2 IN Activated Fraction

The ranges of IN activated fractions for the SOA particles at the investigated temperatures are presented in Table 6.1. Only a small fraction of the particles is activated resulting in IN activated fractions from 0.3×10^{-4} to 6.7×10^{-4}. As mentioned above, the substrate based optical microscope technique used here is sensitive to each individual ice nucleation event. The IN activated fraction reported here is mainly defined by the total number of deposited particles available for ice nucleation. The total number of particles deposited on the substrate is determined by an optical microscope and a large number of small particles may not be detected due to the limited resolution of the optical microscope. Thus, the IN activated fractions reported here for the investigated SOA particles have to be interpreted as upper limits compared to other studies.

6.3.3 Contact Angle of SOA Particles

The mean θ values for the investigated SOA particles as a function of temperature and RH_{ice} are shown in Fig. 6.3a and b, respectively. The investigated particle samples possess mean θ values ranging from ~25.5° to 27.9° for deposition ice nucleation. Within the investigated temperature range, all the investigated particle samples exhibit similar mean θ values within the experimental uncertainties. The mean θ values for the unexposed and O_3-exposed SRFA particles are also shown in Fig. 6.3. The SOA particles have very similar mean θ values compared to both unexposed and O_3–exposed SRFA particles with mean θ values of 24.5–27.5° at temperatures between 230 and 220 K. This indicates that the SOA particles and unexposed and O_3-exposed SRFA particles have similar ice nucleation efficiency which also can be seen when comparing the ice nucleation onset RH_{ice} as shown in Figs. 6.1 and 4.4.

Figure 5.12b shows the mean θ values as a function of onset RH_{ice} for SOA particles and various organic and inorganic particle types which have been presented in Fig. 4.6. Figure 5.12b also shows the proposed parameterization of θ given in Chapter 4. As shown in Fig. 5.12b, θ values for the laboratory–generated amorphous SOA particles with O/C ratio ranging from 0.27 to 1.0 agree well with the proposed parameterization within the experimental uncertainties.

6.4 Glass Transition Temperature of Amorphous Organic Particles

6.4.1 Approach to Derive Glass Transition Temperature

As discussed in Chapter 2, the glass transition temperature (T_g) of aerosol particles can be used as a representative temperature to determine the state of organic particles which is strongly affected by the particle's water content and environmental RH. In this section, the upper limit of T_g as a function of RH for the investigated SOA particles is determined based on the theoretical description of T_g shown in Chapter 2.

To predict T_g of an organic particle as a function of RH, according to Eq. 2.10, three parameters are required. The first two are k_{gt} and $T_g(dry)$. The third one is the ratio of the mass fractions of organic material and water (w_{org} and w_w, $w_w + w_{org} = 1$). At equilibrium conditions, RH equals a_w. ρ_w and M_w represent density and molecular weight of water. Also, the ratio of w_{org}

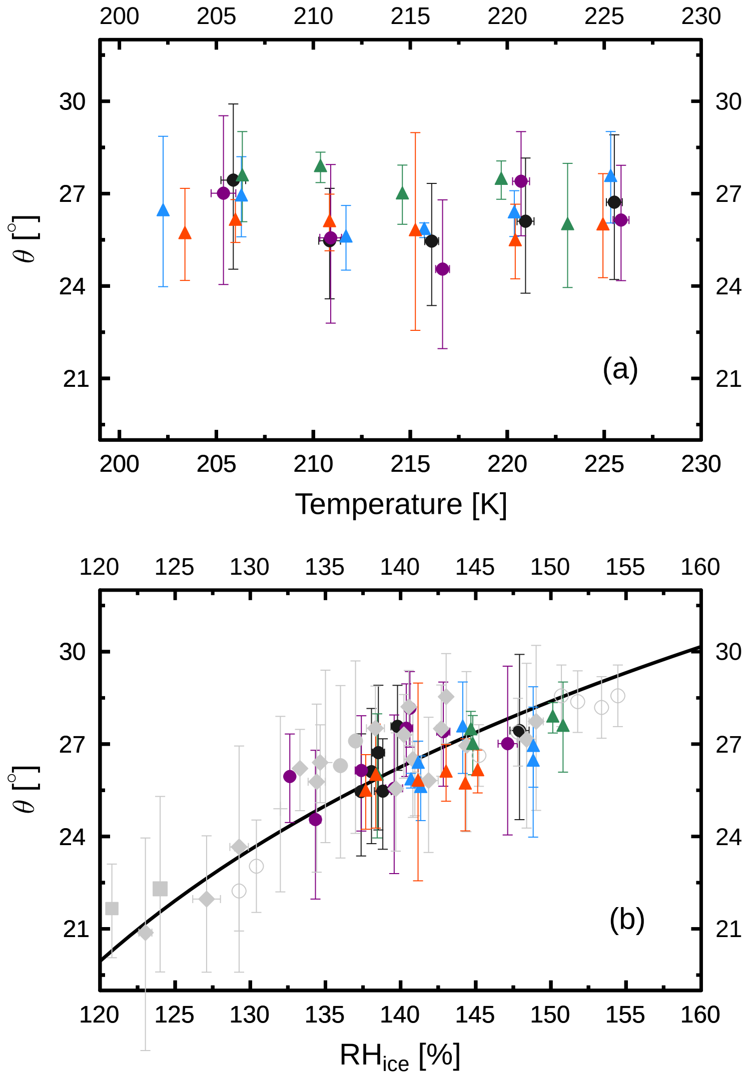

Figure 6.3: The mean values of contact angles, θ, for deposition ice nucleation induced by SOA particles (a) as a function of temperature and (b) as a function of RH_{ice}. Blue, green, and red triangles represent the SOA particles with high, medium, and low O/C ratio, respectively. Black and purple circles represent the unexposed and O_3–exposed SRFA particles, respectively. The solid line represents the parameterization of θ as a function of RH_{ice} and gray symbols represent θ values for various particle types as shown in Fig. 4.6.

and w_w can be described as follows:

$$\frac{w_{org}}{w_w} = \frac{M_{org}}{M_w}\frac{n_{org}}{n_w}\,, \tag{6.1}$$

where M is molar mass, and n is the number of moles of water or organic in the particle; the indices w and org refer to water and the organic solute, respectively. Thus, the third parameter can be either obtained from i_{org} and M_{org} according to Eq. 2.8 or from κ_{org} and ρ_{org} according to Eq. 2.9.

Because SOA particles can not be described as a pure compound, but rather as a mixture of compounds with different molecular weights, it is difficult to obtain a single molecular weight to represent these two type of compounds. Thus, we use the measured κ_{org} and ρ_{org} values to derive the third parameter. According to Eq. 2.9, the ratio of w_{org} and w_w can be derived as a function of RH or a_w as follows:

$$\frac{w_{org}}{w_w} = f(RH) = \frac{100 - RH}{RH}\frac{1}{\kappa_{org}}\frac{\rho_{org}}{\rho_w}\,. \tag{6.2}$$

According to Eq. 2.10 and Eq. 6.2, T_g of an organic particle as a function of RH can be derived as follows:

$$T_g(RH) = \frac{k_{gt}T_{g,w} + f(RH)T_g(dry)}{k_{gt} + f(RH)}\,, \tag{6.3}$$

where $T_{g,w}$ is 136 K for pure water[276].

6.4.2 Prediction of the Upper Limit of T_g for Amorphous SOA Particles

Using Eqs. 6.2 and 6.3, the upper limit of T_g for SOA particles as a function of RH is predicted using the experimental derived parameters which are summarized in Table 6.2. The effective density (ρ_{org}) for the SOA particles is derived from the AMS vacuum aerodynamic diameter and the SMPS mobility diameter measured during particle collection. κ_{org} is derived from the CCN activities measured during particle collection. k_{gt} of 1.5 is used for all SOA particles which is the lower bound of k_{gt} as suggested by Koop et al.[19]. Thus, the present estimate of T_g should be considered as an upper limit.

Currently, $T_g(dry)$ values for SOA particles are not available[19,205]. At 298 K and 35% RH, the SOA particles adopt an amorphous semi–solid and most likely solid state because of the measured bounce factor of 0.6±0.2 as discussed above. Thus, T_g of 298 K at 35% RH is used as a constraint and

Table 6.2: The values of ρ_{org}, κ_{org}, k_{gt}, and $T_g(dry)$ used to predict the the upper limit of $T_g(RH)$ for SRFA and SOA particles are presented. The corresponding atomic O/C ratios are also listed.

Sample	O/C Ratio	ρ_{org} (g/cm^3)	κ_{org}	k_{gt}	$T_g(dry)$ K
High O/C	1.0	1.70	0.217	1.5	315
Medium O/C	0.54	1.65	0.235	1.5	317
Low O/C	0.27	1.70	0.143	1.5	309

$T_g(w)$ (i.e., 136 K at 100% RH for pure water) to predict the upper limit of $T_g(RH)$ for SOA particles using measured ρ_{org}, κ_{org}, and an assumption of k_{gt} values according to Eqs. 6.2 and 6.3.

First, ρ_{org} and κ_{org} are used to derive $f(35\%)$ according to Eq. 6.2. Then, $T_g(35\%)$ at 298 K, $f(35\%)$, and k_{gt} of 1.5 are used to estimate $T_g(dry)$ from Eq. 6.3. This procedure yields $T_g(dry)$ of ∼315, 317, and 309 K for the SOA particles with high, medium, and low O/C ratio, respectively. Finally, the $T_g(dry)$ values are used to derive the upper limit of T_g for the investigated SOA particles as a function of RH as shown in Fig. 6.4.

For example, the predicted upper limit of $T_g(RH)$ for the SOA particles with low O/C ratio is shown as the red solid line which indicates that below this line the SOA particles most likely adopt a solid (i.e., glassy) state. The range of onset conditions for deposition ice nucleation and water uptake by SOA particles as a function of RH converted from the data presented in Fig. 6.1 are also shown. In case of SOA particles with low O/C ratio, at temperatures below the predicted upper limit of T_g (red line), all the ice nucleation events occurred via deposition mode (open circles). At temperatures and RH conditions above the upper limit of T_g, for most of cases, water uptake was observed indicating that the humidity–induced glass transition of the SOA particles most likely occurred upon increasing RH. As shown in Fig. 6.4, the predicted upper limits of T_g for SOA particles increases with increasing κ_{org} values. For example, the predicted upper limit of T_g for SOA particles with low O/C ratio (κ_{org} of 0.143) is much higher than those of particles with high (κ_{org} of 0.217) and medium (κ_{org} of 0.235) O/C ratios.

For SOA particles with high and medium O/C ratio, water uptake also occurred above the corresponding predicted upper limits of T_g for most of the cases. Again, water uptake was observed indicating that the humidity–induced glass transition most likely occurred on the SOA particles upon increasing RH. At temperatures below the predicted upper limit of T_g, the majority of ice nucleation events from particles with medium and high O/C ratio occurred

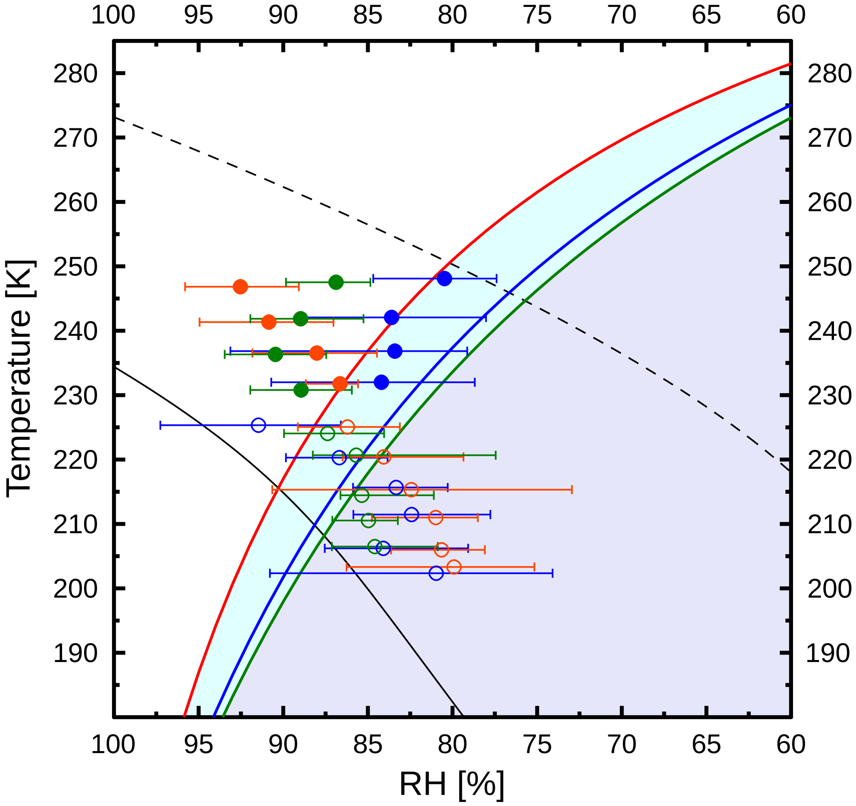

Figure 6.4: The range of predicted upper limit of T_g for SOA particles as a function of RH (light cyan area). The onset conditions for deposition ice nucleation and water uptake by SOA particles as a function of RH converted from the data presented in Fig. 6.1 are shown. The mean values of deposition ice nucleation and water uptake onsets for SOA particles with high (1.0), medium (0.54), and low (0.27) O/C ratio are indicated by the open and solid blue, green, and red circles, respectively. The error bars represent the range of the observed onset conditions. The blue, green, red lines represent the predicted upper limit of $T_g(RH)$ for SOA particles with high, medium, and low O/C ratio, respectively. The dashed and solid black lines represent the ice melting curve and the predicted homogeneous freezing curve, respectively adapted from Koop et al.[33] and Koop and Zobrist[52].

via deposition mode. But also some deposition ice nucleation events from particles with medium and high O/C ratio occur at temperatures of 220 and 225 K which is above the T_g at corresponding RH. One possible reason could be that the T_g values are underestimated because the assumption of k_{gt} of 1.5 may be to high for particles with medium and high O/C ratio. Zobrist et al.[180] have shown that some organic compounds with low molecular weight exhibit k_{gt} smaller than 1.0. Thus, k_{gt} of 1.5 may be an overestimation for SOA particles with medium and high O/C ratio because of the presence of organics with low molecular weight in these two types of SOA particles. As for SOA particles with low O/C ratio, k_{gt} of 1.5 would be a reasonable assumption. Another explanation may be that at these low temperatures, the diffusion of water molecules into SOA particles is slow so that an ice germ forms at RH_{ice} values above 130% before the formation of a liquid film on the particle surface.

As shown in Fig. 6.4, water uptake indicating the humidity–induced glass transition by the SOA particles occurred close to or above the corresponding predicted upper limits of T_g for most of the cases. Thus, we propose that the range of the predicted upper limits of T_g for SOA particles (light cyan area showing in Fig. 6.4) could be used as an estimate of T_g as a function of RH for organic aerosol particles or organic materials resembling similar chemical composition, density, and hygroscopicity as SOA particles investigated in this study.

6.5 Amorphous SOA Particles and Field Collected Organic–Dominated Particles

Figure 6.5 shows the comparison of onset conditions of ice nucleation and water uptake by laboratory–generated SOA particles and field–collected anthropogenically impacted particles collected during the CalNex campaign. Below 230 K, the anthropogenic–impacted particles (A2, A3, and A4) exhibit remarkably similar ice nucleation efficiencies compared to those of laboratory–generated SOA particles. This indicates that the organic–dominated particles collected during the CalNex campaign may also adopt an amorphous solid state with a morphology similar to the investigated amorphous solid SOA particles. Thus these particles exhibit similar deposition ice nucleation efficiency. Above 230 K, water uptake occurred at similar RH values compared to the laboratory–generated SOA particles with high (1.0) and medium (0.54) O/C ratios. After water uptake, the anthropogenically impacted particles nucleated ice more efficiently than laboratory–generated SOA particles indicating that most likely the insoluble inclusions become efficient IN.

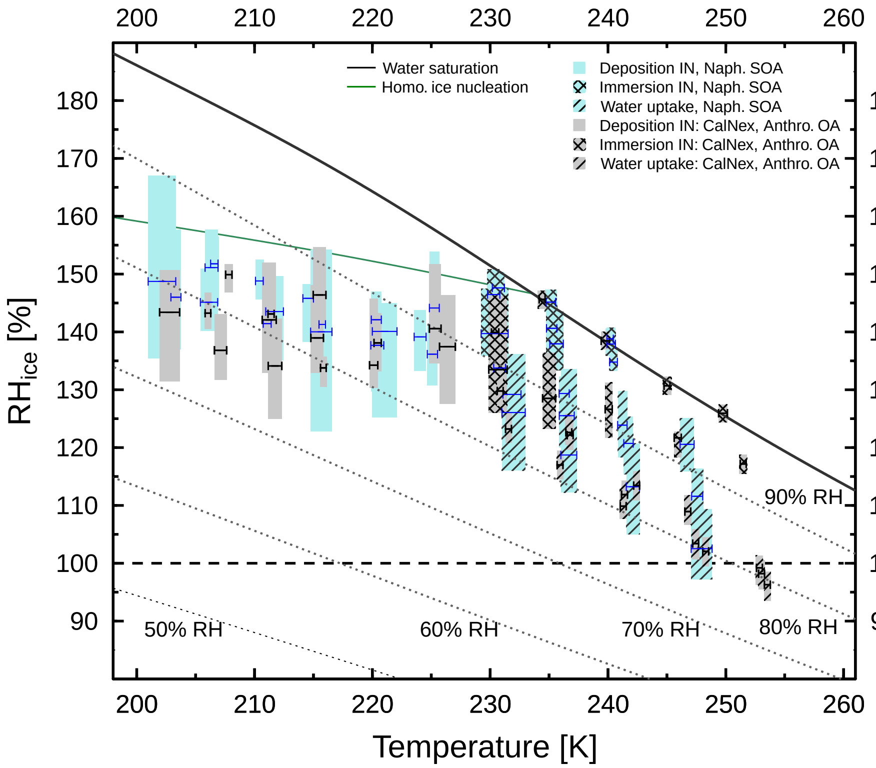

Figure 6.5: The range of onset conditions of ice nucleation and water uptake by laboratory-generated SOA particles (light green bars) and field-collected anthropogenic-impacted particles (A2, A3, and A4) during the CalNex campaign (gray bars). The corresponding shaded and hatched bars represent conditions of water uptake and immersion freezing, respectively. The remaining lines are identical to those in Fig. 5.8

Figure 6.6 shows the comparison of onset conditions of ice nucleation and water uptake by laboratory–generated SOA particles and field–collected organic–dominated particles with SOA coating collected during the MILAGRO campaign. Below 230 K, in general, the organic–dominated particles exhibit higher ice nucleation efficiencies compared to those of laboratory–generated SOA particles. Above 230 K, water uptake also occurred at similar *RH* values compared to the laboratory-generated SOA particles with high and medium O/C ratios. The discussion of the phase state of SOA particles suggests that the SOA dominated MILAGRO organic particles are in a glassy state at low temperatures similar to the laboratory-generated SOA particles. However, the solid inclusions of the field-collected particles may render the surface structure of overlying SOA particles more efficient IN. After water uptake, the field-collected organic–dominated particles exhibit similar immersion freezing

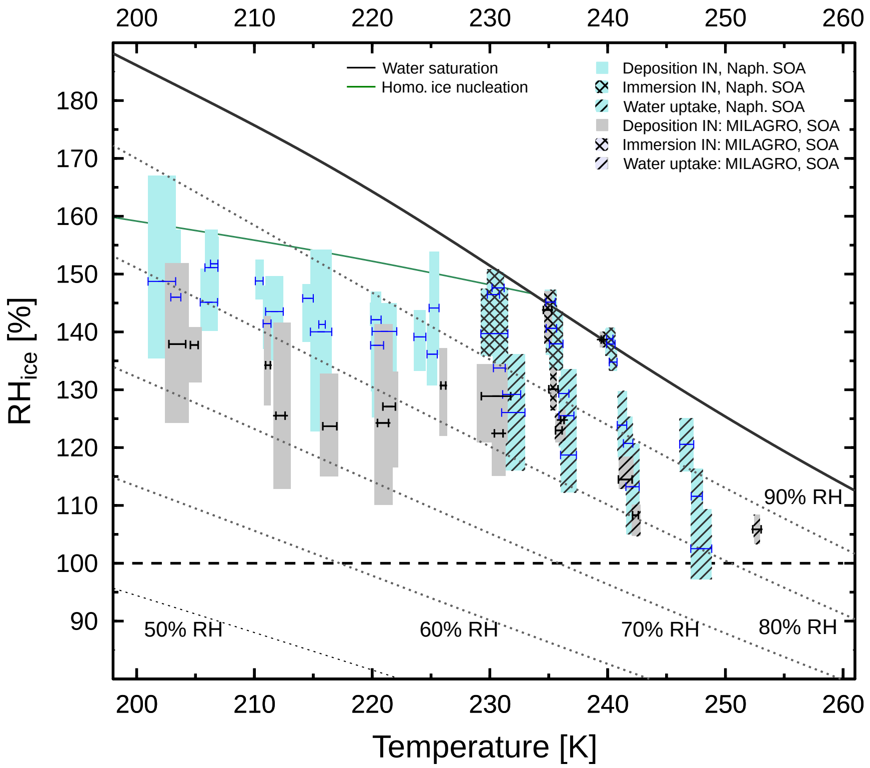

Figure 6.6: The range of onset conditions of ice nucleation and water uptake by laboratory-generated SOA particles (light green bars) and field-collected organic-dominated particles (T0, T1, and T2) during the MILAGRO campaign (gray bars). The corresponding shaded and hatched bars represent conditions of water uptake and immersion freezing, respectively. The remaining lines are identical to those in Fig. 5.8

efficiencies compared to the laboratory–generated SOA particles.

Figure 6.7 shows the onset conditions for deposition ice nucleation and water uptake by MILAGRO organic–dominated particles as a function of *RH* along with the range of the proposed upper limits of T_g for SOA particles as shown in Fig. 6.4. Water uptake (blue solid circles) by the organic–dominated particles collected at the T1 and T2 sampling sites occurred above the predicted upper limit of T_g (red line). The majority of deposition ice nucleation events occurred below this upper limit of T_g. As discussed in Chapter 5, the particles collected at the T1 and T2 sampling sites were significantly coated with secondary organic material due to the photochemical formation and processing of SOA[22,23,219]. This indicates that the SOA coating on these particles most likely adopted an amorphous solid state and nucleated ice at temperatures and *RH* conditions below the predicted upper limit of T_g. As for the particles collected at the T0 sampling site, all the water uptake occurred above the lower predicted upper limit of T_g. In general, it can be concluded that the proposed upper limits of T_g predicted from laboratory–generated SOA particles could serve as estimates of T_g as a function of RH for anthropogenic SOA materials.

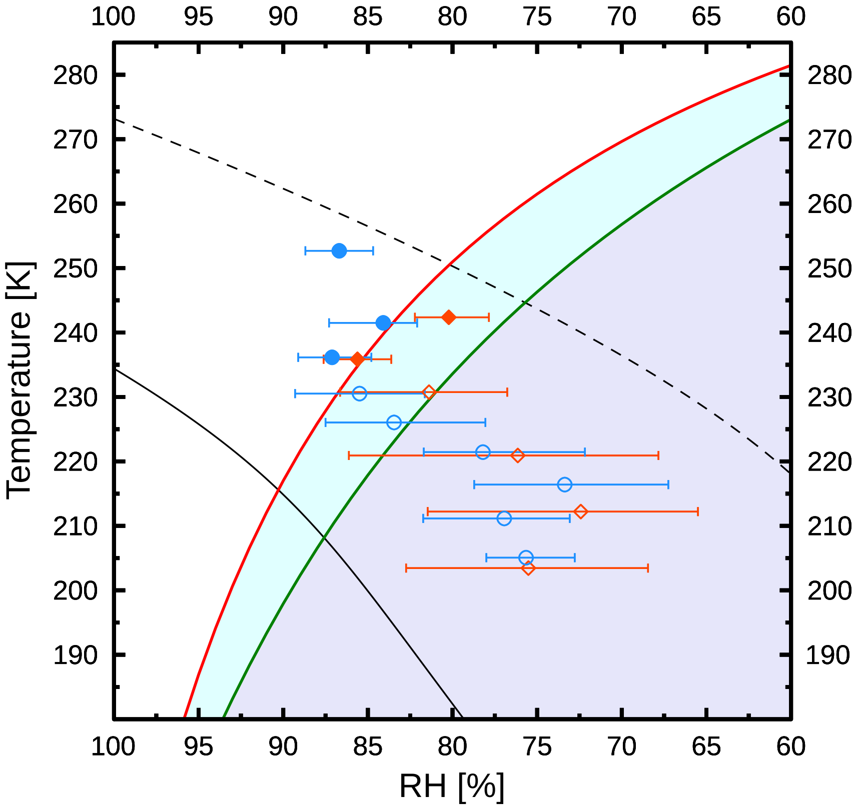

Figure 6.7: The onset conditions for deposition ice nucleation and water uptake by MILAGRO organic-dominated particles as a function of RH converted from the data presented in Fig. 5.3. The mean values of deposition ice nucleation (open) and water uptake (solid) onsets for MILAGRO organic-dominated particles collected at the T0 and T1/T2 sites are indicated by diamonds and circles, respectively. The error bars represent the range of the observed onset conditions. The remaining lines and colors are identical to those in Fig. 6.4

6.6 Conclusions

The investigated amorphous SOA particles with O/C ratio of 0.27–1.0 generated from the oxidation of naphthalene with OH radicals and O_3 demonstrate the potential to act as deposition IN at temperatures below 230 K and below the homogeneous freezing limit. Water uptake is observed above 230 K followed by immersion freezing in some cases at temperatures between 230 and 245 K. The bulk atomic oxygen–to–carbon (O/C) ratio of these SOA particles does not show a significant effect on deposition ice nucleation within the experimental uncertainty but does depend on water uptake. Above 230 K particles with higher O/C ratio take up water at lower RH than particles with low O/C ratio.

The investigated SOA particles exhibit a bounce factor of 0.6±0.2 which was determined at room temperature and ~35% RH. Under these conditions, these SOA particles adopt an amorphous semi–solid and probably an amorphous solid state. These SOA particles can be present in a solid state and nucleate ice via deposition mode below 230 K whereas they adopt a semi–solid state with lower viscosity at higher temperatures and take up water. Thus, phase state and viscosity affect the interaction of SOA particles with water vapor. This is further confirmed by the analysis of the glass transition temperatures as a function of RH for SOA particles which shows that most of the water uptake occurred near or above the glass transition temperatures.

The mean RH_{ice} values of deposition ice nucleation by the investigated SOA particles are about 10–15% lower than the homogeneous ice nucleation limit[33] similar to SH cirrus onsets. When present in sufficient number concentration and low updraft velocities, these amorphous solid SOA particles could induce cirrus cloud formation and thus inhibit subsequent homogeneous ice nucleation. Amorphous SOA particles also show the ability to nucleate ice via immersion freezing, in part, at water subsaturated conditions, at temperatures between 230 and 242 K. Thus, amorphous SOA particles could affect mixed–phase cloud formation. The change rate of RH may govern the size of the solid core or thickness of the liquid shell and thus yields different immersion freezing efficiencies. For example, upon a slow change rate of RH, corresponding to a slow updraft, amorphous solid particles would have a longer time to take up water and become liquid droplets, and thus nucleate ice homogeneously instead of undergoing immersion freezing.

The upper limits of the glass transition temperature (T_g) as a function of RH for the amorphous SOA particles are derived based on the theoretical frame work proposed by Koop et al.[19] using the observed values of parameters including ρ_{org}, κ_{org}, and $T_g(dry)$ and an assumption of k_{gt}. The upper limit of $T_g(RH)$ for SOA particles provides possible explanations for the observed different heterogeneous ice nucleation pathways and water uptake. A range of the upper limits of $T_g(RH)$ is proposed for organic aerosol particles or organic materials resembling similar chemical composition, density, and hygroscopicity as SOA particles investigated in this study. Although the predicted $T_g(RH)$ may explain the measured ice nucleation and water uptake by amorphous SOA particles, significant uncertainties in predicted $T_g(RH)$ remain, mainly due to a lack of data for the required parameters, such as $T_g(dry)$ and k_{gt}. Clearly, more investigations are needed to obtain sufficient data for advancing the understanding of the interaction between organic particles and water vapor and thus cloud formation processes.

Chapter 7

Conclusions and Outlook

7.1 Summary and Conclusions

The overall goal of this thesis is to improve scientific understanding of heterogeneous ice nucleation by ubiquitous atmospheric organic particles. This thesis presents the laboratory study of heterogeneous ice nucleation and water uptake by various types of laboratory–generated and field–collected organic and organic–containing particles for temperatures and relative humidity (RH) typical of the troposphere and lower stratosphere. This was achieved by using a custom-built optical microscopy-based ice nucleation system. In addition, complementary techniques were used for single particle analysis, including computer controlled scanning electron microscopy with energy dispersive analysis of X–rays (CCSEM/EDX) and scanning transmission X–ray microscopy with near edge X–ray absorption fine structure spectroscopy (STXM/NEXAFS). The main conclusions from this thesis are summarized as follow.

Heterogeneous Ice Nucleation and Water Uptake by Laboratory–Generated HULIS particles

This study investigated the heterogeneous ice nucleation and water uptake by laboratory–generated Suwannee river standard fulvic acid (SRFA) and Leonardite standard humic acid (Leonardite) particles serving as surrogates of HULIS typically found in atmospheric particles and the effect of particle oxidation by O_3 on corresponding IN efficiencies. Validation of the experimental method was performed by determining the ice nucleation onsets of Kaolinite particles which are known to be efficient IN. The results show that SRFA, Leonardite and corresponding O_3–exposed particles can nucleate ice via deposition mode and immersion freezing at atmospheric relevant conditions. Oxidation of Leonardite and SRFA particles by O_3 led to a decrease in deposition nucleation efficiency and to water uptake at lower temperatures for the former and to an increase in the lowest temperature at which deposition nucleation was observed for the latter. These results suggest that there is not a clear relationship between particle hydrophilicity and ice nucleation efficiency, and thus other factors may also govern the nucleation process.

Heterogeneous Ice Nucleation and Water Uptake by Field–Collected Particles

Different types of anthropogenically and marine-impacted particles collected within and around the urban environments of Los Angeles and Mexico City were investigated for their potential to nucleate ice. The particle's ice nucleation efficiency is related to the chemical composition determined by single particle analyses using CCSEM/EDX and STXM/NEXAFS. The results demonstrate that all the investigated particles with various chemical and physical properties exhibit distinctly different ice nucleation efficiencies and can serve as efficient IN at atmospheric conditions typical for cirrus and mixed phase cloud formation. The chemical composition was found to play a crucial role in determining water uptake and immersion freezing but was less important for deposition nucleation. The observed ice nucleation onsets observed by these field–collected particles are in stark contrast to previous ice nucleation data from laboratory–generated organic particles. This indicates that current laboratory proxies of organic particles are not sufficiently representative to infer heterogeneous ice nucleation by complex atmospheric organic particles. The results demonstrate that the novel combination of optical microscopy based ice nucleation studies with micro-spectroscopy analyses provides an insightful tool to infer ice nucleation properties of atmospheric aerosol particles.

Heterogeneous Ice Nucleation and Water Uptake by Laboratory–Generated Amorphous SOA Particles

Heterogeneous ice nucleation and water uptake by laboratory–generated amorphous SOA particles with oxygen–to–carbon (O/C) ratio of 0.27–1.0 from the oxidation of naphthalene with OH radicals and O_3 serving as surrogates of anthropogenic SOA were investigated. The SOA particles demonstrate the potential to act as deposition IN at temperatures below 230 K and at RH below the homogeneous freezing limit. Water uptake was observed above 230 K followed by immersion freezing at temperatures between 230 and 242 K. The bulk atomic O/C ratio of these SOA particles did not show a significant effect on deposition ice nucleation. However, the O/C ratio did affect water uptake.

Above 230 K particles with higher O/C ratio took up water at lower RH than particles with low O/C ratio. The results indicate that these SOA particles may form a solid (i.e., glassy) state and nucleate ice via deposition mode below 230 K whereas they adopt a semi-solid state with lower viscosity at higher temperatures and take up water. The results show that the phase state and viscosity affect the interaction of SOA particles with water vapor.

The experimentally derived ice nucleation data for all the investigated particles were analyzed using both classical nucleation theory (CNT) and the singular hypothesis approach (SH) providing heterogeneous ice nucleation rate coefficients (J_{het}) and cumulative IN spectra (K), respectively, allowing either approach to be implemented in cloud resolving models. J_{het} and K for all investigated Kaolinite, HULIS, field-collected, and SOA particles were a strong function of temperature and increased exponentially by 2∼3 orders of magnitude within less than 3 K. J_{het} was applied to derive the contact angle (θ) using CNT. A new parameterization for deposition ice nucleation was derived from experimentally derived θ. Two back–of–the envelope calculations show that the proposed parameterization and correspondingly derived heterogeneous ice nucleation rate coefficients can be useful in applications such as cloud system resolving models but also for post analysis of field observations to describe the evolution of the ice phase. The IN activated fraction for all the investigated particles is also provided and should be interpreted as lower limits due to the applied technique. The ice nucleation onsets for the different particle types investigated here coincide with the observed conditions for cirrus cloud formation. Although the investigated particles types exhibit different ice nucleation efficiencies via deposition mode and immersion freezing at different temperature and RH conditions, the results suggest that that these laboratory-generated and field-collected organic or organic-containing particles can play important roles in both cirrus and mixed-phase cloud formation. Thus, the potential role of these organic-containing particles on atmospheric ice crystal formation should be considered in cloud and climate modeling studies.

To instigate the phase state of organic particles at different atmospherically relevant conditions, the upper limits of glass transition temperature (T_g) as a function of RH for the amorphous SOA particles were estimated based on the theoretical frame work proposed by Koop et al.[19]. The upper limit of the $T_g(RH)$ for SOA particles provides possible explanations for the observed different heterogeneous ice nucleation pathways and water uptake. Below the upper limit of $T_g(RH)$, particles most likely will adopt a solid state in which water uptake will be hindered and deposition ice nucleation is preferred. Most of the observed deposition ice nucleation events from SOA particles indeed occurred below the predicted upper limits of $T_g(RH)$. A range of the upper limits of $T_g(RH)$ is proposed for organic aerosol particles or organic materials resembling similar chemical composition, density, and hygroscopicity as the SOA particles investigated in this study.

7.2 Outlook

The current understanding of the interactions between aerosol particles and water vapor leading to the formation of ice crystals is not sufficient resulting in large uncertainties in predicting future climate. The results presented in this study raise a number of topics and questions to be investigated to improve our understanding of aerosol particles and water vapor interactions

- Will chemical aging by heterogeneous oxidation change the ice nucleation efficiency of organic particles and if yes, to what extend? Up to now, only a few studies have investigated the effects of atmospheric oxidation by O_3 of organic particles on ice nucleation[3,174]. How will the oxidation by OH radicals and NO_3 affect the ice nucleation efficiency of organic particles? OH oxidation is know to lead to volatilization of organic particles[162,164] and NO_3 is an efficient oxidant in polluted environments during nighttime[56,57,161] leading potentially to condensed phase nitrate groups. Oxidation by OH and NO_3 may change the surface microstructure and chemical composition of organic particles and thus change the particle's ice nucleation efficiency.

- The discrepancy in the ice nucleation efficiency between the laboratory-generated and field-collected organic-containing particles has to be resolved for better representation of IN in modeling studies. Complementary and sophisticated single particle analysis and ice nucleation experiments on the same atmospheric particles may be able to provide sufficient information to close the gap.

- Although an increasingly better understanding of the the chemical composition of SOA particles is being achieved, the efficiency of SOA particles serving as IN is poorly understood. Thus, the role of SOA particles in cloud formation at temperatures below ice melting temperature should be further investigated. The glass transition of organic particles should be further investigated since this affects their cloud formation ability.

- The results from previous studies and this study indicate that various particles' properties such as surface morphology and chemical composition may control the heterogenous ice nucleation mechanisms of particles. But what really governs heterogenous ice nucleation, i.e. the active site, is not well known. Also how the heterogeneous ice nucleation should be described, i.e. as a stochastic or deterministic process, is not clear yet. One promising approach to advance our understanding on these fundamental mechanisms would be to identify, at a molecular level, the active site on the particle surface for ice nucleation . Currently, no analytical technique can achieve this goal. Thus, the development of novel analytical techniques capable of observation of ice nucleation at the microscopic level of individual particles is needed to examine ice nucleation and to investigate the effects of chemical composition and morphological features on the ice nucleation efficiency of atmospheric particles.

Bibliography

[1] Q. Zhang, J. L. Jimenez, M. R. Canagaratna, J. D. Allan, H. Coe, I. Ulbrich, M. R. Alfarra, A. Takami, A. M. Middlebrook, Y. L. Sun, K. Dzepina, E. Dunlea, K. Docherty, P. F. DeCarlo, D. Salcedo, T. Onasch, J. T. Jayne, T. Miyoshi, A. Shimono, S. Hatakeyama, N. Takegawa, Y. Kondo, J. Schneider, F. Drewnick, S. Borrmann, S. Weimer, K. Demerjian, P. Williams, K. Bower, R. Bahreini, L. Cottrell, R. J. Griffin, J. Rautiainen, J. Y. Sun, Y. M. Zhang, and D. R. Worsnop. Ubiquity and dominance of oxygenated species in organic aerosols in anthropogenically-influenced Northern Hemisphere midlatitudes. *Geophys. Res. Lett.*, 34:L13801, 2007.

[2] D. M. Murphy, D. S. Thomson, and T. M. J. Mahoney. In situ measurements of organics, meteoritic material, mercury, and other elements in aerosols at 5 to 19 kilometers. *Science*, 282:1664–1669, November 1998.

[3] M. Dymarska, B. J. Murray, L. M. Sun, M. L. Eastwood, D. A. Knopf, and A. K. Bertram. Deposition ice nucleation on soot at temperatures relevant for the lower troposphere. *J. Geophys. Res.-Atmos.*, 111: D04204, 2006.

[4] J. E. Shilling, T. J. Fortin, and M. A. Tolbert. Depositional ice nucleation on crystalline organic and inorganic solids. *J. Geophys. Res.-Atmos.*, 111 (D12):D12204, 2006.

[5] K. J. Baustian, M. E. Wise, and M. A. Tolbert. Depositional ice nucleation on solid ammonium sulfate and glutaric acid particles. *Atmos. Chem. and Phys.*, 10(5):2307–2317, 2010.

[6] B. Zobrist, C. Marcolli, T. Koop, B. P. Luo, D. M. Murphy, U. Lohmann, A. A. Zardini, U. K. Krieger, T. Corti, D. J. Cziczo, S. Fueglistaler, P. K. Hudson, D. S. Thomson, and T. Peter. Oxalic acid as a heterogeneous ice nucleus in the upper troposphere and its indirect aerosol effect. *Atmos. Chem. Phys.*, 6:3115–3129, 2006.

[7] A. J. Prenni, P. J. DeMott, S. M. Kreidenweis, D. E. Sherman, L. M. Russell, and Y. Ming. The effects of low molecular weight dicarboxylic acids on cloud formation. *J. Phys. Chem. A*, 105(50):11240–11248, 2001.

[8] Z. A. Kanji, O. Florea, and J. P. D. Abbatt. Ice formation via deposition nucleation on mineral dust and organics: dependence of onset relative humidity on total particulate surface area. *Environ. Res. Lett.*, 3(2): 025004, 2008.

[9] O. Möhler, S. Buttner, C. Linke, M. Schnaiter, H. Saathoff, O. Stetzer, R. Wagner, M. Kramer, A. Mangold, V. Ebert, and U. Schurath. Effect of sulfuric acid coating on heterogeneous ice nucleation by soot aerosol particles. *J. Geophys. Res.-Atmos.*, 110(D11), JUN 14 2005.

[10] O. Möhler, C. Linke, H. Saathoff, M. Schnaiter, R. Wagner, A. Mangold, M. Krämer, and U. Schurath. Ice nucleation on flame soot aerosol of different organic carbon content. *Meteorol. Z.*, 14(4):477–484, 2005.

[11] O. Möhler, S Benz, H. Saathoff, M. Schnaiter, R. Wagner, J. Schneider, S. Walter, V. Ebert, and S. Wagner. The effect of organic coating on the heterogeneous ice nucleation efficiency of mineral dust aerosols. *Environ. Res. Lett.*, 3(2):1425–1435, 2008.

[12] P. J. DeMott, Y. Chen, S. M. Kreidenweis, D. C. Rogers, and D. E. Sherman. Ice formation by black carbon particles. *Geophys. Res. Lett.*, 28(16):2429–2432, August 1999.

[13] K. A. Koehler, P. J. DeMott, S. M. Kreidenweis, O. B. Popovicheva, M. D. Petters, C. M. Carrico, E. D. Kireeva, T. D. Khokhlovac, and N. K. Shonijac. Cloud condensation nuclei and ice nucleation activity of hydrophobic and hydrophilic soot particles. *Phys. Chem Chem. Phys.*, 11:7906–7920, 2009.

[14] P. J. DeMott, M. D. Petters, A. J. Prenni, C. M. Carrico, S. M. Kreidenweis, J. L. Collett, and H. Moosmuller. Ice nucleation behavior of biomass combustion particles at cirrus temperatures. *J. Geophys. Res.-Atmos.*, 114, 2009.

[15] M. D. Petters, M. T. Parsons, A. J. Prenni, P. J. DeMott, S. M. Kreidenweis, C. M. Carrico, A. P. Sullivan, G. R. McMeeking, E. Levin, C. E. Wold, J. L. Collett, and H. Moosmuller. Ice nuclei emissions from biomass burning. *J. Geophys. Res.-Atmos.*, 114(6):401–404, 2009.

[16] J. Heymsfield, A. and M. Miloshevich, L. Relative humidity and temperature influences on cirrus formation and evolution: Observations from wave clouds and FIRE II. *J. Atmos. Sci.*, 52(23):4302–4326, December 1995.

[17] J. Ström, M. Seifert, B. Kärcher, J. Ovarlez, A. Minikin, J. F. Gayet, R. Krejci, A. Petzold, F. Auriol, W. Haag, R. Busen, U. Schumann, and H. C. Hansson. Cirrus cloud occurrence as function of ambient relative humidity: a comparison of observations obtained during the INCA experiment. *Atmos. Chem. Phys.*, 3(5):1807–1816, 2003.

[18] W. Haag, B Kärcher, J. Ström, A. Minikin, U. Lohmann, J. Ovarlez, and A. Stohl. Freezing thresholds and cirrus cloud formation mechanisms inferred from in situ measurements of relative humidity. *Atmos. Chem. Phys.*, 3(5):1791–1806, 2003.

[19] T. Koop, J. Bookhold, M. Shiraiwa, and U. Poschl. Glass transition and phase state of organic compounds: dependency on molecular properties and implications for secondary organic aerosols in the atmosphere. *Phys. Chem. Chem. Phys.*, 13:19238–19255, 2011.

[20] R. Pruppacher, H. and J. D. Klett. *Microphysics of Clouds and Precipitation.* Kluwer Academic Publishers, Netherlands, 1997.

[21] A. T. Lambe, T. B. Onasch, P. Massoli, D. R. Croasdale, J. P. Wright, A. T. Ahern, L. R. Williams, D. R. Worsnop, W. H. Brune, and P. Davidovits. Laboratory studies of the chemical composition and cloud condensation nuclei (ccn) activity of secondary organic aerosol (soa) and oxidized primary organic aerosol (opoa). *Atmos. Chem. and Phys.*, 11 (17):8913–8928, 2011.

[22] J. C. Doran, J. C. Barnard, W. P. Arnott, R. Cary, R. Coulter, J. D. Fast, E. I. Kassianov, L. Kleinman, N. S. Laulainen, T. Martin, G. Paredes-Miranda, M. S. Pekour, W. J. Shaw, D. F. Smith, S. R. Springston, and X.-Y. Yu. The t1-t2 study: evolution of aerosol properties downwind of mexico city. *Atmos. Chem. and Phys.*, 7(6):1585–1598, 2007.

[23] R. C. Moffet, T. R. Henn, A. V. Tivanski, R. J. Hopkins, Y. Desyaterik, A. L. D. Kilcoyne, T. Tyliszczak, J. Fast, J. Barnard, V. Shutthanandan, S. S. Cliff, K. D. Perry, A. Laskin, and M. K. Gilles. Microscopic characterization of carbonaceous aerosol particle aging in the outflow from mexico city. *Atmos. Chem. and Phys.*, 10(3):961–976, 2010.

[24] R. C. Moffet, T. Henn, A. Laskin, and M. K. Gilles. Automated chemical analysis of internally mixed aerosol particles using x-ray spectromicroscopy at the carbon k-edge. *Anal. Chem.*, 82(19):7906–7914, 2010.

[25] D. M. Murphy and T. Koop. Review of the vapour pressures of ice and supercooled water for atmospheric applications. *Q. J. R. Meteorol. Soc.*, 131(608):1539–1565, 2005.

[26] M. L. Eastwood, S. Cremel, C. Gehrke, E. Girard, and A. K. Bertram. Ice nucleation on mineral dust particles: Onset conditions, nucleation rates and contact angles. *J. Geophys. Res.-Atmos.*, 113:D22203, 2008.

[27] M. Bailey and J. Hallett. Nucleation Effects on the Habit of Vapour Grown Ice Crystals from -18°C to -42°C. *Quart. J. R. Met. Soc.*, 128: 1461–1483, 2002.

[28] R. C. Schaller and N. Fukuta. Ice nucleation by aerosol particles: Experimental studies using a Wedge-Shaped ice thermal diffusion chamber. *J. Atmos. Sci.*, 36:1788–1802, 1979.

[29] P. Roberts and J. Hallett. A laboratory study of the ice nucleating properties of some mineral particulates. *Quart. J. R. Met. Soc.*, 94: 25–34, 1968.

[30] A. Welti, F. Lüönd, and U. Lohmann. Influence of particle size on the ice nucleating ability of mineral dusts. *Atmos. Chem. Phys.*, 9(18):6705–6715, 2009.

[31] F. Zimmermann, M. Ebert, A. Worringen, L. Schutz, and S. Weinbruch. Environmental scanning electron microscopy (ESEM) as a new technique to determine the ice nucleation capability of individual atmospheric aerosol particles. *Atmos. Environ.*, 41(37):8219–8227, 2007.

[32] A. Salam, U. Lohmann, B. Crenna, G. Lesins, P. Klages, D. Rogers, R. Irani, A. MacGillivray, and M. Coffin. Ice nucleation studies of mineral dust particles with a new continuous flow diffusion chamber. *Aerosol Sci. Technol.*, 40(2):134–143, 2006.

[33] T. Koop, B. P. Luo, A. Tsias, and T. Peter. Water activity as the determinant for homogeneous ice nucleation in aqueous solutions. *Nature*, 406:611–614, August 2000.

[34] G. Kulkarni and S. Dobbie. Ice nucleation properties of mineral dust particles: determination of onset RH$_i$, in active fraction, nucleation time-lag, and the effect of active sites on contact angles. *Atmos. Chem. and Phys.*, 10(1):95–105, 2010.

[35] Z. A. Kanji and J. P. D. Abbatt. Ice nucleation onto Arizona Test Dust at cirrus temperatures: Effenct of temperature and aerosol size on onset relative humidity. *J. Phys. Chem. A*, 114(2):935–941, 2010.

[36] R. W. Saunders, O. Möhler, M. Schnaiter, S. Benz, R. Wagner, H. Saathoff, P. J. Connolly, R. Burgess, B. J. Murray, M. Gallagher, R. Wills, and J. M. C. Plane. An aerosol chamber investigation of the heterogeneous ice nucleating potential of refractory nanoparticles. *Atmos. Chem. and Phys.*, 10(3):1227–1247, 2010.

[37] A. G. Detwiler and V. Bernard. Humidity required for ice nucleation from the vapor onto silver iodide and lead iodide aerosols over the temperature range -6 to -67 °C. *J. Appl. Meteor.*, 20:1006–1012, 1981.

[38] D. J. Cziczo, O. Stetzer, A Worringen, S. Ebert, M.and Weinbruch, M. Kamphus, S.J. Gallavardin, J. Curtius, K. D. Borrmann, S.and Froyd, S. Mertes, O. Möhler, and U. Lohmann. Inadvertent climate modification due to anthropogenic lead. *Nature Geosci*, 2(5):333–336, 2009.

[39] D. A. Knopf, B. Wang, A. Laskin, R. C. Moffet, and M. K. Gilles. Heterogeneous nucleation of ice on anthropogenic organic particles collected in mexico city. *Geophys. Res. Lett.*, 37:L11803, 2010.

[40] T. B. Onasch, R. L. Siefert, S. D. Brooks, A. J. Prenni, B. Murray, M. A. Wilson, and M. A. Tolbert. Infrared spectroscopic study of the deliquescence and efflorescence of ammonium sulfate aerosol as a function of temperature. *J. Geophys. Res.-Atmos.*, 104(D17):21317–21326, 1999.

[41] C. F. Braban, J. P. D. Abbatt, and D. J. Cziczo. Deliquescence of Ammonium Sulfate Particles at Sub-Eutectic Temperatures. *Geophys. Res. Lett.*, 28(20):3879–3882, October 2001.

[42] M. T. Parsons, D. A. Knopf, and A. K. Bertram. Deliquescence and crystallization of ammonium sulfate particles internally mixed with water-soluble organic compounds. *J. Phys. Chem. A*, 108(52):11600–11608, 2004.

[43] D. J. Cziczo and J. P. D. Abbatt. Infrared observations of the response of NaCl, $MgCl_2$, NH_4HSO_4, and NH_4NO_3 aerosols to changes in relative humidity from 298 to 238 K. *J. Phys. Chem. A*, 104:2038–2047, 2000.

[44] T. Koop, A. Kapilashrami, L. T. Molina, and M. J. Molina. Phase transitions of sea-salt/water mixtures at low temperatures: Implications for ozone chemistry in the polar marine boundary layer. *J. Geophys. Res.-Atmos.*, 105(D21):26393–26402, November 2000.

[45] Z. A. Kanji, P. J. DeMott, O. Möhler, and J. P. D. Abbatt. Results from the university of toronto continuous flow diffusion chamber at icis 2007: instrument intercomparison and ice onsets for different aerosol types. *Atmos. Chem. and Phys.*, 11(1):31–41, 2011.

[46] B. J. Murray, T. W. Wilson, S. Dobbie, Z. Q. Cui, Smrk Al-Jumur, O. Möhler, M. Schnaiter, R. Wagner, S. Benz, M. Niemand, H. Saathoff, V. Ebert, S. Wagner, and B. Kärcher. Heterogeneous nucleation of ice particles on glassy aerosols under cirrus conditions. *Nature Geosci.*, 3: 233–237, 2010.

[47] M. E. Wise, K. J. Baustian, T. Koop, M. A. Freedman, E. J. Jensen, and M. A. Tolbert. Depositional ice nucleation onto hydrated nacl particles: a new mechanism for ice formation in the troposphere. *Atmos. Chem. and Phys. Discuss.*, 11(8):23139–23167, 2011.

[48] R. Wagner, O. Möhler, H. Saathoff, M. Schnaiter, and T. Leisner. New cloud chamber experiments on the heterogeneous ice nucleation ability of oxalic acid in the immersion mode. *Atmos. Chem. and Phys.*, 11(5): 2083–2110, 2011.

[49] M. E. Wise, K. J. Baustian, and M. A. Tolbert. Internally mixed sulfate and organic particles as potential ice nuclei in the tropical tropopause region. *Proc. Natl. Acad. Sci.*, 107(15):6693–6698, 2010.

[50] J. P. D. Abbatt, S. Benz, D. J. Cziczo, Z. Kanji, U. Lohmann, and O. Möhler. Solid Ammonium Sulfate Aerosols as Ice Nuclei: A Pathway for Cirrus Cloud Formation. *Science*, 313:1770–1773, September 2006.

[51] Daniel A. Knopf. *personal communication*, 2011.

[52] T. Koop and B. Zobrist. Parameterizations for ice nucleation in biological and atmospheric systems. *Phys. Chem. Chem. Phys.*, 11(46):10839–10850, 2009.

[53] D. K. Lynch, K. Sassen, D. O. Starr, and G. Stephens. *Cirrus*, pages 3–101. Oxford University Press, New York, 2002.

[54] M.D. Shupe, S.Y. Matrosov, and T. Uttal. Arctic mixed-phase cloud properties derived from surface-based sensors at SHEBA. *J. Atmos. Sci.*, 63(2):697–711, FEB 2006.

[55] T. Corti and T. Peter. A simple model for cloud radiative forcing. *Atm. Chem. Phys.*, 9(15):5751–5758, 2009.

[56] B. J. Finlayson-Pitts and J. N. Pitts. *Chemistry of the Upper and Lower Atmosphere*. Academic Press, San Diego, California, 2000.

[57] H. Seinfeld, John and N. Pandis, Spyros. *Atmospheric Chemistry and Physics*. John Wiley & Sons, New York, 1998.

[58] M. Quante. The role of clouds in the climate system. *J. PHYS. IV*, 121: 61–86, DEC 2004.

[59] X.J. Wang and J.R. Key. Arctic surface, cloud, and radiation properties based on the AVHRR Polar Pathfinder dataset. Part I: Spatial and temporal characteristics. *J. Clim.*, 18(14):2558–2574, JUL 15 2005.

[60] X.J. Wang and J.R. Key. Arctic surface, cloud, and radiation properties based on the AVHRR Polar Pathfinder dataset. Part II: Recent trends. *J. Clim.*, 18(14):2575–2593, JUL 15 2005.

[61] M.D. Shupe, T. Uttal, and S.Y. Matrosov. Arctic cloud microphysics retrievals from surface-based remote sensors at SHEBA. *J. Appl. Meteorol.*, 44(10):1544–1562, OCT 2005.

[62] D. P. Wylie, W. P. Jackson, W. P. Menzel, and J. J. Bates. Trends in global cloud cover in two decades of HIRS observations. *J. Clim.*, 18: 3021–3031, August 2005.

[63] T. Chen, W. B. Rossow, and Y. Zhang. Radiative effects of cloud-type variations. *J. Clim.*, 13(1):264–286, 2000.

[64] G. M. McFarquhar, G. Zhang, M. R. Poellot, G. L. Kok, R. McCoy, T. Tooman, A. Fridlind, and A. J. Heymsfield. Ice properties of single-layer stratocumulus during the Mixed-Phase Arctic Cloud Experiment: 1. Observations. *J. Geophys. Res.-Atmos.*, 112:D24201, 2007.

[65] D. R. Dowling and L. F. Radke. A summary of the physical properties of cirrus clouds. *J. Appl. Meteorol.*, 29:970–978, 1990.

[66] M. B. Baker. Cloud Microphysics and Climate. *Science*, 276:1072–1078, June 1997.

[67] J. A. Curry, J. L. Schramm, W. B. Rossow, and D. Randall. Overview of arctic cloud and radiation characteristics. *J. Clim.*, 9(8):1731–1764, 1996.

[68] S. Vavrus. The impact of cloud feedbacks on arctic climate under greenhouse forcing. *J. Clim.*, 17(3):603–615, 2004.

[69] A.J. Prenni, P. J. DeMott, S. M. Kreidenweis, J. Y. Harrington, A. Avramov, J. Verlinde, M. Tjernström, C. N. Long, and P. Q. Olsson. Can ice-nucleating aerosols affect arctic seasonal climate? *Bull. Am. Meteorol. Soc.*, 88(4):541–550, 2007.

[70] J. Verlinde, J. Y. Harrington, V. T. Yannuzzi, A. Avramov, S. Greenberg, S. J. Richardson, C. P. Bahrmann, G. M. McFarquhar, G. Zhang, N. Johnson, M. R. Poellot, J. H. Mather, D. D. Turner, E. W. Eloranta, D. C. Tobin, R. Holz, B. D. Zak, M. D. Ivey, A. J. Prenni, P. J. DeMott, J. S. Daniel, G. L. Kok, K. Sassen, D. Spangenberg, P. Minnis, T. P. Tooman, M. Shupe, A. J. Heymsfield, and R. Schofield. The mixed-phase arctic cloud experiment. *Bull. Am. Meteorol. Soc.*, 88(2):205–221, 2007.

[71] D. L. Hartmann, M. E. O. Bell, and M. L. Michelsen. The effect of cloud type on earth's energy balance: Global analysis. *J. Clim.*, 5(11): 1281–1304, 1992.

[72] D. K. Lynch, K. Sassen, D. O. Starr, and G. Stephens. *Cirrus*, pages 41–77. Oxford University Press, New York, 2002.

[73] Matthew Bailey and John Hallett. Growth rates and habits of ice crystals between -20°C and -70°C. *J. Atmos. Sci.*, 61(5):514–544, 2004.

[74] M. Wendisch, P. Yang, and P. Pilewskie. Effects of ice crystal habit on thermal infrared radiative properties and forcing of cirrus. *J. Geophys. Res.*, 112:D08201, 2007.

[75] D. A. Hegg and M. B. Baker. Nucleation in the atmosphere. *Rep. Prog. Phys.*, 72(5):056801, 2009.

[76] A. Avramov and J. Y. Harrington. Influence of parameterized ice habit on simulated mixed phase Arctic clouds. *J. Geophys. Res.-Atmos.*, 115: D03205, 2010.

[77] A. Wegener. *Thermodynamik der Atmosphäre*. Johann Ambrosius Barth, Leipzig, 1911.

[78] T. Bergeron. On the physics of clouds and precipitation. *Proc. 5th Assembly UGGI, Lisbon*, 2:156, 1935.

[79] W. Findeisen. Die kolloidmeteorologischen vorgänge bei der niederschlagsbildung (colloidal meteorological processes in the formation of precipitation). *Meteor. Z.*, 55:121–133, 1938.

[80] R. R. Rogers and M. K. Yau. International Series in Natural Philosophy, Woburn, Massuchusetts, USA, 1989.

[81] U. Lohmann and K. Diehl. Sensitivity studies of the importance of dust ice nuclei for the indirect aerosol effect on stratiform mixed-phase clouds. *J. Atmos. Sci.*, 63:968–982, 2006.

[82] T. Storelvmo, C. Hoose, and P. Eriksson. Global modeling of mixed-phase clouds: The albedo and lifetime effects of aerosols. *J. Geophys. Res.*, 116:D05207, 2011.

[83] A. P. Khain. Notes on state-of-the-art investigations of aerosol effects on precipitation: a critical review. *Environ. Res. Lett.*, 4(1):015004, 2009.

[84] J. R. Holton, P. H. Haynes, M. E. Mcintyre, A. R. Douglass, R. B. Rood, and L. Pfister. Stratosphere-troposphere exchange. *Rev. Geophys.*, 33 (4):403–439, 1995.

[85] I. M. Held and B. J. Soden. Water vapor feedback and global warming. *Annu. Rev. Energ. Environ.*, 25:441–475, 2000.

[86] J. Lelieveld, C. Brühl, P. Jockel, B. Steil, P. J. Crutzen, H. Fischer, M. A. Giorgetta, P. Hoor, M. G. Lawrence, R. Sausen, and H. Tost. Stratospheric dryness: model simulations and satellite observations. *Atmos. Chem. Phys.*, 7:1313–1332, 2007.

[87] E. Jensen and L. Pfister. Transport and freeze-drying in the tropical tropopause layer. *J. Geophys. Res.-Atmos.*, 109(D2):1425–1434, 2004.

[88] T. Peter, B. P. Luo, M. Wirth, C. Kiemle, H. Flentje, V. A. Yushkov, V. Khattatov, V. Rudakov, A. Thomas, S. Borrmann, G. Toci, P. Mazzinghi, J. Beuermann, C. Schiller, F. Cairo, G. Di Donfrancesco, A. Adriani, C. M. Volk, J. Strom, K. Noone, V. Mitev, R. A. MacKenzie, K. S. Carslaw, T. Trautmann, V. Santacesaria, and L. Stefanutti. Ultrathin

Tropical Tropopause Clouds (UTTCs): I. Cloud morphology and occurrence. *Atmos. Chem. Phys.*, 3(D15):1083–1091, 2003.

[89] P. Forster, V. Ramaswamy, P. Artaxo, T. Berntsen, R. Betts, D. W. Fahey, J. Haywood, J. Lean, D. C. Lowe, G. Myhre, J. Nganga, R. Prinn, G. Raga, M. Schulz, and R. Van Dorland. *Climate Change 2007: The Physical Science Basis. Contribution of Working Group I to the Fourth Assessment Report of the Intergovernmental Panel on Climate Change*, chapter Changes in Atmospheric Constituents and in Radiative Forcing, pages 131–234. Cambridge University Press, 2007.

[90] M. B. Baker and T. Peter. Small-scale cloud processes and climate. *Nature*, 451:299–300, 2008.

[91] W. Cantrell and A. Heymsfield. Production of ice in tropospheric clouds. *Bull. Amer. Meteor. Soc.*, 86(6):795–807, June 2005.

[92] M. Kanakidou, J. H. Seinfeld, S. N. Pandis, I. Barnes, F. J. Dentener, M. C. Facchini, R. Van Dingenen, B. Ervens, A. Nenes, C. J. Nielsen, E. Swietlicki, J. P. Putaud, Y. Balkanski, S. Fuzzi, J. Horth, G. K. Moortgat, R. Winterhalter, C. E. L. Myhre, K. Tsigaridis, E. Vignati, E. G. Stephanou, and J. Wilson. Organic aerosol and global climate modelling: a review. *Atmos. Chem. Phys.*, 5(4):1053–1123, 2005.

[93] D. Rosenfeld, U. Lohmann, G. B. Raga, C. D. O′Dowd, M. Kulmala, S. Fuzzi, A. Reissell, and M.O. Andreae. Flood or drought: How do aerosols affect precipitation? *Science*, 321(5894):1309–1313, 2008.

[94] G. McFiggans, P. Artaxo, U. Baltensperger, H. Coe, M. C. Facchini, G. Feingold, S. Fuzzi, M. Gysel, A. Laaksonen, U. Lohmann, T. F. Mentel, D. M. Murphy, C. D. O'Dowd, J. R. Snider, and E. Weingartner. The effect of physical and chemical aerosol properties on warm cloud droplet activation. *Atmos. Chem. and Phys.*, 6(9):2593–2649, 2006.

[95] Y. J. Kaufman and I. Koren. Smoke and pollution aerosol effect on cloud cover. *Science*, 313(5787):655–658, 2006.

[96] M. O. Andreae and D. Rosenfeld. Aerosol-cloud-precipitation interactions. Part 1. The nature and sources of cloud-active aerosols. *Earth Science Reviews*, 89(1-2):13–41, 2008.

[97] B. Albrecht. Aerosols, cloud microphysics and fractional cloudiness. *Science*, 245:1227–1230, 1989.

[98] S. Twomey. Pollution and planetary albedo. *Atmos. Environ.*, 8(12): 1251–1256, 1974.

[99] V. Ramanathan, P. J. Crutzen, J. T. Kiehl, and D. Rosenfeld. Aerosols, climate, and the hydrological cycle. *Science*, 294(5549):2119–2124, 2001.

[100] D. Rosenfeld. Suppression of rain and snow by urban and industrial air pollution. *Science*, 287(5459):1793–1796, March 2000.

[101] G. Vali. Nucleation Terminology. *J. Aerosol Sci.*, 16(6):575–576, 1985.

[102] T. Koop. Homogeneous ice nucleation in water and aqueous solutions. *Z. Phys. Chemie-Int. J.*, 218(11):1231–1258, 2004.

[103] E. K. Bigg. The formation of atmospheric ice crystals by the freezing of droplets. *Q. J. R. Meteorol. Soc.*, 79(342):510–519, 1953.

[104] E. K. Bigg. The supercooling of water. *Proc. Phys. Soc. B*, 66(404): 688–694, 1953.

[105] N.H. Fletcher. Size effect in heterogeneous nucleation. *J. Chem. Phys.*, 29:572–576, 1958.

[106] J.P. Chen, A. Hazra, and Z. Levin. Parameterizing ice nucleation rates using contact angle and activation energy derived from laboratory data. *Atmos. Chem. Phys.*, 8(24):7431–7449, 2008.

[107] G. Vali. Quantitative evaluation of experimental results on heterogeneous freezing nucleation of supercooled liquids. *J. Atmos. Sci.*, 28: 402–409, 1971.

[108] D. Niedermeier, S. Hartmann, R. A. Shaw, D. Covert, T. F. Mentel, J. Schneider, L. Poulain, P. Reitz, C. Spindler, T. Clauss, A. Kiselev, E. Hallbauer, H. Wex, K. Mildenberger, and F. Stratmann. Heterogeneous freezing of droplets with immersed mineral dust particles measurements and parameterization. *Atmos. Chem. Phys.*, 10(8):3601–3614, 2010.

[109] B. J. Murray, S. L. Broadley, T. W. Wilson, J. D. Atkinson, and R. H. Wills. Heterogeneous freezing of water droplets containing kaolinite particles. *Atmos. Chem. Phys.*, 11:4191?4207, 2011.

[110] P. A. Alpert, J. Y. Aller, and D. A. Knopf. Ice nucleation from aqueous nacl droplets with and without marine diatoms. *Atmos. Chem. Phys.*, 11(12):5539–5555, 2011.

[111] D. C. Rogers, P. J. DeMott, S. M. Kreidenweis, and Y. L. Chen. Measurements of ice nucleating aerosols during success. *Geophys. Res. Lett.*, 25(9):1383–1386, 1998.

[112] P. J. DeMott, D. J. Cziczo, A. J. Prenni, D. M. Murphy, S. M. Kreidenweis, D. S. Thomson, R. Borys, and D. C. Rogers. Measurements of the concentration and composition of nuclei for cirrus formation. *Proc. Natl. Acad. Sci.*, 100(25):14655–14660, December 2003.

[113] O. Stetzer, B. Baschek, F. Lüönd, and U. Lohmann. The zurich ice nucleation chamber (zinc) - a new instrument to investigate atmospheric ice formation. *Aerosol. Sci. Technol.*, 42(1):64–74, 2008.

[114] B. Zobrist, C. Marcolli, T. Peter, and T. Koop. Heterogeneous ice nucleation in aqueous solutions: the role of water activity. *J. Phys. Chem. A*, 112(17):3965–3975, 2008.

[115] D. A. Knopf and M. D. Lopez. Homogeneous ice freezing temperatures and ice nucleation rates of aqueous ammonium sulfate and aqueous levoglucosan particles for relevant atmospheric conditions. *Phys. Chem Chem. Phys.*, 11:8056–8068, 2009.

[116] D. A. Knopf and Y. J. Rigg. Homogeneous ice nucleation from aqueous inorganic/organic particles representative of biomass burning: Water activity, freezing temperatures, nucleation rates. *J. Phys. Chem. A*, 115: 762–773, 2010.

[117] D. A. Knopf, P. A. Alpert, Bingbing Wang, and J. Y. Aller. Stimulation of ice nucleation by marine diatoms. *Nature Geosci.*, 4:88–90, 2011.

[118] D. A. Knopf and S. Forrester. Heterogeneous ice nucleation from water and aqueous NaCl droplets coated by 1-nonadecanol and 1-nonadecanoic acid monolayers. *J. Phys. Chem. A*, 115:5579–5591, 2011.

[119] P. A. Alpert, J. Y. Aller, and D. A. Knopf. Initiation of the ice phase by marine biogenic surfaces in supersaturated gas and supercooled aqueous phases. *Phys. Chem. Chem. Phys.*, page In press, 2011.

[120] C. Marcolli, S. Gedamke, T. Peter, and B. Zobrist. Efficiency of immersion mode ice nucleation on surrogates of mineral dust. *Atmos. Chem. Phys.*, 7(19):5081–5091, 2007.

[121] F. Lüönd, O. Stetzer, A. Welti, and U. Lohmann. Experimental study on the ice nucleation ability of size–selected kaolinite particles in the immersion mode. *J. Geophys. Res.-Atmos.*, 115:D14201, 2010.

[122] D. Niedermeier, R. A. Shaw, S. Hartmann, H. Wex, T. Clauss, J. Voigtländer, and F. Stratmann. Heterogeneous ice nucleation: exploring the transition from stochastic to singular freezing behavior. *Atmos. Chem. and Phys.*, 11(16):8767–8775, 2011.

[123] S. Fuzzi, M. O. Andreae, B. J. Huebert, M. Kulmala, T. C. Bond, M. Boy, S. J. Doherty, A. Guenther, M. Kanakidou, K. Kawamura, V.-M. Kerminen, U. Lohmann, L. M. Russell, and U. Pöschl. Critical assessment of the current state of scientific knowledge, terminology, and research needs concerning the role of organic aerosols in the atmosphere, climate, and global change. *Atmos. Chem. and Phys.*, 6(7):2017–2038, 2006.

[124] Y. Iinuma, E. Brüggemann, T. Gnauk, K. Müller, M. O. Andreae, G. Helas, R. Parmar, and H. Herrmann. Source characterization of biomass burning particles: The combustion of selected European conifers, African hardwood, savanna grass, and German and Indonesian peat. *J. Geophys. Res.*, 112:D08209, 2007.

[125] P. M. Fine, G. R. Cass, and B. R. T. Simoneit. Chemical characterization of fine particle emissions from fireplace combustion of woods grown in the northeastern united states. *Environ. Sci. Technol.*, 35(13):2665–2675, 2001.

[126] S. Gao, D. A. Hegg, P. V. Hobbs, T. W. Kirchstetter, B. I. Magi, and M. Sadilek. Water-soluble organic components in aerosols associated with savanna fires in southern Africa: Identification, evolution, and distribution. *J. Geophys. Res.*, 108(D13):S524–S537, 2003.

[127] M. Posfai, A. Gelencser, R. Simonics, K. Arato, J. Li, P. V. Hobbs, and P. R. Buseck. Atmospheric tar balls: Particles from biomass and biofuel burning. *J. Geophys. Res.*, 109(D6):S524–S537, 2004.

[128] J. J. Schauer, M. J. Kleeman, G. R. Cass, and B. R. T. Simoneit. Measurement of emissions from air pollution sources. 3. C1–C29 organic compounds from fireplace combustion of wood. *Environ. Sci. Technol.*, 35 (9):1716–1728, 2001.

[129] J. J. Schauer, M. J. Kleeman, G. R. Cass, and B. R. T. Simoneit. Measurement of emissions from air pollution sources. 3. C1–C29 organic compounds from fireplace combustion of wood. *Environ. Sci. Technol.*, 35 (9):1716–1728, 2001.

[130] M. Hallquist, J. C. Wenger, U. Baltensperger, Y. Rudich, D. Simpson, M. Claeys, J. Dommen, N. M. Donahue, C. George, A. H. Goldstein, J. F. Hamilton, H. Herrmann, T. Hoffmann, Y. Iinuma, M. Jang, M. E. Jenkin, J. L. Jimenez, A. Kiendler-Scharr, W. Maenhaut, G. McFiggans, Th. F. Mentel, A. Monod, A. S. H. Prévôt, J. H. Seinfeld, J. D. Surratt, R. Szmigielski, and J. Wildt. The formation, properties and impact of secondary organic aerosol: current and emerging issues. *Atmos. Chem. and Phys.*, 9(14):5155–5236, 2009.

[131] B. R. T. Simoneit, W. F. Rogge, M. A. Mazurek, L. J. Standley, L. M. Hildemann, and G. R. Cass. Lignin pyrolysis products, lignans, and resin acids as specific tracers of plant classes in emissions from biomass combustion. *Environ. Sci. Technol.*, 27(12):2533–2541, 1993.

[132] W. F. Rogge, L. M. Hildemann, M. A. Mazurek, G. R. Cass, and B. R. T. Simoneit. Sources of fine organic aerosol. 3. Road dust, tire debris, and organometallic brake lining dust - roads as sources and sinks. *Environ. Sci. Technol.*, 27(9):1892–1904, 1993.

[133] B. R. T. Simoneit. A review of biomarker compounds as source indicators and tracers for air pollution. *Environ. Sci. Pollut. Res.*, 6(3):159–169, 1999.

[134] S. Decesari, M. C. Facchini, S. Fuzzi, and E. Tagliavini. Characterization of water-soluble organic compounds in atmospheric aerosol: A new approach. *J. Geophys. Res.*, 105(D1):1481–1489, 2000.

[135] E. R. Graber and Y. Rudich. Atmospheric HULIS: How humic-like are they? A comprehensive and critical review. *Atmos. Chem. Phys.*, 6(3): 729–753, 2006.

[136] D. M. Murphy, D. J. Cziczo, K. D. Froyd, P. K. Hudson, B. M. Matthew, A. M. Middlebrook, R. E. Peltier, A. Sullivan, D. S. Thomson, and R. J. Weber. Single-particle mass spectrometry of tropospheric aerosol particles. *J. Geophys. Res.-Atmos.*, 111(D23), SEP 30 2006.

[137] S. Decesari, M. C. Facchini, E. Matta, M. Mircea, S. Fuzzi, A. R. Chughtai, and D. M. Smith. Water soluble organic compounds formed by oxidation of soot. *Atmos. Environ.*, 36(11):1827–1832, 2002.

[138] M. C. Facchini, M. Mircea, S. Fuzzi, and R. J. Charlson. Cloud albedo enhancement by surface-active organic solutes in growing droplets. *Nature*, 401(6750):257–259, 1999.

[139] F. Cavalli, M. C. Facchini, S. Decesari, M. Mircea, L. Emblico, S. Fuzzi, D. Ceburnis, Y. J. Yoon, C. D. O'Dowd, J. P. Putaud, and A. Dell'Acqua. Advances in characterization of size-resolved organic matter in marine aerosol over the North Atlantic. *J. Geophys. Res.*, 109: D24215, 2004.

[140] M. S. Jang, N. M. Czoschke, S. Lee, and R. M. Kamens. Heterogeneous atmospheric aerosol production by acid-catalyzed particle-phase reactions. *Science*, 298(5594):814–817, 2002.

[141] H. M. Hung, Y. Katrib, and S. T. Martin. Products and mechanisms of the reaction of oleic acid with ozone and nitrate radical. *J. Phys. Chem. A*, 109(20):4517–4530, 2005.

[142] G. Kiss, E. Tombacz, and H. C. Hansson. Surface tension effects of humic-like substances in the aqueous extract of tropospheric fine aerosol. *J. Atmos. Chem.*, 50(3):279–294, 2005.

[143] O. L. Mayol-Bracero, P. Guyon, B. Graham, G. Roberts, M. O. Andreae, S. Decesari, M. C. Facchini, S. Fuzzi, and P. Artaxo. Water-soluble organic compounds in biomass burning aerosols over Amazonia - 2. Apportionment of the chemical composition and importance of the polyacidic fraction. *J. Geophys. Res.-Atmos.*, 107(D20):189–195, 2002.

[144] H. Lukács, A. Gelencsér, S. Hammer, H. Puxbaum, C. Pio, M. Legrand, A. Kasper-Giebl, M. Handler, A. Limbeck, D. Simpson, and S. Preunkert. Seasonal trends and possible sources of brown carbon based on 2-year aerosol measurements at six sites in Europe. *J. Geophys. Res.*, 112:D23S18, 2007.

[145] T. Feczko, H. Puxbaum, A. Kasper-Giebl, M. Handler, A. Limbeck, A. Gelencsér, C. Pio, S. Preunkert, and M. Legrand. Determination of water and alkanline extratable atmospheric humic-like substances with the TU Vienna HULIS analyzer in samples from six background sites in Europe. *J. Geophys. Res.*, 112:D23S10, 2007.

[146] P. Lin, X. Huang, L. He, and J. Z. Yu. Abundance and size distribution of HULIS in ambient aerosols at a rural site in South China. *J. Aerosol. Sci.*, 41:74–87, 2010.

[147] M. O. Andreae and P. J. Crutzen. Atmospheric aerosols: Biogeochemical sources and role in atmospheric chemistry. *Science*, 276(5315):1052–1058, 1997.

[148] J. L. Jimenez, M. R. Canagaratna, N. M. Donahue, A. S. H. Prevot, Q. Zhang, J. H. Kroll, P. F. DeCarlo, J. D. Allan, H. Coe, N. L. Ng, A. C. Aiken, K. S. Docherty, I. M. Ulbrich, A. P. Grieshop, A. L. Robinson, J. Duplissy, J. D. Smith, K. R. Wilson, V. A. Lanz, C. Hueglin, Y. L. Sun, J. Tian, A. Laaksonen, T. Raatikainen, J. Rautiainen, P. Vaattovaara, M. Ehn, M. Kulmala, J. M. Tomlinson, D. R. Collins, M. J. Cubison, E., J. Dunlea, J. A. Huffman, T. B. Onasch, M. R. Alfarra, P. I. Williams, K. Bower, Y. Kondo, J. Schneider, F. Drewnick, S. Borrmann, S. Weimer, K. Demerjian, D. Salcedo, L. Cottrell, R. Griffin, A. Takami, T. Miyoshi, S. Hatakeyama, A. Shimono, J. Y Sun, Y. M. Zhang, K. Dzepina, J. R. Kimmel, D. Sueper, J. T. Jayne, S. C. Herndon, A. M. Trimborn, L. R. Williams, E. C. Wood, A. M. Middlebrook, C. E. Kolb, U. Baltensperger, and D. R. Worsnop. Evolution of Organic Aerosols in the Atmosphere. *Science*, 326(5959):1525–1529, 2009.

[149] P. J. Crutzen and M. O. Andreae. Biomass burning in the tropics - impact on atmospheric chemistry and biogeochemical cycles. *Science*, 250(4988):1669–1678, 1990.

[150] J. Fishman, K. Fakhruzzaman, B. Cros, and D. Nganga. Identification of widespread pollution in the southern-hemisphere deduced from satellite analyses. *Science*, 252(5013):1693–1696, 1991.

[151] M. Fromm, J. Alfred, K. Hoppel, J. Hornstein, R. Bevilacqua, E. Shettle, R. Servranckx, Z. Q. Li, and B. Stocks. Observations of boreal forest fire smoke in the stratosphere by POAM III, SAGE II, and lidar in 1998. *Geophys. Res. Lett.*, 27(9):1407–1410, 2000.

[152] M. Fromm, R. Bevilacqua, R. Servranckx, J. Rosen, J. P. Thayer, J. Herman, and D. Larko. Pyro-cumulonimbus injection of smoke to the stratosphere: Observations and impact of a super blowup in northwestern Canada on 3-4 August 1998. *J. Geophys. Res.*, 110(D8), 2005.

[153] G. Wotawa and M. Trainer. The influence of Canadian forest fires on pollutant concentrations in the United States. *Science*, 288(5464):324–328, 2000.

[154] S. Fuzzi, S. Decesari, M. C. Facchini, E. Matta, M. Mircea, and E. Tagliavini. A simplified model of the water soluble organic component of atmospheric aerosols. *Geophys. Res. Lett.*, 28(21):4079–4082, 2001.

[155] D. M. Murphy, P. K. Hudson, D. J. Cziczo, S. Gallavardin, K. D. Froyd, M. V. Johnston, A. M. Middlebrook, M. S. Reinard, D. S. Thomson,

T. Thornberry, and A. S. Wexler. Distribution of lead in single atmospheric particles. *Atmos. Chem. and Phys.*, 7(12):3195–3210, 2007.

[156] K. D. Froyd, D. M. Murphy, P. Lawson, D. Baumgardner, and R. L. Herman. Aerosols that form subvisible cirrus at the tropical tropopause. *Atmos. Chem. Phys.*, 10(1):209–218, 2010.

[157] D. J. Cziczo, D. M. Murphy, P. K. Hudson, and D. S. Thomson. Single particle measurements of the chemical composition of cirrus ice residue during CRYSTAL-FACE. *J. Geophys. Res.*, 109:D04201, 2004.

[158] A. J. Prenni, M. D. Petters, S. M. Kreidenweis, C. L. Heald, S. T. Martin, P. Artaxo, R. M. Garland, A. G. Wollny, and U. Pöschl. Relative roles of biogenic emissions and Saharan dust as ice nuclei in the Amazon basin. *Nat. Geosci.*, 2(6):402–405, 2009.

[159] Y. Rudich. Laboratory perspectives on the chemical transformations of organic matter in atmospheric particles. *Chem. Rev.*, 103(12):5097–5124, 2003.

[160] D. A. Knopf, L. M. Anthony, and A. K. Bertram. Reactive uptake of O_3 by multicomponent and multiphase mixtures containing oleic acid. *J. Phys. Chem. A*, 109(25):5579–5589, 2005.

[161] D. A. Knopf, J. Mak, S. Gross, and A. K. Bertram. Does atmospheric processing of saturated hydrocarbon surfaces by NO_3 lead to volatilization? *Geophys. Res. Lett.*, 33:L17816, 2006.

[162] Y. Rudich, N. M. Donahue, and T. F. Mentel. Aging of organic aerosol: Bridging the gap between laboratory and field studies. *Annu. Rev. Phys. Chem.*, 58:321–352, 2007.

[163] N. Riemer, H. Vogel, and B. Vogel. Soot aging time scales in polluted regions during day and night. *Atmos. Chem. Phys.*, 4:1885–1893, 2004.

[164] I. J. George and J. P. D. Abbatt. Heterogeneous oxidation of atmospheric aerosol particles by gas-phase radicals. *Nature Chem.*, 2(9):713–722, SEP 2010.

[165] B. Zuberi, K. S. Johnson, G. K. Aleks, L. T. Molina, and A. Laskin. Hydrophilic properties of aged soot. *Geophys. Res. Lett.*, 32(1):3033–3043, 2005.

[166] M. Springmann, D. A. Knopf, and N. Riemer. Detailed heterogeneous chemistry in an urban plume box model: reversible co-adsorption of O_3, NO_2, and H_2O on soot coated with benzo[a]pyrene. *Atmos. Chem. and Phys.*, 9(19):7461–7479, 2009.

[167] Daniel A. Knopf, Seanna M. Forrester, and Jonathan H. Slade. Heterogeneous oxidation kinetics of organic biomass burning aerosol surrogates by O_3, NO_2, N_2O_5, and NO_3. *Phys. Chem. Chem. Phys.*, 13, 21050-21062, 2011 .

[168] J. C. Kaiser, N. Riemer, and D. A. Knopf. Detailed heterogeneous oxidation of soot surfaces in a particle-resolved aerosol model. *Atmos. Chem. and Phys.*, 11(9):4505–4520, 2011.

[169] V. A. Garten and R. B. Head. Carbon particles and ice nucleation. *Nature*, 201:1091–1092, 1964.

[170] M. L. Eastwood, S. Cremel, M. Wheeler, B. J. Murray, E. Girard, and A. K. Bertram. Effects of sulfuric acid and ammonium sulfate coatings on the ice nucleation properties of kaolinite particles. *Geophys. Res. Lett.*, 36:L02811, 2009.

[171] A. J. Prenni, M. D. Petters, A. Faulhaber, C. M. Carrico, P. J. Ziemann, S. M. Kreidenweis, and P. J. DeMott. Heterogeneous ice nucleation measurements of secondary organic aerosol generated from ozonolysis of alkenes. *Geophys. Res. Lett.*, 36(6):401–404, 2009.

[172] R. C. Sullivan, L. Minambres, P. J. DeMott, A. J. Prenni, C. M. Carrico, E. J. T. Levin, and S. M. Kreidenweis. Chemical processing does not always impair heterogeneous ice nucleation of mineral dust particles. *Geophys. Res. Lett.*, 37, DEC 21 2010.

[173] R. C. Sullivan, M. D. Petters, P. J. DeMott, S. M. Kreidenweis, H. Wex, D. Niedermeier, S. Hartmann, T. Clauss, F. Stratmann, P. Reitz, J. Schneider, and B. Sierau. Irreversible loss of ice nucleation active sites in mineral dust particles caused by sulphuric acid condensation. *Atmos. Chem. and Phys.*, 10(23):11471–11487, 2010.

[174] B. Friedman, G. Kulkarni, J. B. Welti, A. Zelenyuk, J. A. Thornton, and D. J. Cziczo. Ice nucleation and droplet formation by bare and coated soot particles. *J. Geophys. Res.-Atmos.*, page in press, 2011.

[175] S. T. Martin. Phase Transitions of Aqueous Atmospheric Particles. *Chemical Reviews*, 100:3403–3453, 2000.

[176] E. Mikhailov, S. Vlasenko, S. T. Martin, T. Koop, and U. Pöschl. Amorphous and crystalline aerosol particles interacting with water vapor: conceptual framework and experimental evidence for restructuring, phase transitions and kinetic limitations. *Atmos. Chem. and Phys.*, 9(24): 9491–9522, 2009.

[177] P.G. Debenedetti and F.H. Stillinger. Supercooled liquids and the glass transition. *Nature*, 410(6825):259–267, MAR 8 2001.

[178] C. Marcolli, B. P. Luo, and T. Peter. Mixing of the organic aerosol fractions: Liquids as the thermodynamically stable phases. *J. Phys. Chem. A*, 108(12):2216–2224, 2004.

[179] B. J. Murray. Inhibition of ice crystallisation in highly viscous aqueous organic acid droplets. *Atmos. Chem. and Phys.*, 8(17):5423–5433, 2008.

[180] B. Zobrist, C. Marcolli, D. A. Pedernera, and T. Koop. Do atmospheric aerosols form glasses? *Atmos. Chem. Phys.*, 8(17):5221–5244, 2008.

[181] P. J. DeMott, K. Sassen, M. R: Poellot, D. Baumgardner, D. C. Rogers, S. D. Brooks, A. J. Prenni, and S. M. Kreidenweis. African dust aerosols as atmospheric ice nuclei. *Geophys. Res. Lett.*, 30(14):1–1–1–4, 2003.

[182] Y. Chen, S. M. Kreidenweis, L. M. McInnes, D. C. Rogers, and P. J. DeMott. Single particle analyses of ice nucleating aerosols in the upper troposphere and lower stratosphere. *Geophys. Res. Lett.*, 25(9):1391–1394, 1998.

[183] D. J Cziczo, K. D Froyd, S. J Gallavardin, O. Möhler, S. Benz, H. Saathoff, and D. M Murphy. Deactivation of ice nuclei due to atmospherically relevant surface coatings. *Environ. Res. Lett.*, 4(4):044013, 2009.

[184] K. D. Froyd, D. M. Murphy, T. J. Sanford, D. S. Thomson, J. C. Wilson, L. Pfister, and L. Lait. Aerosol composition of the tropical upper troposphere. *Atmos. Chem. and Phys.*, 9(13):4363–4385, 2009.

[185] D. J. Cziczo, P. J. DeMott, S. D. Brooks, A. J. Prenni, D. S. Thomson, D. Baumgardner, J. C. Wilson, S. M. Kreidenweis, and D. M. Murphy. Observations of organic species and atmospheric ice formation. *Geophys. Res. Lett.*, 31(12):L12116, 2004.

[186] R. B. Head. Steroids as ice nucleators. *Nature*, 191(479):1058–1059, 1961.

[187] R. B. Head. Ice nucleation by alpha-phenazine. *Nature*, 196(4856):736–738, 1962.

[188] R. B. Head. Ice nucleation by some cyclic compounds. *J. Phys. Chem. Solids*, 23(OCT):1371, 1962.

[189] H. W. Georgii. Investigation on the Deactivation of Inorganic and Organic Freezing-Nulcei. *Z. Angew. Math. Phys.*, 14(5):503–510, 1963.

[190] V. A. Garten and R. B. Head. Hydrogen-bonding patterns and ice nucleation, 1964.

[191] N. Fukuta. A study of the mechanism of contact ice nucleation. *J. Atmos. Sci.*, 32:1597–1603, 1966.

[192] M. Gavish, R. Popovitzbiro, M. Lahav, and L. Leiserowitz. Ice nucleation by alcohols arranged in monolayers at the surface of water drops. *Science*, 250(4983):973–975, 1990.

[193] L. H. Seeley and G. T. Seidler. Two-dimensional nucleation of ice from supercooled water. *Phys. Rev. Lett.*, 8705(5), 2001.

[194] L. H. Seeley and G. T. Seidler. Preactivation in the nucleation of ice by langmuir films of aliphatic alcohols. *J. Chem. Phys.*, 114(23):10464–10470, 2001.

[195] M. T. Parsons, J. Mak, S. R. Lipetz, and A. K. Bertram. Deliquescence of malonic, succinic, glutaric, and adipic acid particles. *J. Geophys. Res.*, 109:D06212, 2004.

[196] Z. A. Kanji and J. P. D. Abbatt. Laboratory studies of ice formation via deposition mode nucleation onto mineral dust and n-hexane soot samples. *J. Geophys. Res.-Atmos.*, 111:D16204, 2006.

[197] B. Zobrist, T. Koop, B. P. Luo, C. Marcolli, and T. Peter. Heterogeneous ice nucleation rate coefficient of water droplets coated by a nonadecanol monolayer. *J. Phys. Chem. A*, 111:2149–2155, 2007.

[198] O. Möhler, D. G. Georgakopoulos, C. E. Morris, S. Benz, V. Ebert, S. Hunsmann, H. Saathoff, M. Schnaiter, and R. Wagner. Heterogeneous ice nucleation activity of bacteria: new laboratory experiments at simulated cloud conditions. *Biogeosciences*, 5(5):1425–1435, 2008.

[199] A. P. Fornea, S. D. Brooks, J. B. Dooley, and A. Saha. Heterogeneous freezing of ice on atmospheric aerosols containing ash, soot, and soil. *J. Geophys. Res.-Atmos.*, 114:D13201, 2009.

[200] E. D. Kireeva, O. B. Popovicheva, N. M. Persiantseva, T. D. Khokhlova, and N. K. Shonija. Effect of black carbon particles on the efficiency of water droplet freezing. *Colloid J.*, 71(3):353–359, 2009.

[201] K. A. Pratt, A. J. Heymsfield, C. H. Twohy, S. M. Murphy, P. J. DeMott, J. G. Hudson, R. Subramanian, Z. Wang, J. H. Seinfeld, and K. A. Prather. In Situ Chemical Characterization of Aged Biomass-Burning Aerosols Impacting Cold Wave Clouds. *J. Atmos. Sci.*, 67(8):2451–2468, AUG 2010.

[202] G. Vali. Repeatability and randomness in heterogeneous freezing nucleation. *Atmos. Chem. Phys.*, 8(16):5017–5031, 2008.

[203] P. J. DeMott. An exploratory study of ice nucleation by soot aerosols. *J. Appl. Meteor.*, 29:1072–1079, 1990.

[204] B. Gorbunov, A. Baklanov, N. Kakutkina, H. L. Windsor, and R. Toumi. Ice nucleation on soot particles. *J. Aerosol. Sci.*, 32(2):199–215, 2001.

[205] A. Virtanen, J. Joutsensaari, T. Koop, J. Kannosto, P. Yli-Pirilä, J. Leskinen, J. M. Mäkelä, J. K. Holopainen, U. Pöeschl, M. Kulmala, D. R. Worsnop, and A. sLaaksonen. An amorphous solid state of biogenic secondary organic aerosol particles. *Nature*, 467(7317):824–827, OCT 14 2010.

[206] A. Virtanen, J. Kannosto, H. Kuuluvainen, A. Arffman, J. Joutsensaari, E. Saukko, L. Hao, P. Yli-Pirilä, P. Tiitta, J. K. Holopainen, J. Keskinen, D. R. Worsnop, J. N. Smith, and A. Laaksonen. Bounce behavior of freshly nucleated biogenic secondary organic aerosol particles. *Atmos. Chem. and Phys.*, 11(16):8759–8766, 2011.

[207] M. Shiraiwa, M. Ammann, T. Koop, and U. Poschl. Gas uptake and chemical aging of semisolid organic aerosol particles. *Proc. Natl. Acad. Sci.*, 108(27):11003–11008, 2011.

[208] K. D. Young and E. J. Leboeuf. Glass transition behavior in a peat humic acid and an aquatic fulvic acid. *Environ. Sci. Technol.*, 34(21): 4549–4553, NOV 1 2000.

[209] B. Zobrist, V. Soonsin, B. P. Luo, U. K. Krieger, C. Marcolli, T. Peter, and T. Koop. Ultra-slow water diffusion in aqueous sucrose glasses. *Phys. Chem. Chem. Phys.*, 13:3514–3526, 2011.

[210] H. J. Tong, J. P. Reid, D. L. Bones, B. P. Luo, and U. K. Krieger. Measurements of the timescales for the mass transfer of water in glassy aerosol at low relative humidity and ambient temperature. *Atmos. Chem. and Phys.*, 11(10):4739–4754, 2011.

[211] T. Peter, C. Marcolli, P. Spichtinger, T. Corti, M. B. Baker, and T. Koop. When dry air is too humid. *Science*, 314(5804):1399–1402, 2006.

[212] M. Gordon and J. S. Taylor. Ideal copolymers and the second-order transitions of synthetic rubbers. i. non-crystalline copolymers. *J. of Appl. Chem.*, 2(9):493–500, 1952.

[213] T. Koop, B. P. Luo, U. M. Biermann, P. J. Crutzen, and T. Peter. Freezing of $HNO_3/H_2SO_4/H_2O$ Solutions at Stratospheric Temperatures: Nucleation Statistics and Experiments. *J. Phys. Chem. A*, 101:1117–1133, 1997.

[214] B. Wang and D. A. Knopf. Heterogeneous ice nucleation on particles composed of humic–like substances impacted by O_3. *J. Geophys. Res.-Atmos.*, 116:D03205, 2011.

[215] G. Vali. Freezing rate due to heterogeneous nucleation. *J. Atmos. Sci.*, 51(13):1843–1856, 1994.

[216] P. J. Connolly, O. Möhler, P. R. Field, H. Saathoff, R. Burgess, T. Choularton, and M. Gallagher. Studies of heterogeneous freezing by three different desert dust samples. *Atmos. Chem. Phys.*, 9(8):2805–2824, 2009.

[217] P. J. DeMott, A. J. Prenni, X. Liu, S. M. Kreidenweis, M. D. Petters, C. H. Twohy, M. S. Richardson, T. Eidhammer, and D. C. Rogers. Predicting global atmospheric ice nuclei distributions and their impacts on climate. *Proc. Natl. Acad. Sci.*, 107(25):11217–11222, 2010.

[218] CalNex. page http://esrl.noaa.gov/csd/calnex/, 2010.

[219] L. T. Molina, S. Madronich, J. S. Gaffney, H. B. Singh, and U. Puschl. Acp special issue: Milagro/intex-b 2006. *Atmos. Chem. and Phys.*, 2007.

[220] A. Laskin, J. P. Cowin, and M. J. Iedema. Analysis of individual environmental particles using modern methods of electron microscopy and x-ray microanalysis. *J. Electron Spectr. Rel. Phenom.*, 150(2-3):260–274, 2006.

[221] R. C. Moffet, Y. Desyaterik, R. J. Hopkins, A. V. Tivanski, M. K. Gilles, Y. Wang, V. Shutthanandan, L. T. Molina, R. G. Abraham, K. S. Johnson, V. Mugica, M. J. Molina, A. Laskin, K. A. Prather. Characterization of aerosols containing zn, pb, and cl from an industrial region of mexico city. *Environ. Sci. Technol.*, 42(19):7091–7097, 2008.

[222] A. Laskin and J. P. Cowin. Automated single-particle sem/edx analysis of submicrometer particles down to 0.1 m. *Anal. Chem.*, 73(5):1023–1029, 2001.

[223] A. Laskin, M. J. Iedema, and J. P. Cowin. Time-resolved aerosol collector for CCSEM/EDX single-particle analysis. *Aerosol Sci. Technol.*, 37(3): 246–260, MAR 2003.

[224] R. C. Moffet, A. V. Tivanski, and M. K. Gilles. *Scanning Transmission X-ray Microscopy: Applications in Atmospheric Aerosol Research.* CRC Press Taylor and Francis Group, Boca Raton, 2010. ISBN 978-1-4200-8561-7.

[225] A. L. D. Kilcoyne, T. Tyliszczak, W. F. Steele, S. Fakra, P. Hitchcock, K. Franck, E. Anderson, B. Harteneck, E. G. Rightor, G. E. Mitchell, A. P. Hitchcock, L. Yang, T. Warwick, and H. Ade. Interferometer-controlled scanning transmission X-ray microscopes at the Advanced Light Source. *J. Synchrotron Rad.*, 10(2):125–136, Mar 2003.

[226] S. Ghorai and A. V. Tivanski. Hygroscopic behavior of individual submicrometer particles studied by x-ray spectromicroscopy. *Anal. Chem.*, 82(22):9289–9298, 2010.

[227] S. Ghorai, A. Laskin, and A. V. Tivanski. Spectroscopic evidence of keto–enol tautomerism in deliquesced malonic acid particles. *J. Phys. Chem. A*, 115(17):4373–4380, 2011.

[228] U. Lohmann and J Feichter. Global indirect aerosol effects: a review. *Atmos. Chem. Phys.*, 5(3):715–737, 2005.

[229] Y. S. Choi and C. H. Ho. Radiative effect of cirrus with different optical properties over the tropics in MODIS and CERES observations. *Geophys. Res. Lett.*, 33:L21811, 2006.

[230] J. Lee, P. Yang, A. E. Dessler, B. Gao, and S. Platnick. Distribution and radiative forcing of tropical thin cirrus clouds. *J. Atmos. Sci.*, 66 (12):3721–3731, 2009.

[231] H. J. Jost, K. Drdla, A. Stohl, L. Pfister, M. Loewenstein, J. P. Lopez, P. K. Hudson, D. M. Murphy, D. J. Cziczo, M. Fromm, T. P. Bui, J. Dean-Day, C. Gerbig, M. J. Mahoney, E. C. Richard, N. Spichtinger, J. V. Pittman, E. M. Weinstock, J. C. Wilson, and I. Xueref. In-situ observations of mid-latitude forest fire plumes deep in the stratosphere. *Geophys. Res. Lett.*, 31:L11101, 2004.

[232] D. M. Murphy, D. J. Cziczo, P. K. Hudson, and D. S. Thomson. Carbonaceous material in aerosol particles in the lower stratosphere and tropopause region. *J. Geophys. Res.*, 112:D04203, 2007.

[233] A. J. Prenni, P. J. Demott, D. C. Rogers, S. M. Kreidenweis, G. M. McFarquhar, G. Zhang, and M. R. Poellot. Ice nuclei characteristics from M-PACE and their relation to ice formation in clouds. *Tellus B*, 61(2):436–448, 2009.

[234] S. M. Li, J. Tang, H. S. Xue, and D. Toom-Sauntry. Size distribution and estimated optical properties of carbonate, water soluble organic carbon, and sulfate in aerosols at a remote high altitude site in western china. *Geophys. Res. Lett.*, 27:1107–1110, 2000.

[235] Z. Krivacsy, A. Hoffer, Z. Sarvari, D. Temesi, U. Baltensperger, S. Nyeki, E. Weingartner, S. Kleefeld, and S. G. Jennings. Role of organic and black carbon in the chemical composition of atmospheric aerosol at european background sites. *Atmos. Environ.*, 35:6231–6244, 2001.

[236] F. Yu. Formation of large NAT particles and denitrification in polar stratosphere: possible role of cosmic rays and effect of solar activity. *Atmos. Chem. Phys.*, 4(50):2273–2283, 2004.

[237] I. Salma, R. Ocskay, and G. G. Láng. Properties of atmospheric humic-like substances – water system. *Atmos. Chem. Phys.*, 8(8):2243–2254, 2008.

[238] C. Baduel, D. Voisin, and J. L. Jaffrezo. Comparison of analytical methods for humic like substances (hulis) measurements in atmospheric particles. *Atmos. Chem. Phys.*, 9(16):5949–5962, 2009.

[239] P. Lin, G. Engling, and J. Z. Yu. Humic-like substances in fresh emissions of rice straw burning and in ambient aerosols in the pearl river delta region, china. *Atmos. Chem. Phys.*, 10(14):6487–6500, 2010.

[240] M. N. Chan and C. K. Chan. Hygroscopic properties of two model humic-like substances and their mixtures with inorganics of atmospheric importance. *Environ. Sci. Technol.*, 37(22):5109–5115, 2003.

[241] S. D. Brooks, P. J. DeMott, and S. M. Kreidenweis. Water uptake by particles containing humic materials and mixtures of humic materials with ammonium sulfate. *Atmos. Environ.*, 38(13):1859–1868, 2004.

[242] M. Gysel, E. Weingartner, S. Nyeki, D. Paulsen, U. Baltensperger, I. Galambos, and G. Kiss. Hygroscopic properties of water-soluble matter and humic-like organics in atmospheric fine aerosol. *Atmos. Chem. Phys.*, 4(13):35–50, 2004.

[243] B. Svenningsson, J. Rissler, E. Swietlicki, M. Mircea, M. Bilde, M. C. Facchini, S. Decesari, S. Fuzzi, J. Zhou, J. Monster, and T. Rosenorn. Hygroscopic growth and critical supersaturations for mixed aerosol particles of inorganic and organic compounds of atmospheric relevance. *Atmos. Chem. Phys.*, 6(9):1937–1952, 2006.

[244] E. Dinar, I. Taraniuk, E. R. Graber, S. Katsman, T. Moise, T. Anttila, T. F. Mentel, and Y. Rudich. Cloud condensation nuclei properties of model and atmospheric HULIS. *Atmos. Chem. Phys.*, 6(9):2465–2482, 2006.

[245] T. Koop, H. P. Ng, L. T. Molina, and M. J. Molina. A new optical technique to study aerosol phase transitions: The nucleation of ice from H_2SO_4 aerosols. *J. Phys. Chem. A*, 102(45):8924–8931, 1998.

[246] D. A. Knopf and T. Koop. Heterogeneous nucleation of ice on surrogates of mineral dust. *J. Geophys. Res.*, 111:D12201, 2006.

[247] D. A. Knopf, T. Koop, B. P. Luo, U. G. Weers, and T. Peter. Homogeneous nucleation of NAD and NAT in liquid stratospheric aerosols: insufficient to explain denitrification. *Atmos. Chem. Phys.*, 2(3):207–214, 2002.

[248] B. Kärcher and J. Ström. The roles of dynamical variability and aerosols in cirrus cloud formation. *Atmos. Chem. and Phys.*, 3(3):823–838, 2003.

[249] J. Zahardis and G. A. Petrucci. The oleic acid-ozone heterogeneous reaction system: products, kinetics, secondary chemistry, and atmospheric implications of a model system: a review. *Atmos. Chem. Phys.*, 7:1237–1274, 2007.

[250] T. Ye, D. Wynn, R. Dudek, and E. Borguet. Photoreactivity of alkylsiloxane self-assembled monolayers on silicon oxide surfaces. *Langmuir*, 17:4497–4500, 2001.

[251] E. R. Thomas, G. J. Frost, and Y. Rudich. Reactive uptake of ozone by proxies for organic aerosols: Surface-bound and gas-phase products. *J. Geophys. Res.*, 106(D3):3045–3056, 2001.

[252] T. L. Eliason, S. Aloisio, D. J. Donaldson, D. J. Cziczo, and V. Vaida. Processing of unsaturated organic acid films and aerosols by ozone. *Atmos. Environ.*, 37(16):2207–2219, 2003.

[253] M. J. Molina, A. V. Ivanov, S. Trakhtenberg, and L. T. Molina. Atmospheric evolution of organic aerosol. *Geophys. Res. Lett.*, 31(22):L22104, 2004.

[254] B. D'Anna, J. Adla, G. Christian, S. Konrad, F. Simon, A. Markus, and W Armin. Light-induced ozone depletion by humic acid films and submicron aerosol particles. *J. Geophys. Res.*, 114:D12301, 2009.

[255] B. Kärcher. Physicochemistry of aircraft-generated liquid aerosols, soot, and ice particles 1. Model description. *J. Geophys. Res.*, 103(D14): 17111–17128, 1998.

[256] H. Morrison, J.A. Curry, and V. I. Khvorostyanov. A new double-moment microphysics parameterization for application in cloud and climate models. Part I: Description. *J. Atmos. Sci.*, 62:1665–1677, 2005.

[257] E. Dinar, T. F. Mentel, and Y. Rudich. The density of humic acids and humic like substances (HULIS) from fresh and aged wood burning and pollution aerosol particles. *Atmos. Chem. and Phys.*, 6(12):5213–5224, 2006.

[258] P. K. Hudson, D. M. Murphy, D. J. Cziczo, D. S. Thomson, J. A. de Gouw, C. Warneke, J. Holloway, J. R. Jost, and G. Hubler. Biomass-burning particle measurements: Characteristic composition and chemical processing. *J. Geophys. Res.*, 109:D23S27, 2004.

[259] W. Szyrmer and I. Zawadzki. Biogenic and anthropogenic sources of ice-forming nuclei: A review. *Bull. Am. Meteorol. Soc.*, 78(2):209–228, 1997.

[260] B. Gorbunov and A. Safatov. In-situ measurements of the ice-forming activity of metal-oxide aerosols with controlled amounts of surface-active groups. *J. Aerosol. Sci.*, 25(4):673–682, 1994.

[261] M. S. Akhter, A. R. Chughtai, and D. M. Smith. The Structure of hexane soot I: spectroscopic studies. *Appl. Spectrosc.*, 39(1):143–153, 1985.

[262] D.M. Smith, W.F. Welch, J.A. Jassim, A.R. Chughtai, and D.H. Stedman. Soot-ozone reaction kinetics: spectroscopic and gravimetric studies. *Appl. Spectrosc.*, 42(8):1473–1482, NOV-DEC 1988.

[263] A. R. Chughtai, J. A. Jassim, J. H. Peterson, D. H. Stedman, and D. M. Smith. Spectroscopic and solubility characteristics of oxidized soots. *Aerosol Sci. Technol.*, 15(2):112–126, 1991.

[264] H. M. Daly and A. B. Horn. Heterogeneous chemistry of toluene, kerosene and diesel soots. *Phys. Chem. Chem. Phys.*, 11:1069–1076, 2009.

[265] K. Adachi, E. J. Freney, and P. R. Buseck. Shapes of internally mixed hygroscopic aerosol particles after deliquescence, and their effect on light scattering. *Geophys. Res. Lett.*, 38:L13804, 2011.

[266] J. Cozic, S. Mertes, B. Verheggen, D. J. Cziczo, S. J. Gallavardin, U. S. Walter, Baltensperger, and E. Weingartner. Black carbon enrichment in atmospheric ice particle residuals observed in lower tropospheric mixed phase clouds. *J. Geophys. Res.-Atmos.*, 113:D15209, 2008.

[267] O. Möhler, C. Linke, H. Saathoff, M. Schnaiter, R. Wagner, U. Schurath, A. Mangold, and M. Krämer. Ice nucleation on flame soot aerosol of different organic carbon content. *Meteorolog. Z.*, 14, 2005.

[268] K. Diehl and S. K. Mitra. A laboratory study of the effects of a kerosene–burner exhaust on ice nucleation and the evaporation rate of ice crystals. *Atmos. Environ.*, 32:3145–3151, 1998.

[269] O. Popovicheva, E. Kireeva, N. Persiantseva, T. Khokhlova, N. Shonija, V. Tishkova, and B. Demirdjian. Effect of soot on immersion freezing of water and possible atmospheric implications. *Atmos. Res.*, 90(2-4):326 – 337, 2008.

[270] B. Zobrist, C. Marcolli, T. Peter, and T. Koop. Heterogeneous ice nucleation in aqueous solutions: the role of water activity. *J. Phys. Chem. A*, 112(17):3965–3975, 2008.

[271] J. Mao, X. Ren, W. H. Brune, J. R. Olson, J. H. Crawford, A. Fried, L. G. Huey, R. C. Cohen, B. Heikes, H. B. Singh, D. R. Blake, G. W. Sachse, G. S. Diskin, S. R. Hall, and R. E. Shetter. Airborne measurement of oh reactivity during intex-b. *Atmos. Chem. and Phys.*, 9(1):163–173, 2009.

[272] F. Drewnick, S. S. Hings, P. DeCarlo, J. T. Jayne, M. Gonin, K. Fuhrer, S. Weimer, J. L. Jimenez, K. L. Demerjian, S. Borrmann, and D. R. Worsnop. A new time-of-flight aerosol mass spectrometer (TOF-AMS) - Instrument description and first field deployment. *Aerosol Sci. Technol.*, 39(7):637–658, JUL 2005.

[273] A. C. Aiken, P. F. Decarlo, J. H. Kroll, D. R. Worsnop, J. Alex Huffman, K. S. Docherty, I. M. Ulbrich, C. Mohr, J. R. Kimmel, D. Sueper, Y. Sun, Q. Zhang, A. Trimborn, M. Northway, P. J. Ziemann, M. R. Canagaratna, T. B. Onasch, M. R. Alfarra, A. S. H. Prevot, J. Dommen, J. Duplissy, A. Metzger, U. Baltensperger, and J. L. Jimenez. O/C and OM/OC ratios of primary, secondary, and ambient organic aerosols with high-resolution time-of-flight aerosol mass spectrometry. *Environ. Sci. Technol.*, 42(12):4478–4485, JUN 15 2008.

[274] S. W. Stein, B. J.'Turpin, X.'P. Cai, C. P. F. Huang, and P. H. Mcmurry. Measurements of relative humidity-dependent bounce and density for atmospheric particles using the DMA-Impator technique. *Atmos. Environ.*, 28(10):1739–1746, JUN 1994.

[275] B. Dahneke. The capture of aerosol particles by surfaces. *J. Colloid Interface Sci.*, 37(2):342–353, 1971.

[276] I. Kohl, L. Bachmann, A. Hallbrucker, E. Mayer, and T. Loerting. Liquid-like relaxation in hyperquenched water at leq140 K. *Phys. Chem. Chem. Phys.*, 7:3210–3220, 2005.